Formation of supermassive black holes in the high-redshift universe

宇宙初期の超巨大ブラックホール形成

稲吉恒平

Kohei Inayoshi

Department of Physics, Kyoto University, Kyoto 606-8502, Japan

January 5, 2011

Abstract

In the Universe, there is an enormous number of structures and objects such as galaxies, stars, and planets. Remarkable progresses of observations grow our understanding about their origins and formation processes. Among them, recent observations of high-redshift quasars reveal that supermassive black holes (SMBHs) with mass of $\gtrsim 10^9\ M_\odot$ have already formed as early as the beginning of the universe. As the formation processes of such BHs, the gas accretion and mergers of the remnant BHs formed by the collapse of first generation stars ($\sim 100\ M_\odot$) have been considered. However, various radiative feedbacks prevent the efficient BH growth and thus the required time to form SMBHs becomes longer than the age of the high-redshift universe.

As a solution of this problem, formation of supermassive stars (SMSs; $M_* \gtrsim 10^5\ M_\odot$) and their subsequent collapse directly to the BHs in the first galaxies has been considered. Seed BHs formed by the direct collapse are expected to sufficiently shorten the formation time even with the radiative feedbacks. Formation of SMSs in first galaxies irradiated with strong far ultraviolet (FUV) radiation has often been studied. In such cases, the primordial gas clouds are supposed to collapse monolithically and form stars without strong fragmentation since H_2 molecules, which are the main coolants of primordial gas and promote gas fragmentation, are photo-dissociated.

In this thesis, we discuss the unified scenario of the seed BH formation through the direct collapse of SMSs. We have investigated the formation of SMSs in the following three parts; (i) formation of supermassive clouds in the first galaxies, (ii) collapse phase of the supermassive cloud, and (iii) evolution of the protostar up to a SMS.

We first reconsider conditions of the SMS formation requiring the H_2 photodissociation by the strong FUV radiations. Candidates of FUV sources, including star-forming galaxies, are probably sources of strong CRs and X-rays too. We find that external ionization promotes H_2 production and elevates the threshold FUV intensity needed for SMS formation as $J_{\rm crit} \propto U_{\rm CR}^{1/2}$ ($\propto J_X^{1/2}$) in the high CR (respectively X-ray) limit. Therefore, the SMS formation under the strong FUV radiations is strongly suppressed by the ionizations due to the external high-energy radiations (CRs and X-rays).

Following the result, we propose the new pathway to form SMSs without assuming the strong FUV radiations. The assembly of a typical first galaxy proceeds via cold and dense flows penetrating deep to the center, where the supersonic streams collide each other to develop a hot and dense shocked gas. In such dense shocked layer, H_2 molecules are collisionally dissociated and thus supermassive clouds are formed. Thereafter, the supermassive cloud collapses isothermally by the atomic cooling (Lyα and various continuum emissions). The range of post-shock conditions for SMS formation can be expressed as $T \gtrsim 6000$ K $(n_{\rm H}/10^4\ {\rm cm}^{-3})^{-1}$ for $n_{\rm H} \lesssim 10^4\ {\rm cm}^{-3}$ and $T \gtrsim 5000 - 6000$

K for $n_{\rm H} \gtrsim 10^4$ cm^{-3}. Moreover, metal enrichment does not affect the above condition for metallicity below $\sim 10^{-3}\ Z_\odot$ if metals are in the gas phase.

Next, we investigate the fate of a supermassive cloud using the three-dimensional hydrodynamical simulations. We find the cloud can collapse runaway and without efficient fragmentation even if the cloud has turbulent motions. Though the $\rm H_2$ fractions are rapidly enhanced by the three-body reaction ($\rm 3H \rightarrow H_2 + H$), the $\rm H_2$ cooling (both of line and continuum emission) never play a significant role for the thermal evolution at the central region. When the central region becomes optically thick, single hydrostatic core (i.e., protostar) is formed. The formed protostar grows via rapid accretion fed the dense filamentary flows. The accretion rate is so high ($\dot{M}_{\rm acc} \sim 3\ M_\odot$ yr^{-1}) that the protostar is expected to evolve up to a supermassive star ($\gtrsim 10^5\ M_\odot$) within its lifetime

Finally, we solved the stellar structure growing at the rate of $\gtrsim 0.01\ M_\odot$ yr^{-1}. Under rapid accretion, the stellar radius continues to increases monolithically with the stellar mass following $R_* \propto M_*^{1/2}$. The stellar interior inhomogeneously contracts by losing the thermal energy. The maximum of the stellar radius is $R_* \simeq 4 \times 10^4\ R_\odot \sim 10^2$ AU for $M_* \sim 10^4\ M_\odot$. With this very large radius, the stellar effective temperature is less than 10^4 K even after the protostar becomes supermassive. Strong UV feedback, which could limit the mass accretion onto the star, is thus unlikely to operate in this case. Moreover, we investigate the stability of the accreting protostar against the stelar pulsations. As a result, accreting SMSs become pulsation unstable due to the κ-mechanism, but the resulting mass-loss rates are still much lower than the accretion rates. We conclude that the protostar rapidly grows to a SMS ($\gtrsim 10^5\ M_\odot$) without the strong mass-loss due to the negative feedbacks.

Contents

Chapter 1

Introduction

1.1 Observations of SMBHs in the early universe

The origin and formation process of supermassive black holes (SMBHs), which ubiquitously exist at the center of present-day galaxies, still remain a mystery. Among them, observations by Soltan Digital Sky Survey (SDSS) have revealed the existence of SMBHs with mass of $\gtrsim 10^9\ M_\odot$ in the high-redshift universe at $z > 6$ (e.g., Fan 2006; Willott et al. 2010). More deep observations (e.g., Jiang et al. 2009; Willott et al. 2010; Lawrence et al. 2007) have found a lot of additional high-z quasars (QSOs) and some 50 QSOs have been discovered at $z > 5.7$ in the past decade. The most distant QSO exists in the early universe at $z = 7.085$, which corresponds to the age of the Universe ~ 0.8 Gyr (Mortlock et al. 2011). Moreover, the strong correlations between the central BH mass and global properties of the host galaxy (or spheroid) have been well-known from observations of local galaxies (e.g., Magorrian et al. 1998; Ferrarese and Merritt 2000; Gebhardt et al. 2000; Marconi and Hunt 2003; Gültekin et al. 2009). These observations imply that SMBHs and their host galaxies have co-evolved over the cosmological timescale. Revealing the origin and formation process of SMBHs has crucial impacts on various fields of astrophysics and cosmology.

Most important feature of high-z SMBH is the large BH mass ($\gtrsim 10^9\ M_\odot$). High-z QSOs which host a SMBH at the center strongly shine with the bolometric luminosity $L \gtrsim 10^{47}$ erg s^{-1}. The masse of the central SMBH are inferred as a few $\times 10^9\ M_\odot$, assuming the QSO luminosity is as large as the Eddington luminosity,

$$L_{\rm Edd} = \frac{4\pi G M_{\rm BH} c}{\kappa_{\rm T}} \simeq 1.3 \times 10^{47} \left(\frac{M_{\rm BH}}{10^9\ M_\odot} \right) \ {\rm erg\ s^{-1}}, \tag{1.1}$$

where G is the gravitational constant, c the speed of light, and $\kappa_{\rm T}$ the opacity of the Thomson scattering. The BH mass is actually estimated using the empirical relations obtained from the observations of local active galactic nucleus (e.g., the correlation between the optical luminosity at wave length of 5100 $\mathring{A}$ and the delay time of the continuum flux variability using reverberation mapping; e.g., Peterson 1993; Krolik

2001; Bentz et al. 2009). The estimated masses are almost constant as a function of the redshift and the typical value is $\sim 10^9\ M_\odot$ for $z > 4$ (Marziani and Sulentic 2012), which is consistent with the above assumption of $L \simeq L_{\rm Edd}$ for high-z QSOs. These observations suggest that high-z QSOs have been fully developed in the early universe like the low-redshift QSOs, which is also supported by the fact that the both QSOs have some common properties such as the spectra of the UV to X-ray emissions and metallicities (e.g., Fan et al. 2004; Jiang et al. 2007). Similarly, the hard X-ray observations imply that brighter QSOs (i.e., more massive BHs) have evolved earlier across the cosmic time (Ueda et al. 2003), which is so-called the cosmic downsizing. This characteristic has a property opposite to the *usual* hierarchical structure formation (see section 2.1.1) and thus is considered as a key to understand the formation process of high-z SMBHs.

As other constraints on the origin and formation process of SMBHs, the rarity of the luminous high-z QSOs has been discussed. The high-z SMBHs are expected to be harbored by massive dark matter halos with mass of $\gtrsim 10^{12-13}\ M_\odot$ since the number density is as small as $\sim 1\ \rm Gpc^{-3}$. Since such massive halos are formed from 4-5 σ peaks of the density perturbations, the high-z SMBHs are extremely rare objects in the framework of the cosmological structure formation. This fact probably suggests that most seed BHs hardly grow up to $\gtrsim 10^9\ M_\odot$ or that a small number of very massive seed BHs are formed in the early universe. Tanaka and Haiman (2009) have found that optimistic scenarios of the seed production and growth process required to explain the high-z SMBH overproduce the less massive BHs ($\lesssim$ a few $\times 10^7\ M_\odot$). Therefore, some feedback mechanisms which prevent the seed formation or BH growth are needed. Furthermore, feedback mechanisms are expected to be closely related with the correlations between the BH mass and the host spheroid (e.g., Silk and Rees 1998). As seen above, the existence of high-z SMBH connects various phenomena and physical processes, and thus the scenarios to explain their origin are required to be consistent with all observational facts.

1.2 Growth processes of SMBHs

The existence of such SMBHs formed within $\lesssim 1$ Gyr from Big Bang (e.g., Fan 2006) poses serious constraints on their formation and evolution scenarios. Several authors have studied models for the SMBH growth by gas accretion and merger (e.g., Haiman and Loeb 2001; Volonteri et al. 2003; Li et al. 2007; Tanaka and Haiman 2009), starting from ordinary-massive BHs with $10 - 100\ M_\odot$, which are remnants of first generation of stars. However, various negative feedbacks prohibit their rapid growth. As an alternative solution, massive seed BH formation ($\gtrsim 10^5\ M_\odot$) formed by the direct collapse of supermassive stars. We here review theoretical studies about the SMBH growth process (gas accretion and merger) in section 1.2.1 and 1.2.2, and the recent alternative scenario of the massive seed formation in section 1.2.3.

1.2.1 Gas accretion

We first consider the BH growth via gas accretion. Considering the accreting gas onto the BH has the specific angular momentum exceeding $\sim r_{\rm ISCO}c$, where $r_{\rm ISCO}$ is the radius of the innermost stable circular orbit, an accretion disk is formed around the BH because of the centrifugal barrier. In the disk, the gas accretes to the central BH releasing the gravitational energy as the radiation by transporting the angular momentum via the viscous friction. Assuming that portion of the gas rest-mass energy is converted to the radiation, the luminosity of the disk is written by $L = \epsilon \dot{M}_{\rm BH}c^2$, where $\dot{M}_{\rm BH}$ is the accretion rate and ϵ is the radiative efficiency which depends on the properties of the central BH and accretion disk. The typical value is estimated as $\epsilon \simeq 0.06$ for a non-rotating (schwarzschild) BH and $\epsilon \simeq 0.4$ for a maximally rotating BH and prograde disk (e.g., Shapiro and Teukolsky 1983).

From the luminosity function of bright QSOs, the mass density of the gas accreting onto the bright QSOs is estimated as $\rho_{\rm BH} \simeq (2-4)\times 10^5\ (\epsilon/0.1)^{-1}\ M_\odot\ {\rm Mpc}^{-3}$, assuming the QSO luminosity is given by $L = \epsilon \dot{M}_{\rm BH}c^2$. On the other hand, the mass density of the local BH (non-active phase) is also estimated as $\rho_{\rm BH} \simeq (3-6)\times 10^5\ M_\odot\ {\rm Mpc}^{-3}$. Since the two values are similar, thus the bright QSOs at high-z universe are inferred to grow via gas accretion at the radiative efficiency of $\sim 10\%$. This estimation suggests that the gas accretion is the dominant process of the SMBH growth in the early universe (e.g., Soltan 1982; Yu and Tremaine 2002; Marconi et al. 2004). We here note that this argument is valid for the average BH growth. many authors have considered other processes of the SMBH growth by merger (see section 1.2.2) or (low radiative efficiency) super-Eddington accretion (e.g., Begelman 1978; Abramowicz et al. 1988; Ohsuga et al. 2005).

Next, we estimate the initial conditions required to form the SMBH with $\sim 10^9\ M_\odot$ until $z \sim 6$. We here consider the case of $L = L_{\rm Edd}$ (if $L > L_{\rm Edd}$, the outward radiation pressure force exceeds the gravity of the central BH and thus the gas accretion is prohibited). Under this conservative assumptions of the constant radiative efficiency, the growth of the BH mass is simply described by

$$\frac{dM_{\rm BH}}{dt} = (1-\epsilon)\dot{M}_{\rm Edd} = \frac{1-\epsilon}{\epsilon}\frac{M_{\rm BH}}{t_{\rm Edd}}, \tag{1.2}$$

where $\dot{M}_{\rm Edd} = L_{\rm Edd}/(\epsilon c^2)$ is the Eddington accretion rate and $t_{\rm Edd} = M_{\rm BH}c^2/L_{\rm Edd} \simeq 0.45$ Gyr. From this equation, the BH mass is expressed as a function of the time,

$$M_{\rm BH}(t) = M_{\rm BH}(t_0)\exp\left(\frac{1-\epsilon}{\epsilon}\frac{t-t_0}{t_{\rm Edd}}\right), \tag{1.3}$$

where $M_{\rm BH}(t_0)$ is the seed BH mass and t_0 the initial time when the gas accretion begins. As an example, considering a seed BH formed at $z = 20$ ($t_0 \simeq 0.2$ Gyr), the required seed mass to form the observed SMBHs ($\sim 10^9\ M_\odot$) until $z = 6$ is estimated as $\gtrsim 10^2\ M_\odot$ for $\epsilon = 0.1$. Recent simulations suggest that first generation stars (so-called Pop III stars) are ordinary massive star with $10 - 10^2\ M_\odot$ (Hosokawa et al. 2011; Stacy et al. 2012; Hirano et al. 2013). Thus, the remnant BHs of Pop III stars could be the promising seed BHs which manage to achieve the SMBH formation until $z \sim 6$. For more distant QSOs ($z \gtrsim 6$), the additional assumptions (e.g., super-Eddington accretion or low radiative efficiency) are needed to explain their formation.

In the above rough discussion, only the idealized situations for the BH growth are considered. To evaluate the BH growth more accurately, the negative feedbacks due to the radiation from the central accretion disk must be discussed. Milosavljević et al. (2009) investigated the gas structure of the accretion flows near the remnant BH ($\sim 10^2\ M_\odot$) of Pop III stars at the range of $10^2 - 10^3$ AU, performing the hydrodynamical numerical simulation. The accretion onto the central BH occurs episodically rather than the continuous accretion. The resultant accretion rate is lower than the Eddington accretion rate by one order of magnitude because of the strong radiative force. The photo-ionization and heating due to the accretion disk also reduces the accretion rate from the larger scale ($\sim$ 1 kpc) to the central region, whose rate is smaller than the Eddington rate by several orders of magnitude (Alvarez et al. 2009; Jeon et al. 2012). This is because the accretion rate in the outer-region is limited by the Bondi rate, $\dot{M}_{\rm BH} \simeq G^2 M_{\rm BH}^2\ \rho/c_s^3 \propto T_{\rm gas}^{-3/2}$, where ρ, c_s and $T_{\rm gas}$ are the density, speed of sound, and temperature of the ambient gas, respectively. Thus, the radiative heating strongly decreases the accretion rate, which results the SMBH growth time much longer than that estimated by equation (1.3). To understand the SMBH growth via gas accretion, it is required to investigate the global properties of gas inflows over the wide spacial scale. Recent simulation by Di Matteo et al. (2012) have performed the cosmological simulations considering the hierarchical structure formation and BH growth consistently. They have concluded that assuming a massive seed BH with $\sim 10^5\ M_\odot$, the seed BH can grow to supermassive until $z \sim 6$ fed by cold gas inflow due to the galaxy formation.

1.2.2 BH merger

As another process of the BH growth, the BH merger has been considered. When the galaxies hosting BHs at the center merge, the BHs loses the orbital angular momentum and finally could merge each other. The key point for this process is how the angular momentum of the binary BH is extracted. After the galaxy merging, the binary BH sinks to the galaxy center and its orbit shrink because of the dynamical friction and the three-body (or multi-body) encounter with the surrounding stars. Begelman et al. (1980) pointed out that the orbital decay time becomes much longer than the Hubble time at the binary separation of $\sim$ 1 pc because the number of the stars which receive the angular momentum of the binary BH decreases. This is called final parsec problem, which has been considered to be a crucial problem. However, some authors thereafter found that the extraction of the orbital angular momentum of the binary BH works effectively and thus the separation could shrink to $\ll 1$ pc in the non-spherical (i.e., axisymmetric or triaxial) or non-static potential (e.g., Yu 2002; Merritt and Poon 2004). Moreover, the transport of the binary angular momentum to the circumbinary disks, which is expected to form in the gas-rich galaxy, has been also considered (e.g., Armitage and Natarajan 2002; Milosavljević and Phinney 2005; Hayasaki et al. 2007; MacFadyen and Milosavljević 2008; Cuadra et al. 2009; Haiman et al. 2009). Once the binary orbit decays sufficiently, the gravitational radiation becomes the main process transporting the orbital angular momentum. Then, the orbital decay time caused by the gravitational wave emission is estimated as

$$t_{\rm GW} \simeq 0.25 \ {\rm Gyr} \left(\frac{a}{0.2 \ {\rm AU}}\right)^4 \left(\frac{M_{\rm BH}}{10^2 \ M_\odot}\right)^{-3}, \tag{1.4}$$

where a is the binary separation and we assume the circular orbit of the equal-mass binary BH. For the ordinary massive BHs ($\sim 10^2 \ M_\odot$), the very close binary of $a \lesssim 1$ AU is at least required to merge within the age of the universe at $z \gtrsim 10$ (~ 0.5 Gyr).

Even if the binary coalescence occurs by emitting the gravitational wave, there remains other difficulties of the BH growth in the early universe. When the two BHs have unequal mass or spins, the strong gravitational wave is emitted to a definite direction. Then, the coalesced BHs receive the momentum and thus are recoiled in the opposite direction of the gravitational wave emission. The recoil velocity depends on the mass ratio and their spin configurations (amplitudes and directions) and is typically $v_{\rm recoil} \geq 100$ km s^{-1} (Herrmann et al. 2007; Koppitz et al. 2007) In the case of the untiparallel spins, it can reach as high as 4×10^3 km s^{-1} (Campanelli et al. 2007). As we see in next chapter, typical haloes in a high-redshift universe tend to be low mass and their escape velocity ($\sim$ a few $\times 10$ km s^{-1}) is smaller than the recoil velocity. If BHs are ejected from their host haloes in merging events, the BH growth process must repeat again from scratch, which results in the suppression of the BH growth through the merger events.

1.2.3 Alternative scenarios

As a solution to this, the alternative possibility of massive seed BH formation by the direct collapse of supermassive stars (SMSs: $\gtrsim 10^5 \ M_\odot$) has been considered by some authors. The evolution and general relativistic instability of SMSs have been investigated by many authors (Chandrasekhar 1964a,b; Zeldovich and Novikov 1971; Shapiro and Teukolsky 1983). Among them, Shibata and Shapiro (2002) calculated the collapse of a rotating SMS into a SMBH and found that most of the mass originally in the SMS is eventually locked in the BH ($M_{\rm BH} \simeq 0.9 \ M_{\rm SMS}$). This massive seed BH as a remnant of SMS collapse reduces the growth time to $\gtrsim 10^9 \ M_\odot$ within 0.46 Gyr, which is as long as $t_{\rm Edd}$ and mitigates the growth-time problem by a big margin.

To form SMSs in the cosmological context, the two key physics have been discussed; (1) angular momentum barrier and (2) fragmentation and star formation. Through the hierarchical structure formation, a collapsing object is exerted the tidal torque from neighboring density perturbations (Peebles 1969; Doroshkevich 1970; Efstathiou and Jones 1979; White 1984). If the gas has the angular momentum enough to form disks, the fragmentation could be effectively promoted and thus massive objects are hardly formed. The early studies discussed the extraction of the angular momentum of the gas through the Compton frictions with the cosmic microwave background (CMB) radiation (Loeb 1993; Umemura et al. 1993) and due to the non-axisymmetric spiral structures caused by the gravitational instability (Shlosman et al. 1989, 1990; Loeb and Rasio 1994; Begelman and Shlosman 2009). Furthermore, the possibility that SMSs and SMBHs are formed in halos with low spin angular momentum has been also proposed (Eisenstein and Loeb 1995).

Thereafter, formation of SMSs and their subsequent collapse directly to the BHs in the protogalaxies ($z \gtrsim 10$ and $T_{\rm vir} \gtrsim 10^4$ K) has been envisaged (e.g., Bromm and Loeb 2003; Begelman et al. 2006; Lodato and Natarajan 2006). Here, primordial gas clouds more massive than $10^5\ M_\odot$ are supposed to contract monolithically to form stars without strong fragmentation. Since rapid H_2 cooling, which is the main cooling process in the early universe, causes fragmentation of the primordial gas cloud, for the SMS formation, suppression of H_2 formation is required by some means. Examples of such means are: the photodissociation by far-ultraviolet radiation from nearby stars (e.g., Omukai 2001; Bromm and Loeb 2003; Omukai et al. 2008; Regan and Haehnelt 2009a,b; Shang et al. 2010; Johnson et al. 2011; Inayoshi and Omukai 2011; Agarwal et al. 2012; Johnson et al. 2013), and the collisional dissociation in dense and hot gas (Inayoshi and Omukai 2012). As other process suppressing fragmentation, the gas heating by the ambipolar diffusion of the primordial magnetic field has been also considered (Sethi et al. 2010). In all cases, the primordial gas collapses isothermally at $T \sim 8000$ K via H atomic cooling (Omukai 2001) and no major fragmentation is observed in numerical simulations during this phase (Bromm and Loeb 2003; Regan and Haehnelt 2009a,b). In chapter 2, we describe the SMS formation process and its difficulties in more detail.

1.3 Organization of this thesis

This thesis is organized as follows. Chapter 2 is devoted to reviews of previous works, and our works are described in the remaining chapters.

In chapter 2, we review the formation of galaxies and stars in the early universe. Among them, we focus on the formation of supermassive stars as seeds of the observed high QSOs.

In chapter 3 and 4, we present the discussion of our two papers:

- K. Inayoshi and K. Omukai, "Effect of cosmic ray/X-ray ionization on supermassive black hole formation," Monthly Notices of the Royal Astronomical Society, 416, 2748 (2011).

- K. Inayoshi and K. Omukai, "Supermassive black hole formation by cold accretion shocks in the first galaxies," Monthly Notices of the Royal Astronomical Society, 422, 2539 (2012).

We investigate the formation scenario of supermassive clouds in the high-z galaxies. First, we mention about negative feedback on the supermassive star formation due to the cosmic rays / X-rays. Next, we propose a new scenario to form supermassive stars which is consistent with the galaxy formation. Our scenario does not assume the strong far-ultraviolet radiation, which is required in the previous studies.

In chapter 5, we show the results of numerical simulations about the subsequent collapse of a supermassive cloud. This study is still unpublished. Nevertheless, we discuss it because the collapse phase (e.g., efficiency of fragmentation) is the most important topic in the supermassive star formation.

In chapter 6 and 7, we present the discussion of our two papers:

- K. Inayoshi, T. Hosokawa, and K. Omukai, "Pulsational instability of supergiant protostars: do they grow supermassive by accretion?," Monthly Notices of the Royal Astronomical Society, 431, 3036 (2013).

- T. Hosokawa, H. W. Yorke, K. Inayoshi, K. Omukai, and N. Yoshida, "Formation of Primordial Supermassive Stars by Rapid Mass Accretion" The Astrophysical Journal, 778, 178 (2013).

We investigate the evolution and stability of the supermassive star under the protostellar phase. We also discuss whether the protostar can grow up to a supermassive star via rapid accretion.

In the last chapter, we summarize our results and discuss future works.

Chapter 2

Supermassive star formation in the first galaxies: Overview

In this chapter, we overview the formation of supermassive stars (SMSs), which could evolve to seeds of SMBHs in the high-z universe. In section 2.1, the formation of first galaxy, which is the first object forming many stars in the universe, is briefly described. Stars formed in the first galaxies are affected by the stellar activities of stars born before (e.g., ultra-violet radiation, cosmic rays, X-rays, and supernovae). In section 2.2, the SMS formation from primordial gas irradiated by strong far ultraviolet (FUV) radiations is discussed. The probability of the SMS formation due to strong FUV in the early universe are reviewed in section 2.3. Finally, we review the evolution of the protostellar phase of SMSs in section 2.4.

2.1 Formation of first galaxies

2.1.1 Structure formation

In the present-day universe, there are many structures over the various spacial range from galaxy clusters to the solar system. Our current understanding of the structure formation is base on the Λ cold dark matter (CDM) model, which is supported by observations of the cosmic microwave background (CMB), galaxy distribution, type Ia supernovae (e.g., Riess et al. 1998; Perlmutter et al. 1999; Spergel et al. 2003; Knop et al. 2003; Eisenstein et al. 2005; Kowalski et al. 2008; Komatsu et al. 2009). The ΛCDM model suggests that the large-scale structure has been hierarchically formed via growth of density fluctuations with smaller scale. As the amplitude of the density fluctuations increases to the non-linear regime, the DM collapses and reaches an equilibrium state, a so-called virial equilibrium. According to many numerical simulations of the cosmological structure formation (e.g., Springel et al. 2005), DM halos merge each other and form filamentary structure, which results in the assembly of more massive halos in the intersections of the filaments. Although the properties of such complex structures are difficult to describe analytically, we can roughly understand them assuming the spherical collapse of matters. By this assumption of the non-linear theory of the density perturbations, the radius of the virialized DM halo is estimated as

$$R_{\mathrm{vir}} = 0.784 h^{-1}\ \mathrm{kpc} \left(\frac{M}{10^8 h^{-1}\ M_\odot}\right)^{1/3} \left(\frac{\Omega_m}{\Omega_m^z}\frac{\Delta_c}{18\pi^2}\right)^{-1/3} \left(\frac{1+z}{10}\right)^{-1}, \tag{2.1}$$

where M is the halo mass, z the redshift at the virialization,

$$\Delta_c = 18\pi^2 + 82(\Omega_m^z - 1) - 39(\Omega_m^z - 1)^2, \tag{2.2}$$

and

$$\Omega_m^z = \frac{\Omega(1+z)^3}{\Omega_m(1+z)^3 + \Omega_\Lambda}, \tag{2.3}$$

(Bryan and Norman 1998). From the equilibrium between the gravity and velocity dispersion, the virial temperature of the halo is defined as

$$\begin{aligned} T_{\mathrm{vir}} &= \frac{\mu m_{\mathrm{H}}}{2k_{\mathrm{B}}}\frac{GM}{R_{\mathrm{vir}}} \qquad (2.4) \\ &= 1.98\times 10^4\ \mathrm{K} \left(\frac{\mu}{0.6}\right)\left(\frac{M}{10^8 h^{-1}\ M_\odot}\right)^{2/3}\left(\frac{\Omega_m}{\Omega_m^z}\frac{\Delta_c}{18\pi^2}\right)^{1/3}\left(\frac{1+z}{10}\right), \end{aligned}$$

where μ is the mean molecular weight of the baryonic gas and m_{H} the hydrogen mass. We here note that this is the simplest description of the non-linear structure formation. Thereafter, more sophisticated formulations considering the non-spherical objects have been constructed (e.g., Sheth and Tormen 2002). Nevertheless, the spherical collapse model has been widely used because of its simplicity and accordance with a number of cosmological simulations.

Then, when and where do first galaxies form in the framework of the hierarchical structure formation? We here consider that first galaxies must be massive hosts enough to retain large amounts of gas for star formation, even if the radiative and mechanical feedbacks happen inside the galaxies. Since ionization photons (> 13.6 eV) from massive stars heat up the surrounding gas to $\sim 10^4$ K, the DM halo of the the first galaxy is required to be more massive as $T_{\mathrm{vir}} > 10^4$ K. Moreover, recurrent SNe could remove the ionized gas from the first galaxy. Many authors have investigated the propagation of the SN shock and the fate of the gas in DM halos (e.g., Mori et al. 2002; Bromm et al. 2003). For the explosion energy of $\sim 10^{51} - 10^{53}$ erg, the efficiency of the conversion to the thermal energy is not so high because of the radiative loss, depending on the density profile of the surrounding gas. Then, in more massive halos with $\gtrsim 10^7\ M_\odot$, the gas is confined by the deep gravitational potential without blowing. (e.g., Kitayama and Yoshida 2005; Greif et al. 2007; Whalen et al. 2008). In such massive halos, some kinds of the feedback effect do not prevent the subsequent star formation can actively proceed. In this paper, we define the first galaxies as massive halos with $M > 10^{7-8}\ M_\odot$ and $T_{\mathrm{vir}} > 10^4$ K (e.g., Bromm and Yoshida 2011).

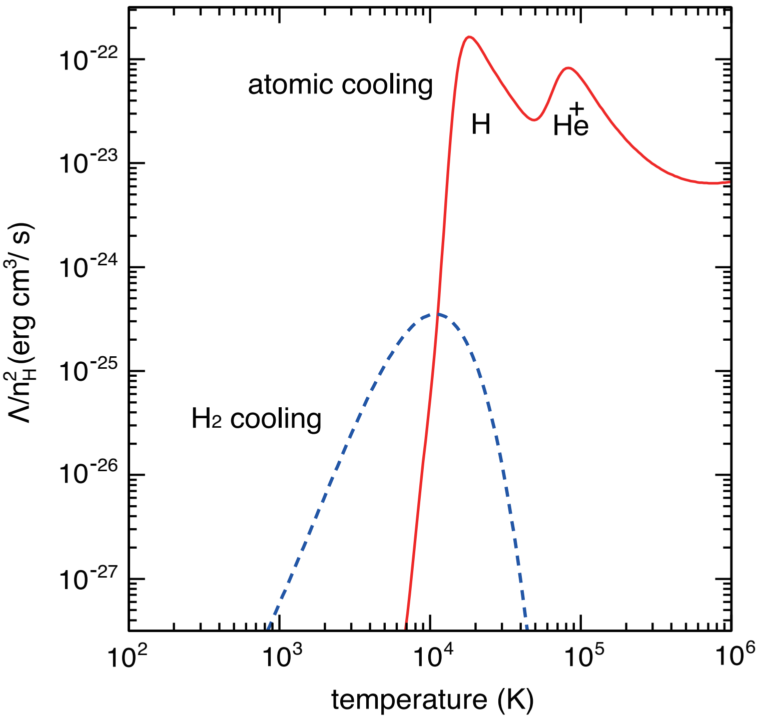

Figure 2.1: The cooling function (erg s^{-1} cm^3) of primordial gas ($Z = 0$) for atomics (solid) and H_2 molecules (dashed) as a function of the temperature. The H_2 abundance is assumed as $y(H_2) = 10^{-3}$.

2.1.2 Cold accretion flows

In the first galaxies, the gas falls into the deep gravitational potential well of the massive halo and heat up to the virial temperature $> 10^4$ K. After the virialization, the gas begins to collapse via radiative cooling and finally form stars. Figure 2.1 shows the cooling rate of primordial gas ($Z = 0$) for atomics (solid) and H_2 molecules (dashed) as a function of the temperature. The two peaks of the atomic cooling rate present the transition of H (Lyα emission; $\sim 10^4$ K) and He ($\sim 10^5$ K), respectively, wheres the H_2 cooling works for lower temperature regime ($10^3 < T < 10^4$ K) if H_2 is formed in the gas. Since the gas temperature rises to $> 10^4$ K at the center of the first galaxy, the Lyα cooling become the main cooling process. Since the cooling rate via the Lyα emission is high, the cooling time of the gas is shorter than the Hubble time (age of the universe) and thus star formation is efficiently driven in the halo, which is called the *atomic cooling halo*.

In the conventional description of the gas virialization, the gas fallen into the DM halo heats up to the virial temperature and the shocks propagate toward the virial radius. Since the cooling rate is high in the atomic cooling halos ($T_{\rm vir} > 10^4$ K), however, the behavior of the shock propagation should change depending on the cooling

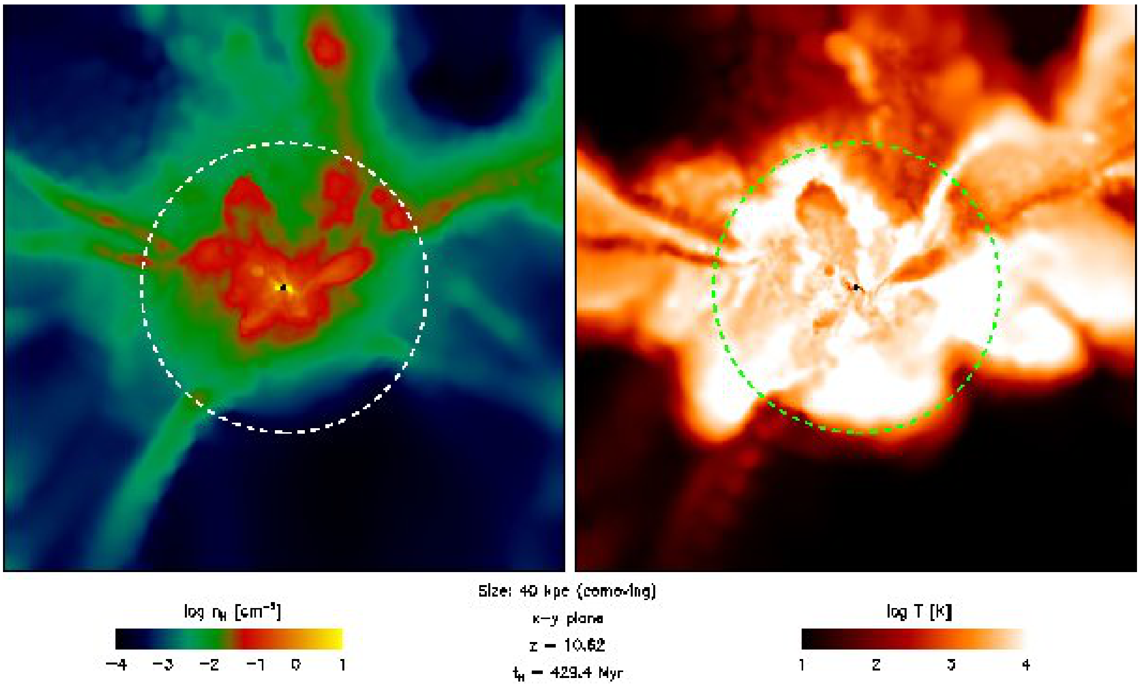

Figure 2.2: The density (left) and temperature (right) of the primordial gas collapsing into an atomic cooling halo at $z \simeq 10$. The dashed lines show the size of the the virial radius (~ 1 kpc). Since the shock position shrinks inside the virial radius owing to efficient Lyα cooling, the accreting cold gas penetrates deep to the centre through dense filamentary flows. This figure is taken from Greif et al. (2008).

time. According to the linear stability analysis by Birnboim and Dekel (2003) and Dekel and Birnboim (2006), the post-shock region with radiative cooling is unstable against the self-gravity when the post-shock pressure and density are satisfied with

$$\gamma_{\rm eff} \equiv \frac{\dot{P}}{P}\frac{\rho}{\dot{\rho}} < \frac{2\gamma}{\gamma + \frac{2}{3}}, \tag{2.5}$$

where $\gamma_{\rm eff}$ is the effective adiabatic index with radiative cooling and $\gamma = (\partial \ln P/\partial \ln \rho)_{\rm ad}$. For a monotonic gas ($\gamma = 5/3$), $\gamma_{\rm eff} = 10/7$. We note that this stability condition is equivalent to $\gamma < 4/3$, which is the condition for an adiabatic sphere given by the virial theorem, if $\gamma_{\rm eff} = \gamma$ (i.e., no cooling). When we rewrite the stability condition using the energy conservation

$$\dot{e} = \frac{P}{\rho^2}\dot{\rho} - \frac{\Lambda}{\rho}, \tag{2.6}$$

we obtain

$$\begin{aligned} \gamma_{\rm eff} &= \gamma - \frac{\Lambda}{\rho e}\frac{\rho}{\dot{\rho}}, \\ &\equiv \gamma - \frac{t_{\rm comp}}{t_{\rm cool}}, \end{aligned} \tag{2.7}$$

where $\cdot$ is the Lagrange time derivative, e the specific energy, Λ the cooling rate, $t_{\rm comp} = \rho/\dot{\rho}$ the compression time scale, $t_{\rm cool} = \rho e/\Lambda$ the cooling time scale. Therefore, we find the condition (2.5) roughly means that the radiative cooling in the post-shock region exceeds the energy deposit due to the accretion flows (i.e., $t_{\rm cool} \lesssim t_{\rm comp}$). Assuming that the post-shock velocity is proportional to the radius (Birnboim and Dekel 2003), the compression time is expressed as

$$t_{\rm comp} = -\frac{1}{r^2}\frac{\partial}{\partial r}(r^2 u) = -\frac{3u_2}{r_{\rm sh}}, \tag{2.8}$$

where $u(r) = u_2(r/r_{\rm sh})$, and u_2 $r_{\rm sh}$is the post-shock velocity and $r_{\rm sh}$ the position of the shock. Since the pre-shock velocity is simply written as $u_1 = u_2(\gamma+1)/(\gamma-1)$ under strong shock limit when the shock does not move, $t_{\rm comp} \sim u_1/r_{\rm sh}$. Thus, we obtain the critical value of the cooling function ($\bar{\Lambda} = \Lambda/n_{\rm H}^2$, where $n_{\rm H}$ is the number density of hydrogen nuclei) as a function of quantities in the pre-shock flow,

$$\bar{\Lambda} > \bar{\Lambda}_{\rm crit} \sim 0.02\,\frac{m_{\rm H}^2|u_1|^3}{\rho_1 r_{\rm sh}}. \tag{2.9}$$

Assuming $r_{\rm sh} \simeq R_{\rm vir}$ and $u_1 \simeq \sqrt{2GM/R_{\rm vir}}$, we estimate the critical value $\bar{\Lambda}_{\rm crit} \simeq 2.4 \times 10^{-25}$ erg s^{-1} cm^3 for the atomic cooling halo ($M \simeq 10^8\ M_\odot$ and $z \simeq 10$), which is much less than the value for the Lyα emission ($\gtrsim 10^{-23}$ erg s^{-1} cm^3) shown in Figure 2.1. Therefore, since the post-shock gas is gravitationally unstable for the gas in the atomic cooling halo, the virial shocks do not propagate outward and instead shrinks within the virial radius, which result in the different description of the galaxy formation from the conventional ones.

Recent numerical simulations of galaxy formation have revealed that in the atomic cooling halos ($T_{\rm vir} > 10^4$ K), the shock position does not stay at the virial radius and shrinks inside owing to efficient Lyα cooling. As seen in Figure 2.2, the accreting cold gas penetrates deep to the centre through dense filamentary flows (Birnboim and Dekel 2003; Kereš et al. 2005; Dekel and Birnboim 2006; Dekel et al. 2009; Bromm and Yoshida 2011). The supersonic flows form the core supported by the kinetic energy of turbulence with high Mach number. The turbulent flows collide each other and the resultant shock develops a hot and dense ($T \gtrsim 10^4$ K and $n \gtrsim 10 - 10^3$ cm^{-3}) gas near the centre (Wise and Abel 2007; Greif et al. 2008; Wise et al. 2008). This cold accretion flows could effectively drive star formation by suppling the gas into the central region.

2.2 Star formation of second generation stars

In this section, we consider formation of 2nd generation stars, which are affected by stellar feedbacks from stars born before. The very first stars (so-called Pop III stars) would be more massive ($\sim 100\ M_\odot$) and hotter ($T_{\rm eff} \sim 10^5$ K) than Pop I/II stars in present-day because of the absence of the metals (e.g., Marigo et al. 2001, 2003).

Therefore, Pop III stars emit a large amount of UV photons and have influences on the subsequent star formation. In what follows, we reviewed the development of the UV radiation background in the early universe (section 2.2.1), star formation under UV radiations (section 2.2.2), and formation of SMSs as a special case (section 2.2.3 and 2.2.4).

2.2.1 UV radiation background in the early universe

Pop III stars emit a large amount of UV photons since they are massive stars and have hot atmosphere. The typical effective temperature is so high ($T_{\rm eff} \sim 10^5$ K) that the spectrum of the galaxies including many Pop III stars is much different from that of Pop I/II galaxies. Remarkably, a large number of the ionizing photon ($h\nu \geq 13.6$ eV) is emitted from Pop III galaxies compared to that of Pop II/I galaxies. Such ionizing photons from Pop III galaxies are expected to ionize the neutral hydrogens in the intergalactic medium (IGM) and thus proceed the cosmic re-ionization. The size of the ionization region is limited by the balance between the ionization and recombination. On the other hand, since photons with energy lower than 13.6 eV does not contribute the ionization of H and He, they propagate outside the ionization radius. Among them, the far UV (FUV) photons at the Lyman-Werner band ($11.2{\rm eV} \leq h\nu \leq 13.6{\rm eV}$) dissociate H_2 molecules via

$$\mathrm{H_2} + \gamma \rightarrow 2\mathrm{H}. \tag{2.10}$$

Therefore, the photo-dissociation regions of H_2 molecules can expand outside the ionization regions. In other words, the background of FUV photons dominates before the ionization regions develop enough to achieve the cosmic re-ionization. The development of the UV radiation background at the initial epoch of cosmic reionization has been studied by Haiman et al. (1997), assuming the the intrinsic radiation spectrum (i.e., before absorptions) as

$$J(\nu) = J_{21} \times 10^{-21} \left(\frac{\nu}{\nu_{\rm L}}\right)^{-1} \ {\rm erg\ s^{-1}\ cm^{-2}\ sr^{-1}\ Hz^{-1}}, \tag{2.11}$$

where $h\nu_{\rm L} = 13.6$ eV and J_{21} is the intensity of photons at the Lyman limit ($\nu_{\rm L}$). Since ionizing photons ($h\nu \geq 13.6$ eV) are strongly absorbed by neutral H and He, the UV background is developed by low energy photons. Most of the FUV photons also contribute to the background radiations even in the face of the absorption due to the H lines (e.g., Lyman series).

The average intensity of FUV radiation background is roughly estimated as a function of the star-formation rate (SFR) per comoving volume $\Psi_*(z)$ and redshift z (Greif and Bromm 2006),

$$J_{\rm LW} \simeq \frac{hc}{4\pi m_{\rm H}} \left(\frac{\bar{\nu}}{\Delta\nu}\right) \eta_{\rm LW} \rho_*(z)(1+z)^3, \tag{2.12}$$

where h is the Planck constant, c the speed of light, $\bar{\nu}$ the average frequency of the LW band ($h\bar{\nu} = 12.4$ eV), $\Delta\nu$ the LW band width ($h\Delta\nu = 2.4$ eV), $\eta_{\rm LW}$ the number of FUV photons radiated per Pop III stellar baryon, ρ_* the stellar mass density producing the background FUV photons. Johnson et al. (2013) evaluated $\rho_*(z)$ from $\rho_*(z) = \Psi_*(z)t_*$, where t_* their lifetime ($\sim$ 5 Myr). Then, equation (2.12) is rewritten as

$$J_{21} \simeq 0.2 \left(\frac{\eta_{\rm LW}}{10^4}\right) \left(\frac{\Psi_*(z)}{10^{-3}\ M_\odot\ {\rm yr}^{-1}\ {\rm Mpc}^{-3}}\right) \left(\frac{1+z}{10}\right)^3 . \tag{2.13}$$

$\eta_{\rm LW}$ is estimated as $\simeq 2 \times 10^4$ for Pop III stars with a top-heavy IMF and $\simeq 4 \times 10^3$ for Pop I/II stars with a Salpeter-like IMF, respectively (Schaerer 2002).

When the FUV radiation background develops, H_2 molecules are photo-dissociated in minihalos of $M \sim 10^6\ M_\odot$ and $T_{\rm vir} \sim 10^3$ K, which results in strong suppression of further star formation (Haiman et al. 1997). As the intensity of the FUV background increases, the mass threshold of the DM halo where the star formation can take place increases as $M = (1.25 + 8.7 J_{21}) \times 10^5\ M_\odot$ (Machacek et al. 2001) and thus the epoch of star formation delays. Moreover, Omukai and Nishi (1999) show that a massive Pop III star totally photo-dissociate the H_2 molecules in their own minihalo. In the both cases, H_2 molecules in minihalos are easily dissociated by the FUV radiation emitted from Pop III stars, which prevents the subsequent star formation. Even if the FUV background develops to $J_{21} > 0.04$, star formation is led by the H atomic cooling in massive halos of $M > 10^7\ M_\odot$ and $T_{\rm vir} \gtrsim 10^4$ K (O'Shea and Norman 2008).

2.2.2 Thermal evolution of the irradiated primordial gas

As the FUV radiation background is built up over the IGM, star formation from primordial gas is affected by the H_2 photo-dissociation process. Figure 2.3 presents the thermal evolution of a cloud irradiated with the FUV radiations for various intensities ($0 \leq J_{21} \leq 10^5$). The FUV spectrum is assumed to be the power law, $J(\nu) \propto \nu^{-1}$, given by equation (2.11).

First we see the case of no-FUV ($J_{21} = 0$), where the cloud collapses along the standard H_2-cooling track (e.g., Palla et al. 1983). Following the initial adiabatic rise up to $\sim$ 1000 K, the temperature starts decreasing owing to the H_2 cooling. H_2 molecules are produced through the H^- channel,

$$\mathrm{H} + \mathrm{e}^- \rightarrow \mathrm{H}^- + \gamma, \tag{2.14}$$

$$\mathrm{H}^- + \mathrm{H} \rightarrow \mathrm{H}_2 + \mathrm{e}^-, \tag{2.15}$$

until the critical density $\simeq 10^4$ cm^{-3}, where the H_2 level-populations reach the local thermodynamic equilibrium (LTE) and the cooling rate per unit mass saturates. The temperature thereafter increases again gradually by the compressional heating towards higher density. Addition of a FUV field affects the evolution in the following way. As seen in the cases with $J_{21} \leq 10^2$, with increasing radiation intensity, the initial adiabatic phase continues until higher density and temperature, where the H_2 column density becomes high enough for efficient self-shielding against photodissociation. Once

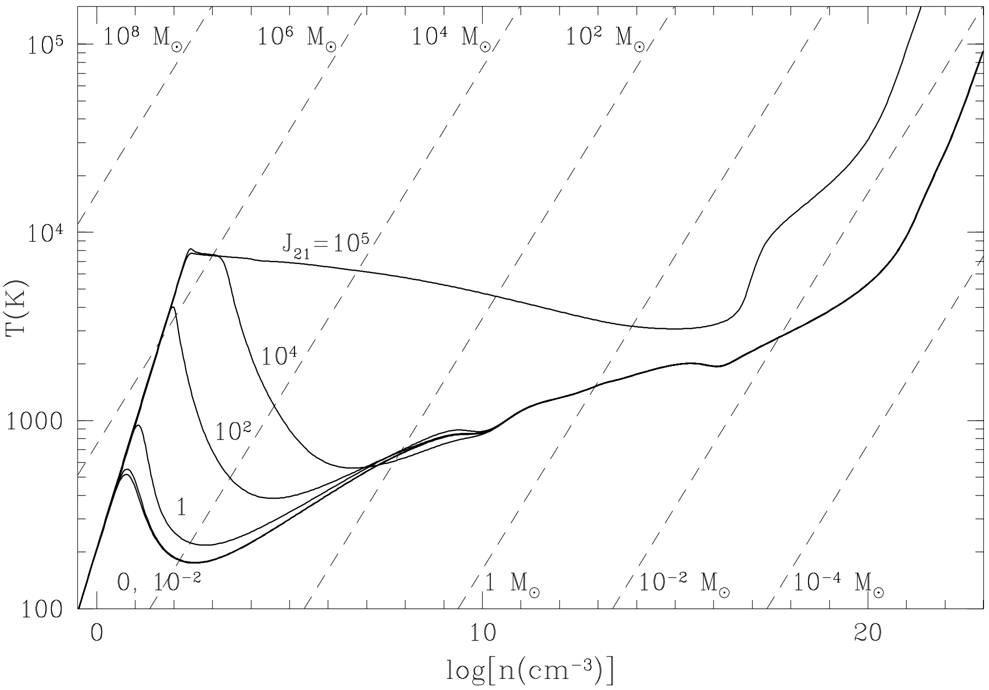

Figure 2.3: Density-temperature diagram of primordial gas irradiated with FUV radiations for $J_{21} = 0$, 10^{-2}, 1, 10^2, 10^4, and 10^5. For $J_{21} \leq 10^4$, the gas cools and collapses via H_2 line cooling ($T \sim 1000$ K), wheres the gas collapses isothermally keeping high temperature ($T \sim 8000$ K). This figure is taken from Omukai (2001).

the H_2 cooling becomes effective, the temperature decreases and gradually converges to the track in the no-FUV case. For $J_{21} = 10^4$, before the onset of H_2 cooling, the temperature reaches $\simeq 8000$ K and stays almost constant around 10^3 cm^{-3} owing to the H Lyα cooling. This short isothermal phase is followed by a rapid temperature drop by the H_2 cooling. As in the cases with lower FUV fields, the temperature converges towards the no-FUV track.

On the other hand, when a FUV field exceeds a critical value $J_{21} \geq 10^5$, the temperature evolution is qualitatively altered. The isothermal evolution at $\simeq 8000$ K continues until very high density ($\sim 10^{16}$ cm^{-3}) and the H_2 cooling never becomes important. This bifurcation of thermal evolution originates from the fact that if the H_2 formation is prevented until the critical density for LTE, sufficient H_2 never forms because, at higher density, (i) the amount of H_2 needed for cooling increases (ii) collisional dissociation from the excited ro-vibrational levels of H_2 becomes effective, which reduces the H_2 fraction (Omukai 2001).

Figure 2.4 shows the dominant cooling and heating processes in the gas for the case of $J_{21} = 10^5$. As the isothermal collapse proceeds until $> 10^6$ cm^{-3}, the dominant cooling process changes to two-photon emissions (the transition line from the 2s state

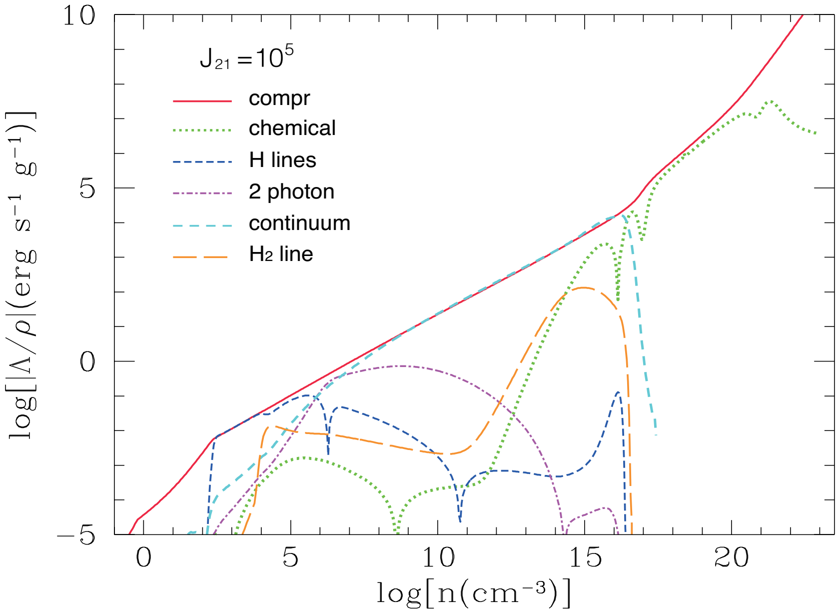

Figure 2.4: Heating and cooling rate (erg s^{-1} g^{-1}) of primordial gas irradiated with FUV radiations for $J_{21} = 10^5$ as a function of the gas density. Each line presents the compressional heating (solid), chemical heating/cooling (dotted), H line emission (short-dashed), two photon emissions (dot-dashed), continuum cooling (dashed), H_2 line emissions (long-dashed). This figure is taken from Omukai (2001).

to 1s state of atomic hydrogen) because the Lyα emission becomes optically thick. For the density higher than 10^8 cm^{-3}, the continuum cooling (the free-bound and free-free emissions of H^- ions) dominates and leads further collapse until $n \sim 10^{16}$ cm^{-3}. Finally, the gas becomes completely optically thick for $n > 10^{16}$ cm^{-3} and thus the adiabatically hydrostatic core forms at the center of the cloud. The mass of the formed protostar is estimated as the Jeans mass at the epoch of the formation of the adiabatic core $\sim 0.03\ M_\odot$, which is somewhat larger than that in formation of usual Pop III stars.

2.2.3 The value of the critical FUV intensity

With the FUV flux increasing and reaching a threshold value, the thermal evolution of the irradiated primordial gas *does* change. The value of the critical FUV intensity, $J_{\rm crit}$, has been studied by several authors (Omukai 2001; Bromm and Loeb 2003; Shang et al. 2010; Inayoshi and Omukai 2011; Wolcott-Green et al. 2011). Since the star-forming galaxies and mini-quasars as sources of FUV radiations, some kinds of the FUV spectrum are often assumed to have a diluted thermal spectrum, $J(\nu) \propto B_\nu(T_*)$, with brightness temperature $T_* = 10^4$ and 10^5 K, corresponding to that from assembly of metal-enriched stars or massive Pop III stars, respectively, and a power-law $J(\nu) \propto \nu^{-1}$.

The values of the critical FUV flux are $J_{\rm crit,21} \simeq 10^3$ (for $T_* = 10^4$ K) and $J_{\rm crit,21} \simeq 10^5$ ($T_* = 10^5$ K and power-law), respectively, by an one-zone model (Omukai 2001) and three-dimensional hydrodynamical simulation (Bromm and Loeb 2003). For the same value of J_{21} at the Lyman limit, the rate of $\rm H_2$ photodissociation, which proceeds via absorption of photons of $11.2 - 13.6$ eV does not vary so much for different values of T_*. On the other hand, the rate of $\rm H^-$ photodissociation,

$$\rm H^- + \gamma \rightarrow H + e^-, \tag{2.16}$$

whose threshold energy (0.755 eV) is far below the Lyman limit, is significantly affected with change of T_* even with the same J_{21}. For example, this rate is 2×10^4 times higher for $T_* = 10^4$ K than that for $T_* = 10^5$ K with the same J_{21}. Since $\rm H^-$ is the intermediary in the $\rm H_2$-forming reaction (equation 2.14 and 2.15), the $\rm H_2$ concentration depends sensitively on T_*.

Subsequently, Shang et al. (2010) performed three-dimensional hydrodynamical simulations and studied the dependence of the critical FUV flux on the radiation spectrum. They suggested that the value of $J_{\rm crit}$ alleviates more than expected in the previous works, because the reaction rate of the $\rm H_2$ collisional dissociation

$$\rm H_2 + H \rightarrow 3H, \tag{2.17}$$

is previously underestimated around the $\rm H_2$ LTE, which results in $30 < J_{\rm crit,21} < 300$ ($10^4 < J_{\rm crit,21} < 10^5$) for the diluted thermal spectrum with $T_* = 10^4$ K (10^5 K, respectively) depending on the properties of host halos. Moreover, Wolcott-Green et al. (2011) improved the effect of the $\rm H_2$ self-shielding against the FUV radiations from a simple fitting formula given by Draine and Bertoldi (1996). Using the new $\rm H_2$ shielding factor, the critical FUV flux for $T_* = 10^5$ K is reduced by an order of magnitude to $J_{\rm crit,21} \simeq 10^4$ (Inayoshi and Omukai 2011; Wolcott-Green et al. 2011)

2.2.4 Supermassive star formation

As you see in the previous section, the strong FUV radiation dramatically change the thermal evolution of primordial gas. How do the differences affect the properties of protostars formed at the center of the cloud? The dependence of gas fragmentation on the thermal state has been studied by many authors using both of the analytical arguments and numerical simulations (e.g., Larson 1985; Li et al. 2003). In cases of weak FUV intensities with $J_{21} \leq 10^4$ (see Figure 2.3), the temperature rapidly decreases via $\rm H_2$ cooling, which results in a soft equation of state $\gamma_{\rm eff} < 1$, where $P \propto \rho^{\gamma_{\rm eff}}$. Then, non-spherical perturbations grows to form filamentary clouds and efficient fragmentation occurs at $n \simeq 10^4~{\rm cm^{-3}}$, where $\rm H_2$ molecules reach the LTE and its cooling saturates ($\gamma_{\rm eff} \gtrsim 1$). The mass of fragments is typically determined by the Jeans mass at the temperature loitering point ($n \sim 10^4~{\rm cm^{-3}}$ and $T \sim 500$ K)

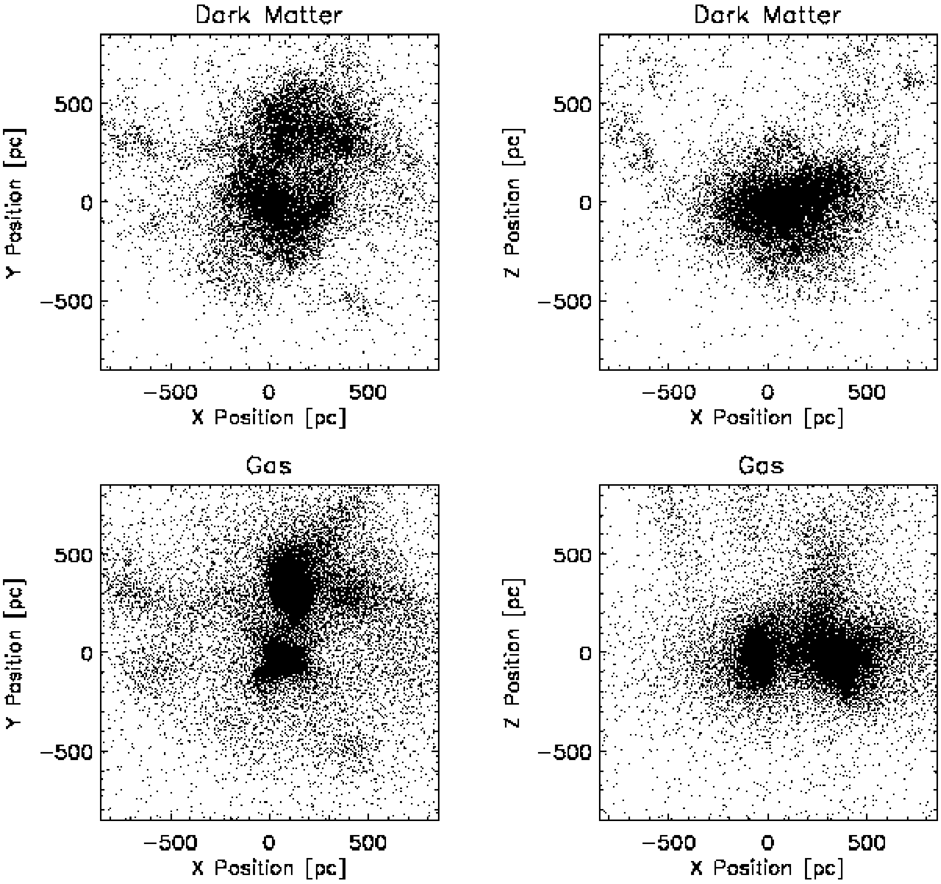

Figure 2.5: Density distribution of DM particles and gas in the atomic cooling halo irradiated with strong FUV radiations ($J_{21} = 10^5$). This figure is taken from Bromm & Loeb (2003)

and estimated as $M_{\rm cloud} \sim 10^3\ M_\odot$. On the other hand, the gas irradiated with strong FUV radiations ($J_{21} > 10^5$) continues to collapses isothermally ($\gamma_{\rm eff} \simeq 1$) instead of the rapid cooling. In such a case, the gas is expected to collapses runaway approaching a self-similar density profile (Penston 1969; Larson 1969) without efficient fragmentation. However, the self-similar solution could be unstable against the bar-mode perturbations (Hanawa and Matsumoto 2000; Lai 2000), which could prompt the gas fragmentation. In this way, the efficiency of fragmentation is non-trivial because of a lot physical processes and thus three-dimensional hydrodynamical simulations are needed to study this topic.

Figure 2.5 presents the results of the three-dimensional numerical simulation of the evolution of the gas where H_2 formation is suppressed by strong FUV. The four panels indicate the spatial distributions of the DM particles (top) and gas (bottom) at $z = 10.3$ with initial density fluctuations and no rotation. The gas falls into the deep gravitational potential of the DMs and become the virial state without efficient

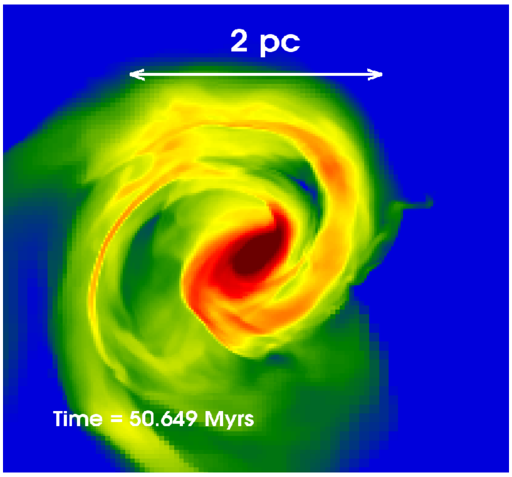

Figure 2.6: Density distribution of a collapsing supermassive cloud within ~ 2 pc from the center. These figure present the result of Regan and Haehnelt (2009a)

fragmentation, which results in formation of a supermassive cloud with $M \sim 2.7 \times 10^6\ M_\odot$. Bromm and Loeb (2003) also performed the simulation of cases that DMs and gas have the angular momentum due to the tidal force during structure formation. The strength of the rotation is often characterized by the (non-dimensional) spin parameter defined by

$$\lambda = \frac{J|E_{\mathrm{tot}}|^{1/2}}{GM^{5/2}}, \tag{2.18}$$

where J is the angular momentum and E_{tot} the total energy of the system. As a result of typical spin case $\lambda = 0.05$, which is given by most cosmological simulations, the gas fragments into two supermassive cloud, whose mass are larger than $\sim 10^6\ M_\odot$.

Similar simulations have been performed by Regan and Haehnelt (2009a,b) and Shang et al. (2010) using the adaptive mesh refinement (AMR) code. These results show that no efficient fragmentation and massive disk formation (see Figure 2.6), which are basically consistent with that of Bromm and Loeb (2003). Most recent work by Latif et al. (2013a,b) studied the collapse phase until $n \sim 10^{16}$ cm^{-3} ($\rho \sim 10^{-8}$ g cm^{-3}), where the protostellar formation is expected, and obtained the similar results as the previous ones. However, these results have significant problems. One is the oversimplification of the cooling processes in the collapsing gas. Most previous works considered only Lyα cooling which is assumed to be the optically thin limit. As you see in Figure 2.4, the dominant cooling process is the continuum emissions at high density regime ($n > 10^8$ cm^{-3}) because the Lyα emission becomes optically thick. Since the temperature dependence of the cooling rate of the continuum radiations is much stronger than that of the Lyα emission, thermal evolution is expected to change from the previous results. Second is turning off H_2 molecular cooling or elevating the photo-dissociating FUV background field by hand. In the gas, H_2 molecules are formed through the three-body reaction and its abundance rapidly increases at high density $> 10^{10}$ cm^{-3}, which could lead to efficient cooling and fragmentation. In chapter***, we again consider these problems in more detail.

2.3 Possibility to form supermassive stars

In the previous section, we introduced the formation scenario of seed BHs in the early universe through the direct collapse of supermassive stars, which are formed from primordial gas irradiated with strong FUV radiations. In this section, we discussed whether supermassive stars are actually formed in the early universe $z \gtrsim 10$. Main topics reviewed in this section are the following two: (1) rarity of the atomic cooling halos irradiated with FUV flux stronger than $J_{\rm crit}$ and (2) effects of the metal pollution on the gas thermal evolution. In addition to these, we also discussed the negative effect of cosmic ray / X-ray ionization on the SMS formation in chapter 3.

2.3.1 Rarity of halos irradiated with $J_{21} > J_{\rm crit}$

We first consider how many atomic cooling halos are exposed to strong FUV radiation ($J_{21} > J_{\rm crit} \sim 10^3 - 10^5$) in the early universe at $z \gtrsim 10$. As seen in section 2.2.1, the FUV radiation background at $z \gtrsim 10$ is estimated $J_{21} \sim 0.1 - 1$, which is much smaller than the critical intensity required to suppress the H_2 cooling completely. Then, the promising sites to form SMSs are very rare atomic cooling halos exposed to the FUV radiations from close luminous star-forming galaxies within $\lesssim 10$ kpc (Dijkstra et al. 2008). Dijkstra et al. (2008) estimated the rarity of the atomic cooling halos at $z = 10$ irradiated with the FUV flux stronger than $J_{\rm crit,21}(> 10^3)$ using the Press-Schechter theory and Monte Carlo calculations, and concluded the fraction of such objects as a non-negligible value $\lesssim 10^{-6}$. However, the probability exponentially decreases for $J_{21} \gtrsim 10^3$, which leads to the difficulties to realize the FUV radiations enough to form SMSs if $J_{\rm crit,21} \gg 10^3$.

Recently, this topic has been studied in more detail using numerical simulations for the cosmological structure formation (Agarwal et al. 2012; Johnson et al. 2013). They predicted the evolution of the stellar populations from Pop III to Pop II stars and the build up of the FUV radiations from the two populations considering the effect of the IGM metal-enrichment on the population transition. Figure 2.7 presents the distribution function of the FUV flux for the pristine halos at the two epoch ($z = 16.01$ and 8.45). The histograms present the FUV flux from Pop III stars (blue) and Pop II stars (red), respectively. The vertical dashed lines are the critical FUV intensities for cases with thermal spectrum of $T_* = 10^4$ (Pop II) and 10^5 K (Pop III). The FUV flux by Pop III stars is below the critical value ($J_{\rm crit,III} \simeq 10^3$) at all redshift, whereas

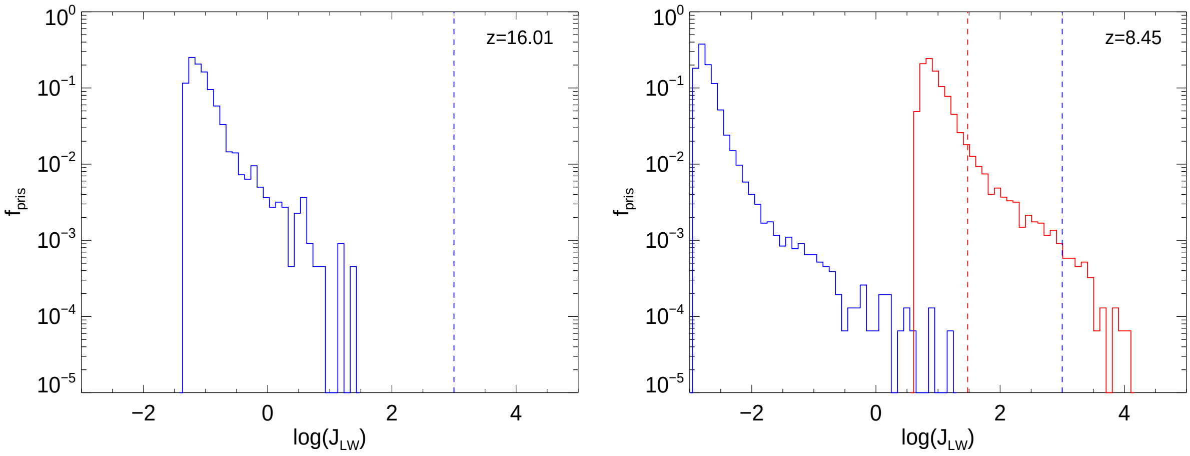

Figure 2.7: The distribution function of the FUV flux for the pristine halos at the two epoch ($z = 16.01$ and 8.45). The histograms present the FUV flux from Pop III stars (blue) and Pop II stars (red), respectively. The vertical dashed lines are the critical FUV intensities for cases with thermal spectrum of $T_* = 10^4$ (Pop II stars) and 10^5 K (Pop III stars). This figure is taken from Agarwal et al. (2012).

that by Pop II stars can locally exceed the critical value ($J_{\rm crit,II} \simeq 30$). Although these results could not be robust because of many uncertainties for the IGM metal-enrichment and Pop II star formation in the early universe, the FUV radiations from Pop II star-forming galaxies are expected to actually have a significant role to suppress the H_2 cooling and lead formation of supermassive stars. To clarify the quantitative understandings, more sophisticated studies are needed.

2.3.2 metal enrichment

After first stars are born in the early universe, the IGM metal enrichment proceeds in the same way as the build up of the LW radiation background. Metals are mainly produced by the stellar nuclear synthesis. Some fractions of metals condense into dust grains, which are ejected by the stellar winds at the asymptotic giant branch (AGB) phase and the SN explosions. Since the lifetime of low mass stars, which evolve to the AGB phase, is shorter than the age of the universe, the main pathway to produce dust grains could be the SN explosion in the early universe (Omukai et al. 2005). The transports of metals and dusts into the IGM have been studied by several authors. The two ways are considered to be promising processes; (1) outflows from the nearby star-forming regions and (2) inheriting from the parent sub-halos (Schneider et al. 2006b). Figure 2.8 shows the SFR of Pop II stars (solid) and Pop III stars (dashed), and the mass-averaged metallicity (dot-dashed) as a function of the redshift (Tornatore et al. 2007). The averaged IGM metallicity increases as the star formation

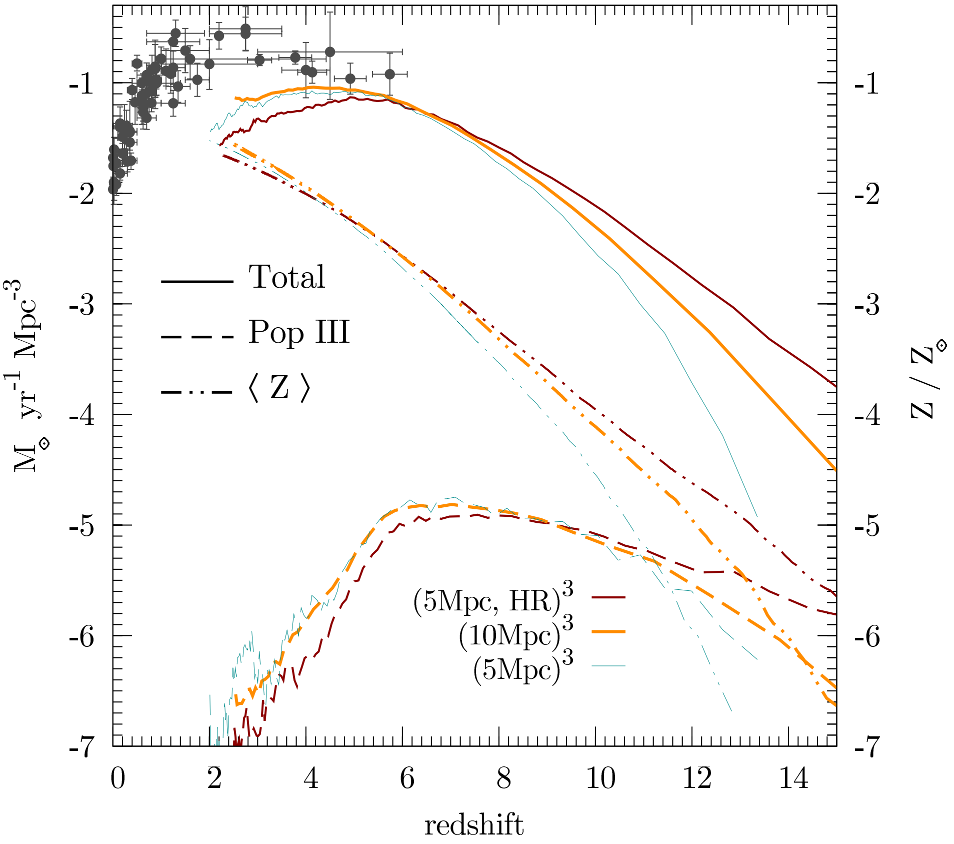

Figure 2.8: Predicted star formation rate of Pop II stars (solid) and Pop III stars (dashed), and the mass-averaged metallicity (dot-dashed) as a function of the redshift. The colors of the lines show the differences of the resolutions of their numerical simulations. This figure is taken from Tornatore et al. (2007).

is activated. The metal enrichment at $z = 10$ reaches $Z \lesssim 10^{-4}\ Z_\odot$. Although the averaged metallicity increases, the pristine regions (i.e., not polluted) continue to survive until low redshift universe ($z < 5$) because of the non-homogeneous metal enrichment. As a result, the Pop III star formation continues down to $z \simeq 2.5$, but at a low SFR $\gtrsim 10^{-5}\ M_\odot\ \mathrm{yr}^{-1}\ \mathrm{Mpc}^{-3}$.

As the IGM is polluted by metals and dusts, the Pop III/II transition from massive stars to low mass stars is expected to occur. According to studies about thermal evolution of low-metallicity gas (e.g., Omukai 2000; Omukai et al. 2005; Schneider et al. 2006a; Tsuribe and Omukai 2006; Clark et al. 2008; Omukai et al. 2010; Dopcke et al. 2013) the thermal emissions by dusts drives the fragmentation and formation of low mass objects when the gas metallicity is higher than $Z_{\rm cr} \simeq 10^{-5\pm1}\ Z_\odot$. The critical metallicity driving the Pop III/II transition has been actively discussed since the properties of dusts in the low-metallicity environments have some uncertainties.

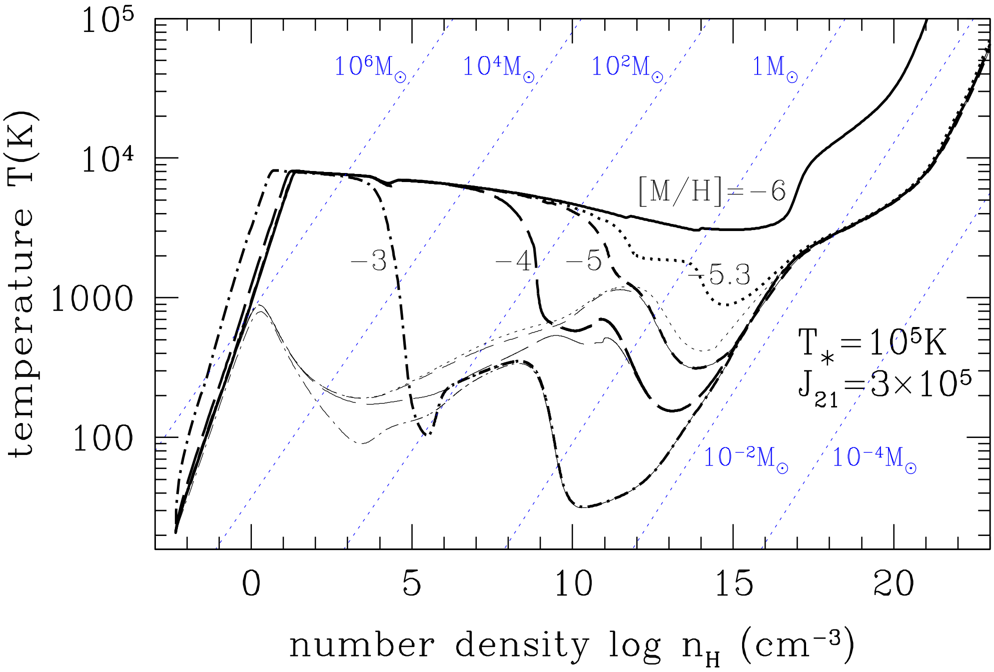

Figure 2.9: Thermal evolution of the low-metallicity gas irradiated with strong FUV flux ($J_{21} = 3 \times 10^5$) assuming the blackbody spectrum with $T_{\rm eff} = 10^5$ K (thick line). Each line presents the case of $\log Z = -6$ (solid), -5.3 (dotted), -5 (short-dashed), -4 (long-dashed), -3 (dot-dashed), respectively. Thin lines shows the results without an external FUV radiations. This figure is taken from Omukai et al. (2008).

From the recent observation of metal-poor stars by SDSS, an extremely metal-poor star with $Z \simeq 10^{-4.5}\ Z_\odot$ was found (Caffau et al. 2011).

As the Pop III/II transition, the effects of the metal cooling on the thermal evolution of the gas irradiated with strong FUV radiations was investigated by (Omukai et al. 2008). As seen from Figure 2.9, the thermal evolution of the gas for $Z > 10^{-5.3}\ Z_\odot$ change from the primordial case because of the dust cooling. In such cases, the gas temperature decreases at higher density $\sim 10^{10} - 10^{15}$ cm^{-3}, which could result in efficient fragmentation. Efficient fragmentation due to the dust cooling would suppress the formation of supermassive stars. However, the typical distance between fragments at the high density regime is so small that the fragments rapidly merge and form supermassive stars. To understand whether the dust cooling affects on the supermassive star formation or not, three-dimensional hydrodynamical simulations are awaited and will be my future works.

2.4 Protostellar evolution

When the atomic gas monolithically collapses, a low mass protostar ($\sim 0.01\ M_\odot$) forms at the center of the cloud. The embryo protostar subsequently grows to an SMS via rapid gas accretion of the surrounding envelope. The accretion rate onto a protostar is roughly set by the temperature in the star-forming cloud as

$$\begin{aligned} \dot{M}_{\rm acc} &\simeq \frac{M_{\rm J}}{t_{\rm ff}} \simeq \frac{c_{\rm s}^3}{G} \\ &\simeq 0.1\ M_\odot\ {\rm yr}^{-1} \left(\frac{\mu}{1.2}\right)^{-3/2} \left(\frac{T_{\rm cloud}}{8000\ {\rm K}}\right)^{3/2}, \end{aligned} \tag{2.19}$$

(Shu 1977; Stahler et al. 1986). Since the accretion rate depends on the cloud temperature, the protostellar evolution is also determined by the thermal history of the parent cloud. Thus, there is an important difference; in the H atomic cooling case, the accretion rate on to the protostar is $\sim 0.1\ M_\odot\ {\rm yr}^{-1}$ ($T_{\rm cloud} \sim 8000$ K), which is much higher than that in the ordinary Pop III case, where the H_2 cooling is effective ($\sim 10^{-3}\ M_\odot\ {\rm yr}^{-1}$; $T_{\rm cloud} \sim 400$ K).

Figure 2.10 shows the evolution of the radii of accreting protostars at different accretion rates as a function of the stellar mass. For the low accretion rate case ($\dot{M}_{\rm acc} = 10^{-3}\ M_\odot\ {\rm yr}^{-1}$), the stellar radius gradually expands with mass via the adiabatic heat input, so called the adiabatic-accretion phase. After that, protostar starts to contract by losing its entropy via radiative diffusion (the Kelvin-Helmholtz contraction) until the nuclear ignition occurs at the center. On the other hand, with the accretion rate as high as $\dot{M}_{\rm acc} \sim 0.1\ M_\odot\ {\rm yr}^{-1}$, the protostar continues expanding without the Kelvin-Helmholtz contraction. In such a star, while most of the interior material contracts, the outermost layer significantly swells up like a red giant star (‘supergiant protostar’ phase). This is because the outer layer absorbs a part of the outward heat flux and obtains a very high specific entropy. Also in this case, the contraction at the centre ceases with the hydrogen ignition, but the envelope continuously expands with the increase of stellar mass.

In this evolutionary stage, the stellar luminosity is close to the Eddington value ($L_* \simeq L_{\rm Edd} \propto M_*$), and the effective temperature remains almost constant at $T_{\rm eff} \simeq 5000$ K due to the strong temperature dependence of the H^- bound-free opacity. With these two conditions and diffusion equation,

$$L_* = 4\pi R_*^2 \sigma_{\rm SB} T_{\rm eff}^4, \tag{2.20}$$

where $\sigma_{\rm SB}$ is the Stefan-Boltzmann constant, the mass-radius relation of the supergiant protostars is analytically written as

$$R_* \simeq 8.2 \times 10^3\ R_\odot \left(\frac{M_*}{10^3\ M_\odot}\right)^{1/2}, \tag{2.21}$$

which well agrees with the numerical results in Figure 2.10.

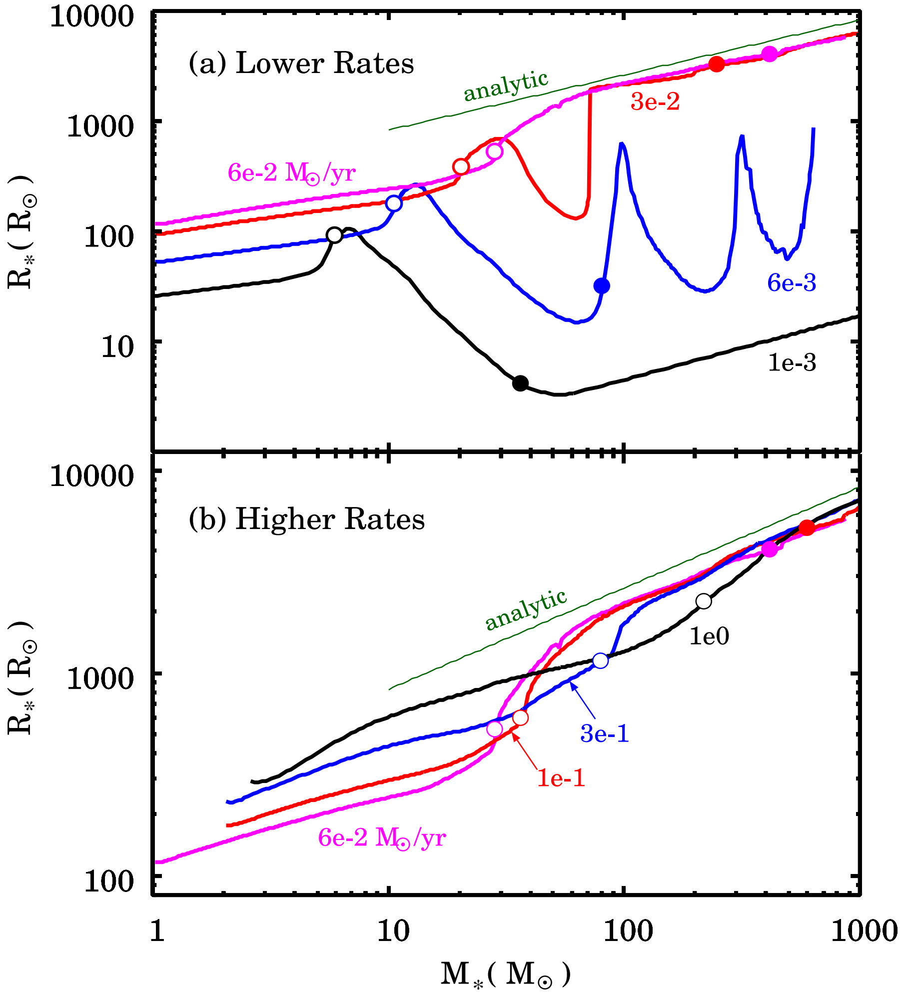

Figure 2.10: Evolution of the protostellar radius with various accretion rates ($10^{-3} \leq \dot{M}_{\rm acc} \leq 1.0\ M_{\odot}\ {\rm yr}^{-1}$). This figure is taken from Hosokawa et al. (2012a).

As a protostar grows to massive more than $10^2\ M_{\odot}$, the stellar luminosity approaches the Eddington luminosity. For cases with $\dot{M}_{\rm acc} < 10^{-2}\ M_{\odot}\ {\rm yr}^{-1}$, after the KH contraction, the surface temperature increase to $\sim 10^5$ K and thus the large amounts of ionizing photons are emitted. Such strong ionizing radiations heats up the surrounding materials and halts the accretion onto the protostar (McKee and Tan 2008; Hosokawa et al. 2011; Stacy et al. 2012). On the other hand, for the case of SMS formation ($\dot{M}_{\rm acc} > 10^{-2}\ M_{\odot}\ {\rm yr}^{-1}$), supergiant protostars have the bloated and cool ($T_{\rm eff} \simeq 5000$ K) envelope throughout the stellar evolution. In this case, since they hardly emit ionizing photons and create an large $\rm H_{II}$ region, the radiative negative feedback does not work, which could result in the continuous gas supply into the central protostar even without other negative feedbacks (e.g., stellar pulsation). In chapter 6 and 7, we describe our studies about the pulsational instability of supergiant protostars and the subsequent evolution up to $M_* \gtrsim 10^5~M_\odot$.

Chapter 3

Effect of cosmic ray/X-ray ionization on SMBH formation

As we describe in section 2.2.4, supermassive stars are expected to form form primordial gas where H_2 cooling is suppressed by the FUV radiations. The critical FUV flux, $J_{\rm crit}$, for the suppression of the H_2 cooling is far above the predicted mean value of the background radiation. The value of $J_{\rm crit}$ strongly depends on the spectrum of the FUV sources. Assuming a diluted thermal spectrum, $J(\nu) \propto B_\nu(T_*)$, $J_{\rm crit} \simeq 10^2$ for $T_* = 10^4$ K and $\simeq 10^5$ for $T_* = 10^5$ K (in units of 10^{-21} erg s^{-1} cm^{-2} sr^{-1} Hz^{-1}), corresponding to that from star-forming galaxies including Pop II and III stars, respectively. Dijkstra et al. (2008) estimated the probability distribution of the FUV intensity incident on halos with mass $\sim 10^8\ M_\odot$ collapsing at redshift $z \simeq 10$ and showed such intense FUV fields are only realized in neighborhoods of strong FUV sources. They also estimated the fraction of halos bathed in radiation fields exceeding the threshold value $J_{\rm crit}$. This fraction is 10^{-6} for $J_{\rm crit} = 10^3$ and decreases exponentially with increasing $J_{\rm crit}$ ($> 2 \times 10^3$). A small difference in $J_{\rm crit}$ significantly affects the number of halos bearing supermassive stars, and thus correct knowledge of the critical FUV flux is crucial in estimating the number of seed BHs.

So far, the critical FUV flux $J_{\rm crit}$ has been studied only in cases where the incident radiation consists of components below the Lyman limit (Omukai 2001; Bromm and Loeb 2003; Shang et al. 2010). However, strong FUV sources, i.e., actively star-forming galaxies, are expected to contain a large number of massive stars and possibly some mini-quasars. Since massive stars end their lives as supernovae and leave the remnants, where cosmic rays (CRs) are accelerated and X-ray photons are produced, sources of strong FUV radiation can also be those of CRs and X-ray photons. Similarly, mini-quasars and high-mass X-ray binaries emit soft X-ray radiation. The incident flux is thus expected to have such high-energy components. If present, CRs and X-rays enhance the ionization degree of gas and increase the amount of H_2, which is formed by electron-catalysed reactions. In fact, Haiman et al. (1996) and Glover and Brand (2003), who studied the condition for virialized minihalos under both FUV and X-ray irradiation to be able to cool via H_2 line emission, found that the FUV photodissociation effect is somewhat alleviated by the X-ray ionization.

In this chapter, we discuss the thermal evolution of primordial gas, including chemical reactions and effects of FUV and CRs/X-rays. We also present the dependence of $J_{\rm crit}$ on the ionization rate by CRs/X-rays (section 3.2) and give an analytic interpretation for this (section 3.3). In section 3.4, we use an empirical relation between intensities of FUV and CRs/X-rays from nearby star-forming galaxies and speculate on conditions required to induce supermassive star formation. Finally, we summarize this section and provide some discussion in section 3.5.

3.1 Setups of our models

We consider thermal evolution of a metal-free cloud in a moderately massive halo with virial temperature $\gtrsim 10^4$ K irradiated by a FUV field and simultaneously by either CRs or X-rays. In this section, we briefly explain how to treat the evolution of cloud collapse (thermal state and chemistry) and the effects of external radiations (FUV, CR, and X-ray).

3.1.1 thermal evolution

The evolution during the gravitational collapse is calculated by a one-zone model. The actual hydrodynamical collapse of self-gravitating clouds is well described by the Penston-Larson self-similar solution (Penston 1969; Larson 1969). In this solution, the clouds consist of two spatial parts: the flat central core, whose size is about the Jeans length $\lambda_{\rm J}$ and where number density of hydrogen nuclei $n_{\rm H}$ and temperature T, etc. are nearly homogeneous, and the envelope, where the density profile obeys the power law with radius as $\rho \propto r^{-2}$. In our one-zone model, all the physical variables such as $n_{\rm H}$, T, etc. are thus intended to indicate those at the center of the core. The central density increases approximately at the free-fall rate as

$$\frac{d\rho}{dt} = \frac{\rho}{t_{\rm ff}}, \tag{3.1}$$

where $t_{\rm ff} = \sqrt{3\pi/32G\rho}$. In evaluating $t_{\rm ff}$, we neglect the contribution from the dark matter because the dark-matter gravity dominates only just before the virialization, where the temperature increases adiabatically in any case.

The temperature evolution is calculated by solving the energy equation:

$$\frac{de}{dt} = -p\frac{d}{dt}\left(\frac{1}{\rho}\right) - \frac{\Lambda_{\rm net}}{\rho}, \tag{3.2}$$

where e is the internal energy per unit mass, p the gas pressure, $\mu(=1.2)$ the mean molecular weight, $k_{\rm B}$ the Boltzmann constant, $\gamma_{\rm ad}(=5/3)$ the ratio of specific heat, and $\Lambda_{\rm net}$ the net cooling rate per unit volume. We here consider the cooling processes for $10 < T < 10^4$ K in primordial gas by H atom, H_2 molecule, and HD molecule (Omukai 2001; Galli and Palla 1998), net cooling associated with chemical reactions, and heating rates by CRs and X-rays, respectively. Chemical reactions in primordial gas among the following 14 species (H, H_2, e^-, H^+, H_2^+, H^-, D, HD, D^+, HD^+, D^-, He, He^+, and He^{++}) are considered. The included reactions are summarized in Table 1 of Inayoshi and Omukai (2011). We here adopt the H_2 collisional dissociation rate of Martin et al. (1996), which is ten times larger than the older rate of Shapiro and Kang (1987) used by Omukai (2001) around $\simeq 10^3\ {\rm cm^{-3}}$. The chemical reaction networks are solved by an implicit method.

When the collapse proceeds significantly and the cloud becomes optically thick, the radiative cooling becomes ineffective due to photon trapping. We assume the radius of the core to be half a Jeans length

$$R_{\rm c} = \frac{\lambda_{\rm J}}{2} = \sqrt{\frac{\pi k_{\rm B} T}{G \rho \mu m_{\rm H}}}. \tag{3.3}$$

Since we consider the core of the collapsing cloud, the column density of i-th species is given by $N_{\rm i} = x_{\rm i} n_{\rm H} R_{\rm c}$, where $x_{\rm i}$ is its concentration. Using this value, we estimate the optical depth and the reduction rate of radiative cooling as in Omukai (2001).

3.1.2 FUV radiation

The incident FUV radiation field is assumed to have a diluted thermal spectrum, i.e., $J(\nu) \propto B_\nu(T_*)$, with brightness temperature $T_* = 10^4$ or 10^5 K, as the previous works considered (see Section 2.2.3 and 2.2.4). We here consider the photo-dissociation of H_2, H^-, and HD by FUV radiations. We note that the dissociation rate of H^- strongly depends on T_*, whose rate is 2×10^4 times higher for $T_* = 10^4$ K than that for $T_* = 10^5$ K. The H_2 and HD are self-shielded against photodissociation for their column densities $N_{\rm H_2} > 10^{13}\ {\rm cm^{-2}}$. The HD shielding is also contributed by H and H_2. We use the shielding factors given by Wolcott-Green and Haiman (2011). For the photoionization of H and the photodissociation of H_2^+, those from the excited levels are also included as in Omukai (2001).

3.1.3 Cosmic Rays

For the incident CR flux, we follow the treatment by Stacy and Bromm (2007). The CR energy distribution $dn_{\rm CR}/d\epsilon$ (${\rm cm^{-3}\ eV^{-1}}$) is assumed to obey a power-law spectrum with index -2, the value by the diffusive shock acceleration by a strong shock (e.g., Bell 1978) from the minimum energy $\epsilon_{\rm min} = 10^6$ eV to the maximum $\epsilon_{\rm max} = 10^{15}$ eV. After incident to the gas, CRs propagate inward with losing their energies by ionization up to the penetration depth $D_{\rm p}$ at a rate $(d\epsilon/dt)_{\rm ion}$, for which we use the expression by Schlickeiser (2002). The heating rate by CRs at depth D is

$$\Gamma_{\rm CR}(D) = \frac{E_{\rm heat}}{\Delta\epsilon}\int_{\epsilon_{\rm min}}^{\epsilon_{\rm max}} \left(\frac{d\epsilon}{dt}\right)_{\rm ion} \frac{dn_{\rm CR}}{d\epsilon} e^{-D/D_p} d\epsilon, \tag{3.4}$$

where $\Delta\epsilon = 50$ eV is the approximate kinetic energy of a CR particle lost upon each scattering (Spitzer and Tomasko 1968), and the ionization rate is

$$\zeta_{\rm CR}(D) = \frac{\Gamma_{\rm CR}(D)}{n_{\rm H} E_{\rm heat}}, \tag{3.5}$$

where $E_{\rm heat} \simeq 6$ eV is the energy deposited as heat per ionization in a neutral medium (Spitzer and Scott 1969; Shull and van Steenberg 1985). Note that the CR ionization rate is related with the total CR energy density,

$$U_{\rm CR} = \int_{\epsilon_{\rm min}}^{\epsilon_{\rm max}} \epsilon \frac{dn_{\rm CR}}{d\epsilon} d\epsilon, \tag{3.6}$$

by

$$\zeta_{\rm CR} = 1.7 \times 10^{-18} U_{15}\ {\rm s^{-1}}, \tag{3.7}$$

in the low column density limit, where $U_{15} = U_{\rm CR}/10^{-15}$ erg cm^{-3} whereas the CR ionization rate $\zeta_{\rm CR}$ for high column density $N_{\rm H}$ can be approximated as

$$\begin{aligned} \zeta_{\rm CR} &= 1.3 \times 10^{-19} U_{15} \left(\frac{N_{\rm H}}{10^{22}\ {\rm cm^{-2}}}\right)^{-3/4} {\rm s^{-1}}, \\ &= 6.8 \times 10^{-20} U_{15} \left(\frac{n_{\rm H}}{10^{3}\ {\rm cm^{-3}}} \cdot \frac{T}{8000\ {\rm K}}\right)^{-3/8} {\rm s^{-1}}, \end{aligned} \tag{3.8}$$

for column density higher than $> 10^{22}$ cm^{-2}.

The CR ionization rate in the Milky Way has been estimated by many authors, including $\zeta_{\rm CR} \simeq 4 \times 10^{-16}$ s^{-1} (Hayakawa et al. 1961), $6.8 \times 10^{-18}\ {\rm s^{-1}} < \zeta_{\rm CR} < 1.2 \times 10^{-15}\ {\rm s^{-1}}$ (Spitzer and Tomasko 1968) and $\zeta_{\rm CR} \simeq 3 \times 10^{-17}$ s^{-1} (Webber 1998). By recent observation of H_3^+ in the interstellar medium, the average H_2 ionization by CRs is evaluated $\zeta_{\rm CR,H_2} \simeq 4 \times 10^{-16}$ s^{-1} (McCall et al. 2003; Indriolo et al. 2007), which is translated to a rather high H ionization rate of $\zeta_{\rm CR} \simeq 2.6 \times 10^{-16}$ s^{-1}. The CR intensity at high redshift is totally uncertain. The CR energy density is set by a balance between the injection and the diffusive leakage. On one hand, star formation in young galaxies can be more active than in the Milky Way. The CR injection rate being proportional to the star formation rate, the gas in the neighborhood of such galaxies is subject to intense CRs. On the other hand, magnetic fields are expected to be much weaker in young galaxies, which results in the longer Larmor radii of CRs and easier leakage from the galaxies. This may result in weaker CR density if the CR sources are in the same halo. Considering those uncertainties, we here regard the CR energy density as a free parameter and calculate the cases for $10^{-3} \le U_{15} \le 10^{4}$, which corresponds to the CR ionization rate of $10^{-21}\ {\rm s^{-1}} < \zeta_{\rm CR} < 10^{-14}\ {\rm s^{-1}}$ in the low density case.

3.1.4 X-rays

Since the ionization cross sections of hydrogen and helium fall as $\sigma_{\mathrm{H}}(\nu) \propto \nu^{-3}$ and $\sigma_{\mathrm{He}}(\nu) \propto \nu^{-2}$, respectively, towards higher energy photons, the soft X-ray ($2-10$ keV) photons reach far longer distance from the sources than ionizing UV photons. Many sources contribute to X-rays at a given point, i.e., an extragalactic X-ray background is built up (Haiman et al. 1997).

Following Glover and Brand (2003), we assume the incident X-ray background having a power-law spectrum with index -1.5,

$$J_{\mathrm{X}}(\nu) = J_{\mathrm{X},21} \times 10^{-21} \left(\frac{\nu}{\nu_0}\right)^{-1.5} \ \mathrm{erg\,s^{-1}\,cm^{-2}\,sr^{-1}\,Hz^{-1}}, \tag{3.9}$$

where $h\nu_0 = 1$ keV. We consider the X-ray ionization of both H and He atoms. The heating rate by X-rays is

$$\Gamma_{\mathrm{X}} = \Gamma_{\mathrm{X,H}} + \Gamma_{\mathrm{X,He}}, \tag{3.10}$$

where

$$\Gamma_{\mathrm{X},i} = \int \frac{4\pi J_{\mathrm{X}}(\nu)}{h\nu} e^{-\tau_\nu} \sigma_i(\nu) E_{\mathrm{h},i} d\nu \quad (i = \mathrm{H},\ \mathrm{He}), \tag{3.11}$$

the optical depth is given by

$$\tau_\nu = N_{\mathrm{H}}\sigma_{\mathrm{H}}(\nu) + N_{\mathrm{He}}\sigma_{\mathrm{He}}(\nu), \tag{3.12}$$

$E_{\mathrm{h},i}$ is the energy deposited as heat for each ionization process, and given by a formula by Wolfire et al. (1995). The ionization rate is also expressed as

$$\zeta^i_{\mathrm{X,p}} = \int \frac{4\pi J_{\mathrm{X}}(\nu)}{h\nu} e^{-\tau_\nu} \sigma_i(\nu) d\nu, \tag{3.13}$$

where the subscript p represents primary ionization by X-rays. The primary electron's energy is deposited not only in heating but also in the secondary ionization. Since the energy of the primary electron is far larger than the ionization threshold, the secondary ionization is more effective than the primary in the case of X-ray ionization. The secondary ionization rate of H is given by

$$\zeta^{\mathrm{H}}_{\mathrm{X,s}} = \left(\zeta^{\mathrm{H}}_{\mathrm{X,p}} + \frac{y(\mathrm{He})}{y(\mathrm{H})}\zeta^{\mathrm{He}}_{\mathrm{X,p}}\right)\langle\phi^{\mathrm{H}}\rangle, \tag{3.14}$$

and the secondary ionization rate of He is expressed similarly, where $\langle\phi^{\mathrm{H}}\rangle$ is the number of secondary ionization per primary electron averaged over the X-ray spectrum, for which we use the expression by Wolfire et al. (1995). Then, the terms on the right hand side mean the secondary ionization rate by primary electrons due to H and He ionization, respectively. The total ionization rate by X-rays is given by the sum of the primary and secondary rates:

$$\zeta^i_{\mathrm{X}} = \zeta^i_{\mathrm{X,p}} + \zeta^i_{\mathrm{X,s}} \quad (i = \mathrm{H},\ \mathrm{He}). \tag{3.15}$$

In considering the secondary ionization, the H and He ionization rates are about the same magnitudes, $\zeta^{\mathrm{H}}_{\mathrm{X}} \simeq \zeta^{\mathrm{He}}_{\mathrm{X}}$.

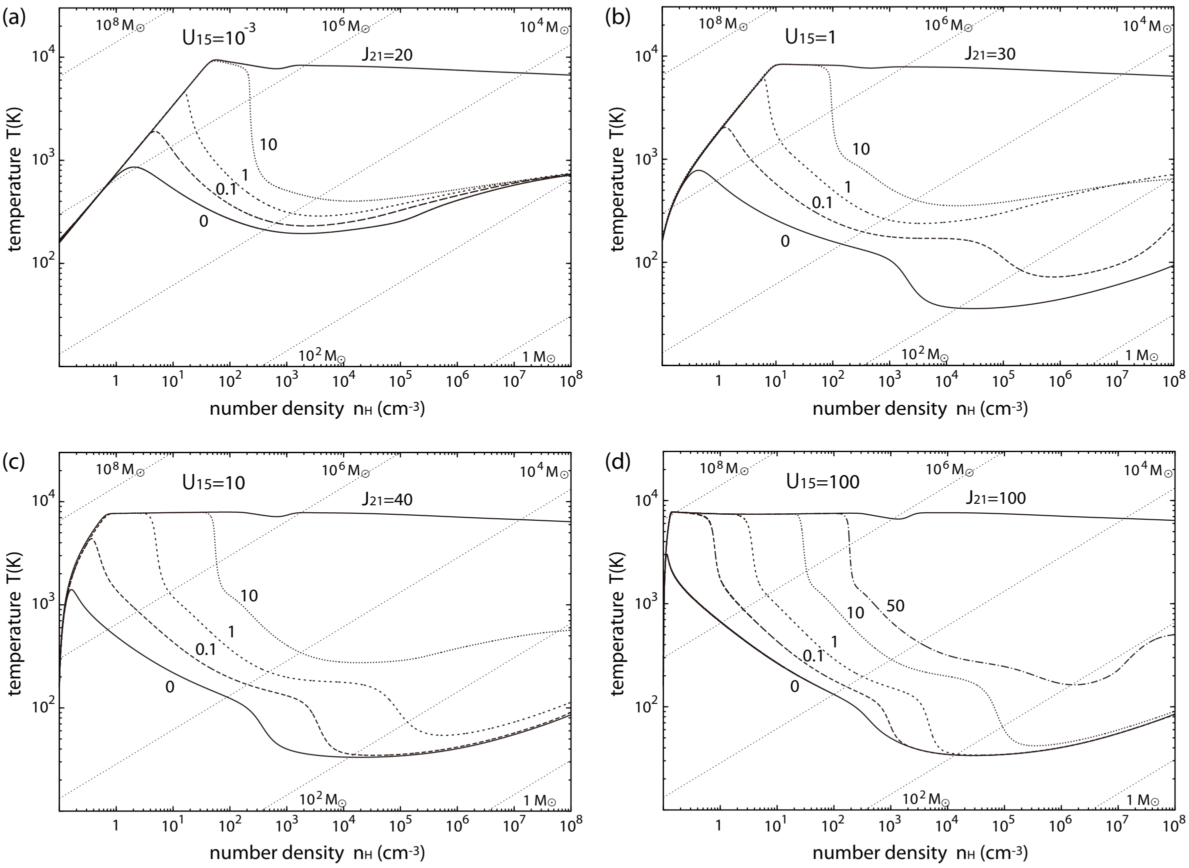

Figure 3.1: Effect of cosmic rays on the temperature evolution of primordial-gas clouds under FUV irradiation with $T_* = 10^4$ K. Four panels correspond to the evolutionary tracks with four different cosmic-ray energy densities: $U_{15} = 10^{-3}$, 1, 10 and 100, where $U_{15} = U_{\rm CR}/10^{-15}$ erg cm^{-3}. The curves in each panel are those for different FUV fluxes, whose intensities J_{21} are indicated by numbers. The diagonal dotted lines show those at the constant Jeans mass, whose values are indicated by numbers in the Figure. These figures are taken from Inayoshi and Omukai (2011).

3.2 Results

We here present the results of our calculation and describe the physical processes determining the thermal evolution of the clouds.

3.2.1 Effects of cosmic rays

In Figure 3.1, we show the temperature evolution of collapsing clouds irradiated by FUV fields with a diluted blackbody spectrum $T_* = 10^4$ K, along with CRs with energy density (a) $U_{15} = 10^{-3}$, (b) 1, (c) 10, and (d) 100. The lines in each panel are for cases with different values of FUV strength J_{21}, which are indicated by numbers in the panel. For the cases with $U_{15} = 10^{-3}$ (left) and 100 (right), we also plot in

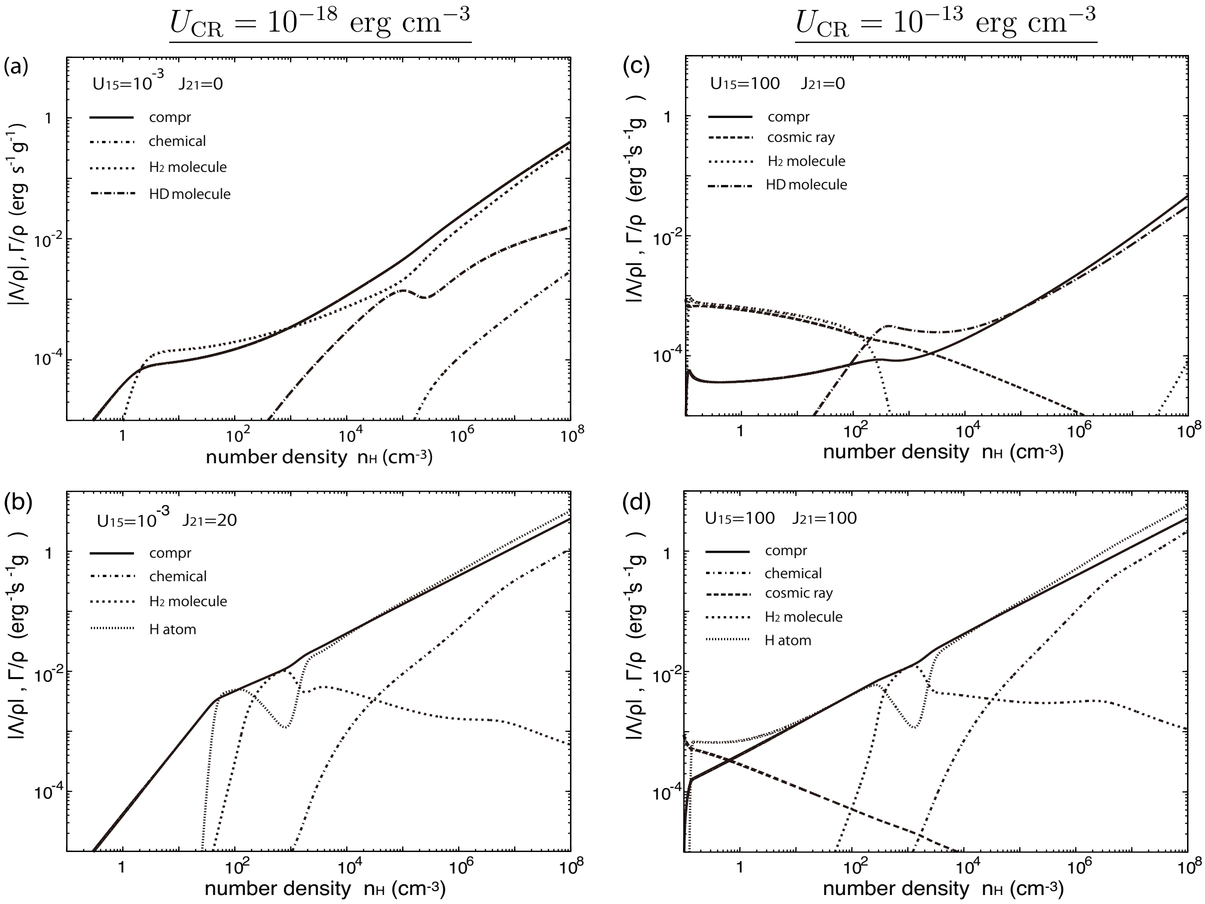

Figure 3.2: Cooling and heating rates per unit mass as a function of the central number density. The cosmic ray energy density is $U_{15} = 10^{-3}$ (left) and 10^2 (right), and the FUV intensity is $J_{21} = 0$ and $J_{21} \geq J_{\rm crit}$ for each case, respectively. The lines show the heating rates by compression (thick) and chemical reactions (short dash-dotted), and cooling rates by H_2 (thick dotted) and HD (dash-dotted) molecules, H atoms (dotted). These figures are taken from Inayoshi and Omukai (2011).

Figure 3.2, the cooling and heating rates per unit mass by individual processes, i.e., heating rates by compression (thick), by CR (dashed) and by chemical reactions (short dash-dotted), and cooling rates by the H_2 (thick dotted), by HD (dash dotted) and by H atom (dotted).

In the case of $U_{15} = 10^{-3}$, where the CR is too weak to affect any aspect in the evolution (Figure 3.1 a, 3.2 a, and 3.2 b), the results are similar to those described in Section 2.2.2 (no-CR cases). We here show these results for comparison with strong CR cases. In the no-FUV case ($J_{21} = 0$), the gas collapses along the standard track (e.g., Palla et al. 1983), where the compressional heating and H_2 cooling are balanced (Figure 3.2 a). When a FUV field exceeds a critical value $J_{21} \geq J_{\rm crit} \simeq 20$, the temperature evolution proceeds keeping $\simeq 8000$ K until high density ($> 10^8$ cm^{-3}). Throughout the evolution, the H_2 cooling never becomes important (Figure 3.2 b).

Next, we see how the thermal evolution described above changes with increasing CR flux. The CR effects are twofold, i.e., heating and ionization. The stronger the CR flux is, the more rapid is the initial temperature-increase owing to the CR heating as seen in Figure 3.1 (b)−(d). In Figure 3.2 (d) for $U_{15} = 100$, very high CR-heating rate can be seen at the lowest density. Enhanced ionization degree facilitates the H_2 formation via H^- channel ($H + e^- \rightarrow H^- + \gamma$ and $H^- + H \rightarrow H_2 + e^-$). To quench H_2 cooling totally, higher FUV flux is necessary, namely, the value of the critical FUV flux $J_{\rm crit}$ becomes larger. For example, as seen in Figure 3.1 (d), under a very strong CR field of $U_{15} = 100$, even such strong FUV flux as $J_{21} = 50$ is not enough to quench the H_2 cooling. In Figure 3.3 (a), we plot the critical FUV flux $J_{\rm crit}$ as a function of the CR intensity. In the case of $T_* = 10^4$ K, from its low-CR limit of $J_{\rm crit} \simeq 20$, $J_{\rm crit}$ begins to increase around $U_{15} \sim 10$ and continues increasing as $J_{\rm crit} \propto {U_{15}}^{1/2}$ in the high U_{15} limit. The dominant cooling and heating processes are similar in all cases of the FUV flux exceeding the critical value $J_{\rm crit}$ (see Figures 3.2 b and d).

So far, we limit our analysis to the radiation spectra of $T_* = 10^4$ K. We also studied the case of $T_* = 10^5$ K. As mentioned previously, the H^- photodissociation rate depends sensitively on the brightness temperature T_*. Then, the concentration of H_2 produced through the H^- channel changes with the value of T_*. This leads to the enhancement of the critical FUV flux $J_{\rm crit}$ for $T_* = 10^5$ K compared to the case for $T_* = 10^4$. The critical flux $J_{\rm crit}$ for $T_* = 10^5$ K is also plotted in Figure 3.3 (a). We find that $J_{\rm crit} = 1.6 \times 10^4$ for $T_* = 10^5$ K, while $J_{\rm crit} = 20$ for $T_* = 10^4$ K in the no-CR cases. For CR energy density higher than $U_{15} \sim 10$, the critical FUV flux $J_{\rm crit}$ increases as $\propto {U_{15}}^{1/2}$ in both $T_* = 10^4$ and 10^5 K cases.

3.2.2 Effects of X-rays

Here, we briefly mention the cases of the clouds irradiated both by FUV and X-rays. The temperature evolution is shown in Figure 3.4 for (a) $J_{\rm X,21} = 10^{-6}$ and (b) 10^{-2}. For the X-ray intensity as low as $J_{\rm X,21} = 10^{-6}$, the effects of X-rays, either ionization or heating, are not important and the evolutionary tracks in Figure 3.4 (a) are the same as those with negligible CRs ($U_{15} = 10^{-3}$) in Figure 3.1 (a). When the X-ray intensity is elevated to $J_{\rm X,21} = 10^{-2}$, the gas is heated instantaneously (see Figure 3.4 b). In the case of $J_{21} = 0$, the H_2 cooling balances the X-ray heating at $\simeq 5000$ K and the temperature begins decreasing thereafter. For $J_{21} \geq 0.1$, the temperature reaches at $\simeq 8000$ K and remains almost constant for a while by the H atomic cooling until H_2 is self-shielded against the FUV field. Similar to the case of CR ionization, X-ray ionization enhances the critical FUV flux $J_{\rm crit}$ for quenching the H_2 cooling. This critical FUV flux $J_{\rm crit}$ is plotted in Figure 3.3 (b) as a function of the X-ray intensity $J_{\rm X,21}$. As in the case of CR ionization, $J_{\rm crit}$ remains constant below a threshold around $J_{\rm X,21} \sim 10^{-3}$ and increases as $(J_{\rm X,21})^{1/2}$ for higher X-ray intensity. Since the behaviors of

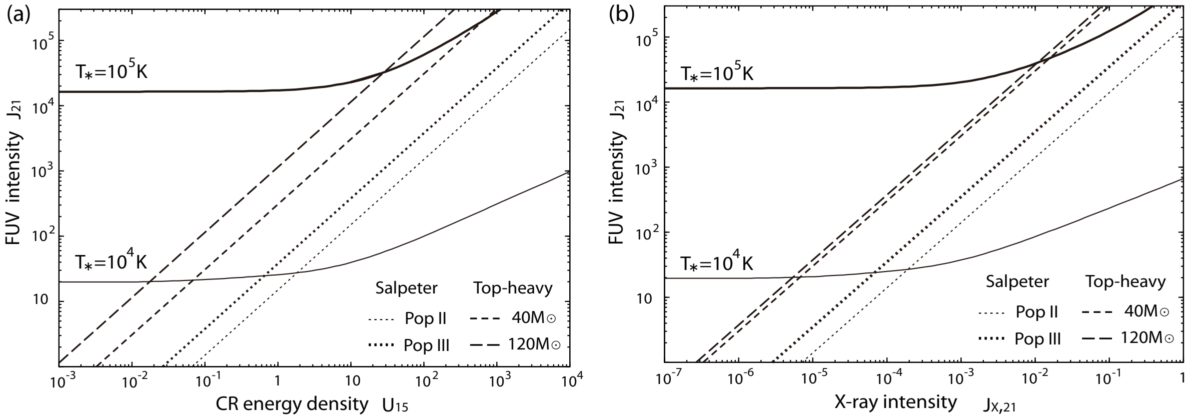

Figure 3.3: (a) The dependence of the critical FUV flux $J_{\rm crit}$ on the CR energy density U_{15} (solid curves) for two spectral types (thin curve: $T_* = 10^4$ K, thick curve: $T_* = 10^5$ K). In both cases, $J_{\rm crit} \propto {U_{15}}^{1/2}$ for $U_{15} > 10$. The lines indicate the relations between J_{21} and U_{15} emitted from a star-forming galaxy (equation 3.32) with (i) the Salpeter IMF and $Z = 10^{-3}\ Z_\odot$ (Pop II; thin dotted), (ii) Salpeter IMF and $Z = 0$ (Pop III; thick dotted), (iii) the top-heavy IMF with $m_{\rm OB} = 40\ {\rm M}_\odot$ (short dashed) and (iv) the top-heavy IMF with 120 $\rm M_\odot$ (long dashed), respectively. The intersection of the curves and lines for each T_* case corresponds to the actual CR energy density and critical FUV flux $J_{\rm crit}$ in a halo affected by the star-forming galaxy. (b) the same plot for the X-ray ionization. For both values of T_*, $J_{\rm crit} \propto (J_{\rm X,21})^{1/2}$ for $J_{\rm X,21} > 10^{-3}$. Note that the fraction of halos with $> 10^8\ {\rm M}_\odot$ at $z = 10$ irradiated by FUV radiation J_{21} exceeding $> 10^5$ is negligibly low $< 10^{-28}$. These figures are taken from Inayoshi and Omukai (2011).

temperature evolution for different FUV fluxes as well as the dominant cooling/heating processes are very similar to the cases with CRs, we do not repeat their description here.

3.3 Dependence of the critical FUV flux on CR/X-ray intensity

In Section 3, we see that strong CR and X-ray fluxes lead to the enhancement of the critical FUV flux as $J_{\rm crit} \propto {U_{15}}^{1/2}$ and $\propto (J_{\rm X,21})^{1/2}$, respectively (see Figure 3.3). Also, $J_{\rm crit}$ decreases with lowering FUV temperature T_*. In this section, we discuss the reason for these dependences. The chemical reactions needed in the below discussion are summarized in Table 3.3

In the cloud under a high enough FUV field, the temperature reaches $\simeq$ 8000 K

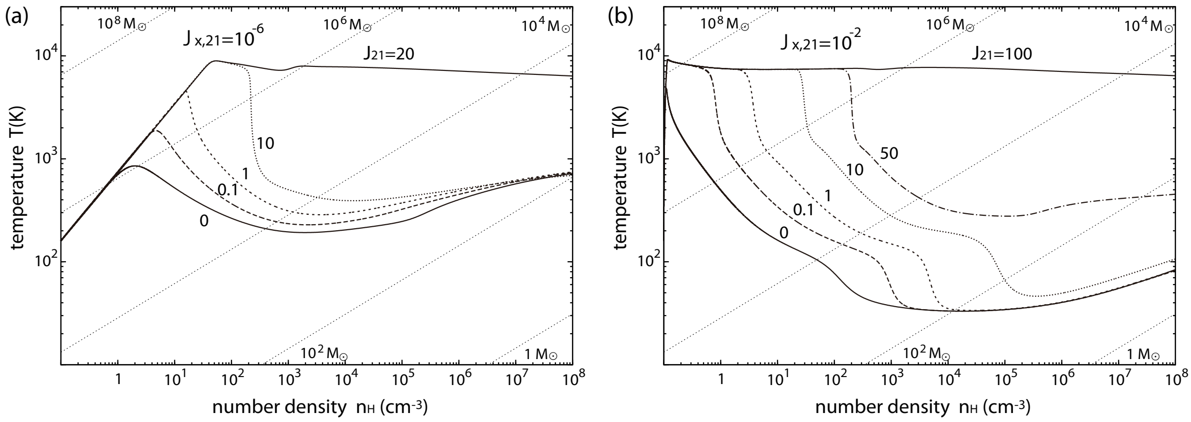

Figure 3.4: Effect of X-ray ionization on the temperature evolution of metal-free clouds under FUV irradiation with $T_* = 10^4$ K. Two panels show the evolutionary tracks with two different X-ray intensities $J_{\rm X,21} = 10^{-6}$ and 10^{-2}. The curves in each panel are those for different FUV fluxes, whose intensities J_{21} are indicated by numbers. The diagonal dotted lines show those at the constant Jeans mass, whose values are indicated by numbers in the Figure. These figures are taken from Inayoshi and Omukai (2011).

and remains constant by the H Lyα cooling. If sufficient H_2 to cool forms during this isothermal collapse, the temperature drops by its cooling and the isothermal evolution is terminated. Otherwise, the isothermal evolution continues until very high density of $\sim 10^{16}$ cm^{-3}, where the cloud becomes optically thick to the H^- bound-free absorption (Omukai 2001). The H_2 concentration needed for its cooling to overcome the compressional heating is

$$y_{\rm cool}({\rm H_2}) = \frac{(3/2)k_{\rm B}T}{\mathcal{L}_{\rm H_2} t_{\rm ff}}, \tag{3.16}$$

where $\mathcal{L}_{\rm H_2} \equiv \Lambda_{\rm H_2}/n({\rm H_2})$ (erg s^{-1}) is the cooling rate per an H_2 molecule. Since most hydrogen is in the atomic form during the isothermal collapse, we assume $n({\rm H}) = n_{\rm H}$ in this Section. In Figure 3.5, we show $y_{\rm cool}({\rm H_2})$ (thick solid line) as a function of density for the isothermal collapse at 8000 K. Since $\mathcal{L}_{\rm H_2}$ increases linearly with number density until the critical density for LTE $n_{\rm H,cr} \simeq 3 \times 10^3$ cm^{-3} (at 8000 K) and saturates for higher density, $y_{\rm cool}({\rm H_2})$ decreases as $\propto n_{\rm H}^{-1/2}$ until $n_{\rm H,cr}$, reaches the minimum $\simeq 1.4 \times 10^{-7}$ there, and increases as $\propto n_{\rm H}^{1/2}$ for higher density. This $y_{\rm cool}({\rm H_2})$ is to be compared with the actual amount of H_2 present $y({\rm H_2})$. Before the temperature reaches $\simeq$ 8000 K, the H_2 concentration attains the equilibrium value set by the balance between the formation and destruction reactions. The effective rate coefficient of H_2 formation via H^- channel taking account of the H^- photodissociation is

$$k_{\rm form} = k_1 \frac{k_2 n_{\rm H}}{k_2 n_{\rm H} + k_3}, \tag{3.17}$$

where

$$k_3 = \beta_3 J_{21}, \tag{3.18}$$

by using $\beta_3 = 2 \times 10^{-7}$ (1×10^{-11}) for $T_* = 10^4$ K (10^5 K, respectively). This H_2 is destructed either by photodissociation (reaction 18), which is dominant at the low density where the FUV radiation is not shielded, or collisionally (reaction 7) at higher density. Equating the larger of those dissociation rates with the formation rate, we obtain the H_2 concentration

$$\begin{aligned} y(\mathrm{H_2}) &= \min(n_\mathrm{H} k_4^{-1}, k_5^{-1}) k_\mathrm{form} y(\mathrm{e^-}) \\ &\equiv \min(y_\mathrm{pd}(\mathrm{H_2}), y_\mathrm{cd}(\mathrm{H_2})). \end{aligned} \tag{3.19}$$

The photodissociation rate coefficient is written as

$$k_4 = \beta_4 J_{21}, \tag{3.20}$$

where $\beta_4 = 4.2 \times 10^{-12}$ (1.3×10^{-12}) for $T_* = 10^4$ K (10^5 K, respectively). In the above, we assume the cloud is transparent to the photodissociating radiation since $y_\mathrm{pd}(\mathrm{H_2})$ immediately exceeds $y_\mathrm{cd}(\mathrm{H_2})$ once the self-shielding becomes important. The values of $y(\mathrm{H_2})$ by equation (3.19) are plotted in Figure 3.5 for some combinations of T_* and J_{21} for the ionization degree $y(\mathrm{e^-}) = 4 \times 10^{-5}$, corresponding the no-CR/X-ray case (see later). The almost vertical portion of $y(\mathrm{H_2})$ on the low-density side is limited by the photodissociation ($y_\mathrm{pd}(\mathrm{H_2})$), while the gradually changing part at higher density is set by the collisional dissociation ($y_\mathrm{cd}(\mathrm{H_2})$). In the cases with $J_{21} = 0.1$ and 1 (10^3 and 10^4) for $T_* = 10^4$ K (10^5 K, respectively), $y(\mathrm{H_2})$ exceeds $y_\mathrm{cool}(\mathrm{H_2})$ at some density. At this moment, the actual temperature falls from $\simeq 8000$ K and the isothermal collapse terminates. On the other hand, in the case with $J_{21} = 20$ (2×10^4) for $T_* = 10^4$ K (10^5 K, respectively), $y(\mathrm{H_2})$ always remains below $y_\mathrm{cool}(\mathrm{H_2})$ and thus the isothermal collapse continues.

For density higher than the critical density $n_\mathrm{H,cr} \sim 10^3$ cm^{-3}, the H_2 concentration decreases owing to effective collisional dissociation from excited ro-vibrational levels and has no chance to reach $y_\mathrm{cool}(\mathrm{H_2})$ anymore. To initiate efficient H_2 cooling, H_2 concentration must exceed $y_\mathrm{cool}(\mathrm{H_2})$ before $n_\mathrm{H,cr}$. Thus, we can find the critical flux J_crit by the condition whether $y(\mathrm{H_2})$ at $n_\mathrm{H,cr} \sim 10^3$ cm^{-3} is higher than $y_\mathrm{cool}(\mathrm{H_2})$.

In the case of irradiation with hard FUV spectra (as $T_* = 10^5$ K), photodissociation limits the H_2 concentration and H^- photodissociation is relatively irrelevant (i.e., $k_\mathrm{form} \simeq k_1$). From the condition $y_\mathrm{pd}(\mathrm{H_2}) = y_\mathrm{cool}(\mathrm{H_2})$ at $n_\mathrm{H,cr}$, we obtain

$$J_\mathrm{crit} = \frac{1}{\beta_4} \frac{k_1 n_\mathrm{H,cr} y(\mathrm{e^-})}{y_\mathrm{cool}(\mathrm{H_2})}. \tag{3.21}$$

On the other hand, for softer FUV spectra, (as $T_* = 10^4$ K), the H_2 formation rate is significantly reduced by H^- photodissociation: $k_\mathrm{form} = k_1 k_2 n_\mathrm{H} / k_3$. The dotted line in Figure 3.5 shows $y_\mathrm{cd}(\mathrm{H_2})$ without H^- photodissociation, which exceeds $y_\mathrm{cool}(\mathrm{H_2})$

Table 3.1: Chemical reactions

number	reaction
1	$H + e^- \rightarrow H^- + \gamma$
2	$H^- + H \rightarrow H_2 + e^-$
3	$H^- + \gamma \rightarrow H + e^-$
4	$H_2 + \gamma \rightarrow 2H$
5	$H_2 + H \rightarrow 3H$
6	$H^+ + e^- \rightarrow H + \gamma$

before reaching $n_{\mathrm{H,cr}}$. The actual value of $y_{\mathrm{cd}}(\mathrm{H_2})$ is, however, suppressed by $\mathrm{H^-}$ photodissociation (see thin solid lines in Figure 3.5) and thus the $\mathrm{H_2}$ concentration is limited by collisional dissociation. Therefore, we obtain from the condition $y_{\mathrm{cd}}(\mathrm{H_2}) = y_{\mathrm{cool}}(\mathrm{H_2})$ at $n_{\mathrm{H,cr}}$:

$$J_{\mathrm{crit}} = \frac{k_2}{\beta_3 k_5} \frac{k_1 n_{\mathrm{H,cr}} y(\mathrm{e^-})}{y_{\mathrm{cool}}(\mathrm{H_2})}. \tag{3.22}$$

In general, the critical FUV flux is given by the larger of the above two values (equations 3.21 and 3.22).

Note that J_{crit} increases with the ionization degree $y(\mathrm{e^-})$, which can be evaluated as follows. Without external ionization, the ionization degree is governed by

$$\frac{dy(\mathrm{e^-})}{dt} = -k_6 n_{\mathrm{H}} y(\mathrm{e^-})^2. \tag{3.23}$$

Integrating this equation for a collapsing cloud (i.e., equation 3.1),

$$y(\mathrm{e^-}) = \frac{y_0(\mathrm{e^-})}{1 + 2k_6 y_0(\mathrm{e^-}) n_{\mathrm{H}} t_{\mathrm{ff}}}, \tag{3.24}$$

where $y_0(\mathrm{e^-})$ is the initial ionization degree. For density $> 50\ \mathrm{cm^{-3}}$, this renders $y(\mathrm{e^-}) = (2k_6 n_{\mathrm{H}} t_{\mathrm{ff}})^{-1}$. Equation (3.24) gives $y(\mathrm{e^-}) \simeq 4 \times 10^{-5}$ at $n_{\mathrm{H}} = 10^3\ \mathrm{cm^{-3}}$. Using the values at $10^3\ \mathrm{cm^{-3}}$, equations (3.21) and (3.22) lead to the critical FUV flux $J_{\mathrm{crit}} \sim 10$ (10^4) for $T_* = 10^4$ K (10^5 K, respectively), which are indeed similar to our numerical results for the no-CR/X-ray cases (Figure 3.3).

In the presence of strong CRs, the ionization degree is set by the balance between recombination and CR ionization:

$$y(\mathrm{e^-}) = \left(\frac{\zeta_{\mathrm{CR}}}{k_6}\right)^{1/2} n_{\mathrm{H}}^{-1/2}. \tag{3.25}$$

Comparing equations (3.24) and (3.25), we see that the CR ionization controls the ionization degree if its rate is higher than

$$\zeta_{\mathrm{CR,crit}} = \frac{1}{4k_6 n_{\mathrm{H}} t_{\mathrm{ff}}^2} \simeq 3.8 \times 10^{-19}\ \mathrm{s^{-1}}, \tag{3.26}$$

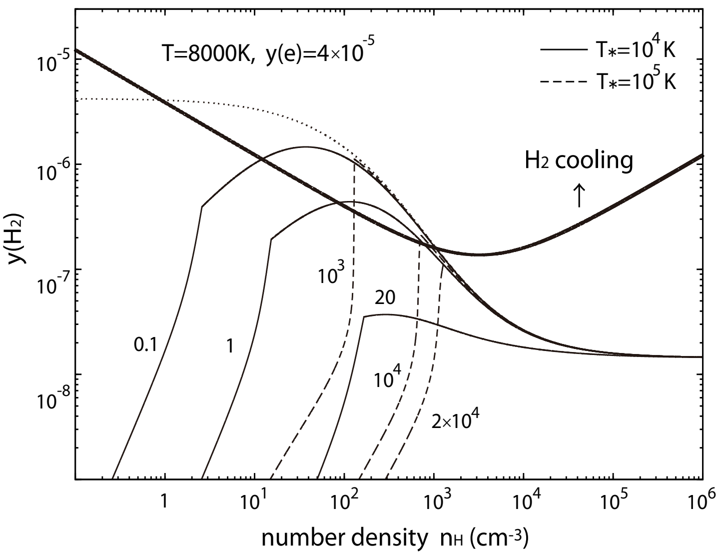

Figure 3.5: The H_2 concentration $y(H_2)$ estimated by equation (3.19) (thin lines) vs. that needed for its cooling to exceed the compressional heating $y_{\rm cool}(H_2)$ (thick line) in the isothermally collapsing clouds at 8000 K with the ionization degree $y(e^-) = 4\times10^{-5}$. The H_2 concentrations are shown for the FUV fields with brightness temperatures $T_* = 10^4$ K (thin solid lines) and 10^5 K (thin dashed lines). For each value of T_*, three cases with different FUV intensities J_{21}, which are indicated by numbers in the Figure, are presented. The dotted line shows $y_{\rm cd}(H_2)$ without H^- photodissociation. This figures is taken from Inayoshi and Omukai (2011).

where the last equation is evaluated at $T = 8000$ K. This value is equivalent to the CR energy density $U_{\rm CR,crit} \simeq 5.5\times10^{-15}$ erg cm^{-3} from equation (3.8). For $U_{\rm CR} > U_{\rm CR,crit}$, the ionization degree, as well as the critical FUV flux, increases as $\propto {U_{\rm CR}}^{1/2}$. This relation is reproduces well the behavior of $J_{\rm crit}$ as a function U_{15} shown in Figure 3.3 (a).

Next we consider the case of the X-ray ionization. Just the same as in the CR ionization, X-rays enhance the ionization degree as $y(e^-) \propto (J_{\rm X,21})^{1/2}$ and thus $J_{\rm crit} \propto (J_{\rm X,21})^{1/2}$ for $J_{\rm X,21} > 10^{-3}$, whose threshold is determined by the balance between recombination and X-ray ionization. This describes well the results shown in Figure 3.3 (b).

Our value of $J_{\rm crit} = 20$ for $T_* = 10^4$ K is smaller than $J_{\rm crit} = 39$ which Shang et al. (2010) estimated with one-zone model. This difference comes from the H_2-formation rate at high temperature: the rate coefficient we adopt (Galli and Palla 1998) is smaller than that Shang et al. (2010) used (Abel et al. 1997). On the other hand, our value of $J_{\rm crit} = 1.6\times10^4$ for $T_* = 10^5$ K is slightly larger than Shang et al. (2010) because we use the new shielding factor by Wolcott-Green and Haiman (2011).

Table 3.2: The IMF models of star-forming galaxies

model	IMF	mass ($\mathrm{M}_\odot$)	metallicity ($Z_\odot$)	T_* (K)
(i)	Salpeter	$1-100$	10^{-3}	10^4
(ii)	Salpeter	$1-100$	0	10^5
(iii)	top-heavy	40	0	10^5
(iv)	top-heavy	120	0	10^5

3.4 CR and X-ray from star-forming galaxies

So far, we have regarded the intensities of FUV, CRs and X-rays as free parameters in our calculation. All those radiation fields are, however, closely linked to the star-formation activity in galaxies and thus their intensities, i.e., J_{21}, U_{15} and $J_{\mathrm{X},21}$, are all proportional to the star formation rate (SFR). We here consider the star-forming galaxies with two types of initial mass function (IMF): the Salpeter IMF and the top-heavy one. For the Salpeter IMF, we take the mass range of $1-100\ \mathrm{M}_\odot$ and consider two cases of the stellar metallicity $Z = 10^{-3}\ Z_\odot$ and 0, which corresponds to Pop II and III star clusters, respectively. For Pop III galaxies, we also consider the two cases of the top-heavy IMF where all stars are $m_{\mathrm{OB}} = 40\ \mathrm{M}_\odot$ or $120\ \mathrm{M}_\odot$. The IMF models we study are summarized in Table 3.4.

For FUV flux, we use the Lyman-Werner photon emissivity from a star-forming galaxy for the IMF models calculated by Schaerer (2002, 2003):

$$J_{21} = \left\{ \begin{array}{c} 6.5\times 10^2 \\ 1.6\times 10^3 \\ 1.4\times 10^4 \\ 1.7\times 10^4 \end{array} \right\} \left(\frac{d}{10\ \mathrm{kpc}}\right)^{-2} \left(\frac{\mathrm{SFR}}{20\ \mathrm{M}_\odot\ \mathrm{yr}^{-1}}\right), \tag{3.27}$$

where d is the distance from the source, and the numbers in the bracket correspond to the IMF models in the same order as in Table 3.4

We assume that supernova remnants (SNRs) are the sources of CRs. The total CR energy from a SNR is written as (Stacy and Bromm 2007)

$$E_{\mathrm{CR}} = 10^{51} \left(\frac{p_{\mathrm{CR}}}{0.1}\right) \left(\frac{E_{\mathrm{SN}}}{10^{52}\ \mathrm{erg}}\right)\ \mathrm{erg}, \tag{3.28}$$

where p_{CR} is the fraction of SN explosion energy E_{SN} going into the CR energy. Using the supernova rate in the source galaxy

$$\dot{N}_{\mathrm{SN}} = \frac{f_{\mathrm{OB}}\ \mathrm{SFR}}{\bar{m}_{\mathrm{OB}}}, \tag{3.29}$$

where f_{OB}, $\bar{m}_{\mathrm{OB}}$ is the mass fraction and average mass of massive ($\geq 8\ \mathrm{M}_\odot$) stars, the CR energy density of U_{CR} is

$$U_{\mathrm{CR}} = \dot{N}_{\mathrm{SN}} \frac{E_{\mathrm{CR}}}{4\pi d^2 \langle v \rangle}, \tag{3.30}$$

where $\langle v \rangle$ is the average CR velocity. For the fiducial values of $p_{\rm CR} = 0.1$ and $E_{\rm SN} = 10^{52}$ erg, we obtain

$$U_{15} = \left\{ \begin{array}{c} 42 \\ 42 \\ 44 \\ 15 \end{array} \right\} \left(\frac{d}{10 \ {\rm kpc}}\right)^{-2} \left(\frac{\rm SFR}{20 \ {\rm M_\odot \ yr^{-1}}}\right). \tag{3.31}$$

From equations (3.27) and (3.31),

$$J_{21} = \left\{ \begin{array}{c} 15 \\ 38 \\ 3.1 \times 10^2 \\ 1.4 \times 10^3 \end{array} \right\} U_{15}. \tag{3.32}$$

X-rays are mainly emitted by high-mass X-ray binaries. Observationally, the X-ray luminosities in $2 - 10$ keV of local star-forming galaxies are related with their star formation rates as (e.g., Glover and Brand 2003)

$$L_{\rm X} = 1.2 \times 10^{40} \left(\frac{\rm SFR}{20 \ {\rm M_\odot \ yr^{-1}}}\right) \ {\rm erg \ s^{-1}}, \tag{3.33}$$

namely,

$$J_{\rm X,21} = 4.5 \times 10^{-3} \left(\frac{d}{10 \ {\rm kpc}}\right)^{-2} \left(\frac{\rm SFR}{20 \ {\rm M_\odot \ yr^{-1}}}\right). \tag{3.34}$$

Although this is an empirical relation for local galaxies, observations of Lyman-break galaxies provide supports for this to be valid as far as $z \sim 4$ (Glover and Brand 2003 and references therein). Here, we thus extend the relation (3.34) to high-redshift (say, $z \sim 10$) universe. From equations (3.27) and (3.34), we obtain

$$J_{21} = \left\{ \begin{array}{c} 1.4 \times 10^5 \\ 3.5 \times 10^5 \\ 3.0 \times 10^6 \\ 3.7 \times 10^6 \end{array} \right\} J_{\rm X,21}. \tag{3.35}$$

In Figure 3.3 (a), we plot the relations (3.32) for the IMF cases (i)-(iv) in Table 3.4. The FUV intensity and CR energy density from galaxies are expected to fall on this relation. In the case of Pop II radiation sources (i.e., type i), which are characterized by $T_* \sim 10^4$ K, the relation (3.32) intersects with the $J_{\rm crit}$ curve at $(J_{21}, U_{15}) = (20, 2)$, where the $J_{\rm crit}$ does not deviate yet from its no-CR value. This means that the CR ionization does not modify the value of $J_{\rm crit}$ significantly. On the other hand, for Pop III star clusters ($T_* \sim 10^5$ K), the critical FUV flux at the intersection points are > 20 (type ii), 10 (iii), and 2 times (iv) as large as $J_{\rm crit}$ in the no-CR case, respectively. Namely, the CR ionization drastically changes the critical FUV flux except for the case with the top-heavy IMF with $m_{\rm OB} = 120$ M$_\odot$.

In Figure 3.3 (b), we also plot the relations (3.35) between J_{21} and $J_{\rm X,21}$. As in the case of CRs, the X-ray ionization effects become important for higher T_*, in particular, $T_* > 10^4$ K.

3.5 Conclusion and Discussion

We have calculated the thermal evolution of primordial clouds under strong far-ultraviolet (FUV) fields, along with cosmic rays (CRs)/X-rays. In the cloud under a FUV field exceeding a threshold, the H_2 cooling is suppressed at any density. Such a cloud collapses almost isothermally at 8000 K by hydrogen atomic cooling. According to numerical simulations (Bromm and Loeb 2003), it avoids fragmentation and collapses directly to a supermassive star (SMS).

Without external ionization by CRs/X-rays, the critical FUV flux is $J_{\rm crit} \simeq 1.6 \times 10^4$ (in units of 10^{-21} erg s^{-1} cm^{-2} sr^{-1} Hz^{-1}) for a diluted black body spectrum with brightness temperature $T_* = 10^5$ K, while it is as small as $J_{21} \simeq 20$ for $T_* = 10^4$ K. This dependence on T_* comes from the higher H^- photodissociation (> 0.755 eV) rate for lower T_* at the same J_{21} normalized at 13.6 eV. Since H_2 is produced through the H^- channel, the larger H^- photodissociation reduces the amount of H_2 and thus the value of $J_{\rm crit}$.

We have studied how this critical FUV flux changes with simultaneous irradiation of either CRs or X-rays. In the case of CR irradiation, the critical FUV flux $J_{\rm crit}$ begins to increase with the CR energy density $U_{\rm CR} > 10^{-14}$ erg cm^{-3} and depends as $J_{\rm crit} \propto {U_{\rm CR}}^{1/2}$ asymptotically. Similarly, for X-ray irradiation, $J_{\rm crit} \propto {J_{\rm X}}^{1/2}$ for $J_{\rm X} > 10^{-24}$ erg s^{-1} cm^{-2} sr^{-1} Hz^{-1} at 1 keV. In both cases, the increase of the critical FUV flux is caused by the enhanced ionization by CRs/X-rays, which promotes the H_2 formation and cooling.

FUV intensity and CRs/X-rays from star-forming galaxies are expected to correlate each other since they all trace the massive-star forming activity. Using the expected relations between FUV intensity and CRs/X-rays, we have found that if the initial mass function (IMF) of the radiation source is Salpeter-like and the brightness temperature of the FUV radiation is rather high $T_* \sim 10^5$ K, the critical FUV intensity increases significantly $J_{\rm crit} \sim 10^6$ owing to ionization by CRs and X-rays. Even with the top-heavy IMF, the critical FUV intensity increases to $J_{\rm crit} \sim 10^5$ unless the stellar mass is > 100 $M_\odot$. Since the fraction of halos exposed to FUV flux exceeding $J_{\rm crit}$ decreases exponentially with $J_{\rm crit}$ for $> 2 \times 10^3$ (Dijkstra et al. 2008), there is little possibility ($< 10^{-28}$) for such intense FUV field realized in any halos. We conclude that if the radiation source is composed of Pop III stars with brightness temperature $\sim 10^5$ K and contains sources of CRs/X-rays, its IMF must be very top-heavy > 100 $M_\odot$ to enable SMS formation in nearby halos. Other possible radiation sources enabling SMS formation include, e.g., sources with low brightness temperature, $T_* \simeq 10^4$ K, such as Pop II/I star clusters, or those with high T_* but without strong CRs and X-rays. The latter possibility is realized if a Pop III star cluster is so young that it harbors neither supernova remnants nor high-mass X-ray binaries.

Finally, we discuss limitations of our analysis. In our model, we have assumed that the external radiation is attenuated with the column density estimated by the central density and the size of the core, which is given by the Jeans length. Although the column density of the core is given by this value for the Larson-Penston solution, the contribution from the envelope needs to be added. But we can see the envelope contribution is not significant by the following consideration. The steep decline of density with radius as $\rho \propto r^{-2}$ limits the column density of hydrogen nuclei N_{H} in the envelope at most that of the core. Due to the photodissociation and low formation rate, the H_2 abundance is remarkably lower in the envelope than in the core. Therefore, the envelope contribution to the column density of H_2, which is relevant for evaluating the critical FUV intensity, is small and the H_2 column density is well approximated by that of the core. Another concern is about the geometry of the cloud. In the low-density regime we considered, the cloud shape can strongly deviate from the sphere. Even though the clouds are in such shapes as sheet-like or filamentary, however, the length scale of the shortest axis, which is most relevant for the shielding effects, is still roughly given by the Jeans length, and thus the our assumption of the Jeans length shielding remains valid. In fact, Shang et al. (2010), who studied the evolution of the primordial clouds under strong FUV irradiation and compared the results by the one-zone model and those by the cosmological three-dimensional simulation, found very good agreements as for the thermal evolution at the center of the clouds, as well as for the critical FUV intensity J_{crit} needed to quench the H_2 formation/cooling. In addition, we assume that the clouds are isotropically irradiated by FUV, as well as CRs and X-rays. However, such intense FUV field as exceeding the critical value J_{crit} tends to be dominated by a nearby single large source, rather than by a collective effect of a large number of sources (Dijkstra et al. 2008). We suspect that, in the case of such anisotropic radiation field, more intense sources are necessary to induce SMS formation as the radiation comes from only limited solid angles. To confirm it, however, detailed modeling is required, which is beyond the scope of this thesis.

Chapter 4

SMBH formation by cold accretion shocks in first galaxies

As a promising process to form SMBHs in the high-z universe, the possibility of massive seed BH formation by direct collapse of SMS ($\gtrsim 10^5\ M_\odot$) has been considered. Specifically, SMS formation requires primordial gas in massive halos ($T_{\rm vir} \gtrsim 10^4$ K) irradiated with strong FUV radiation to suppress the H_2 cooling and efficient gas fragmentation (e.g., Bromm and Loeb 2003; Regan and Haehnelt 2009a,b; Shang et al. 2010). This scenario, however, has a serious drawback: for this mechanism of SMS formation to work, extremely strong FUV radiation $J_{21}^{\rm LW} \gtrsim 10^2 - 10^3$ is required (Omukai 2001; Bromm and Loeb 2003; Shang et al. 2010), while the fraction of halos irradiated with such intense FUV fields with $J_{21}^{\rm LW} \gtrsim 10^3$ is estimated to be $\lesssim 10^{-6}$ at $z \sim 10$ (Dijkstra et al. 2008), i.e., only extremely rare halos satisfy the condition for SMS formation. Moreover, as we describe in the previous section, if high energy components, such as cosmic rays or X-rays, are present along with the FUV radiation, their ionization effect promotes the H_2 formation and then strongly suppresses the SMS formation (Inayoshi and Omukai 2011). Although the above scenario might be still viable considering the rarity of high-z SMBHs, it is worthwhile to explore another possibility.

In this section, we propose a new scenario for SMS formation in post-shock gas of cold accretion flows in forming first galaxies. Recent numerical simulations of galaxy formation have revealed that, in halos with virial temperature $T_{\rm vir} \gtrsim 10^4$ K, the shock position does not stay at the virial radius and shrinks inside owing to the efficient Lyα cooling, and the accreting cold gas penetrates deep to the center through dense filamentary flows (Birnboim and Dekel 2003; Kereš et al. 2005; Dekel and Birnboim 2006; Dekel et al. 2009; Bromm and Yoshida 2011). The supersonic flows collide each other and the resultant shock develops a hot and dense ($\sim 10^4$ K and $\sim 10^3\ {\rm cm}^{-3}$) gas near the center (Wise and Abel 2007; Wise et al. 2008). By studying thermal evolution of the shocked gas, we have found that, if the post-shock density is high enough for the H_2 rovibrational levels to reach the LTE, the efficient collisional dissociation suppresses H_2 cooling, and the gas cannot cool below several thousand K. Massive clouds with $\gtrsim 10^5\ M_\odot$ formed by fragmentation of the post-shock layer subsequently collapse isothermally at ~ 8000 K by the Lyα cooling. Without further fragmentation, monolithic collapse of the clouds results in the SMS formation. Note that, unlike the previous SMS formation mechanism, strong FUV radiation is not required in our scenario. Similar analysis has also been carried out by Safranek-Shrader et al. (2010), who studied the fragmentation of the cold-stream shocked layer considering the effects of radiation field and chemical enrichment, but for a single post-shock condition ($4 \times 10^3 \mathrm{cm}^{-3}$, 1.1×10^4 K, and the equilibrium chemical abundances).

In this chapter, we discuss the new pathway to form SMSs at the epoch of the first galaxy formation without requiring strong FUV radiations. In section 4.1, we describe the model for calculation of thermal evolution in the shocked gas. In section 4.2, we present our results and clarify the conditions for isothermal collapse leading to the SMS formation in terms of post-shock density and temperature. Effects of metal enrichment is also considered here. In section 4.3, we analyze thermal processes in the shocked gas and discuss the reason for the bifurcation of thermal evolution in more detail. Finally, we summarize our study and present some discussions in section 4.4.

4.1 Setups of our models

In this section, we describe our model for calculation of thermal evolution in hot and dense shocked regions formed by collision of cold accretion flows in the first galaxies.

4.1.1 Evolution in the post-shock layer

We consider the thermal evolution in the post-shock layer under the assumption that the flow is steady and plane-parallel. Since the post-shock temperature is as high as the virial temperature of first-galaxy forming halos ($T_{\mathrm{vir}} \gtrsim 10^4$ K), cooling by the Lyα emission is efficient early on. The post-shock flow is compressed almost isobarically as long as the gas cools effectively (e.g., Shapiro and Kang 1987). Within the steady-state approximation, the conservation of mass and momentum leads to the following relationships between the density ρ_0, pressure p_0, and flow velocity v_0 just behind the shock with those in the post-shock flow ρ, p, and v:

$$\rho v = \rho_0 v_0, \tag{4.1}$$

$$\rho v^2 + p = \rho_0 v_0^2 + p_0. \tag{4.2}$$

Along this flow, we solve the energy equation

$$\frac{dE}{dt} = \frac{p+E}{\rho}\frac{d\rho}{dt} - \Lambda_{\mathrm{net}}, \tag{4.3}$$

where E is the internal energy per unit volume, d/dt is the Lagrangian time derivative, and Λ_{net} is the net cooling rate per unit volume. Assuming a strong shock and neglecting the thermal pressure in the pre-shock flow, $p_0 \simeq 3\rho_0 v_0^2$ is satisfied just behind the shock front. Thus, we approximate the right-hand side of equation (4.2) by $4\rho_0 v_0^2$. The cooling term $\Lambda_{\rm net}$ includes the radiative cooling by H, H_2 and HD, and cooling/heating associated with chemical reactions. We solve the chemical reactions of primordial gas among the following 14 species; H, H_2, e^-, H^+, H_2^+, H^-, He, He^+, He^{++}, D, HD, D^+, HD^+, and D^-. We adopt the same coefficients for the cooling/heating and the chemical reactions as in Inayoshi and Omukai (2011) except for omitting the radiative/cosmic-ray ionization and dissociation in this calculation. In studying effects of metal enrichment, we add the cooling by the fine-structure-line emission of $C_{\rm II}$ and $O_{\rm I}$ to the primordial processes described above. Assuming the fraction of metals depleted to dust grains to be the same as in the Galactic interstellar gas, we set the number fractions of C and O nuclei in the gas phase with respect to H nuclei to $x_{\rm C,gas} = 0.927 \times 10^{-4}(Z/Z_\odot)$ and $x_{\rm O,gas} = 3.568 \times 10^{-4}(Z/Z_\odot)$ (Pollack et al. 1994). We follow Hollenbach and McKee (1989) in calculating the cooling rates of $C_{\rm II}$ and $O_{\rm I}$. We curtail the C and O chemistry by simply assuming that all the C and O are in the states of $C_{\rm II}$ and $O_{\rm I}$, respectively, from the following consideration: with lower ionization energy (11.26 eV) than H atom, C is photoionized by weak background radiation and in the state of $C_{\rm II}$, while O is in ionization equilibrium with H and almost neutral for $\lesssim 8000$ K, where the $O_{\rm I}$ cooling is important. Molecular cooling of metals (e.g., CO and H_2O) is not included since its cooling is not important in the temperature range relevant for the bifurcation of thermal evolution ($\gtrsim$ several 10^3 K).

4.1.2 Sheet fragmentation and subsequent evolution

Next, we consider the condition for the gravitational instability during the isobaric compression of the post-shock layer and thus for its fragmentation. For the isobaric compression, the dynamical time $t_{\rm dyn}(\equiv \rho/(d\rho/dt))$, which characterizes thermal evolution, is approximately equal to the cooling time

$$t_{\rm cool} = \frac{(3/2) n_{\rm H} k_{\rm B} T}{\Lambda_{\rm net}}, \tag{4.4}$$

where $n_{\rm H}$ is the number density of H nuclei and T is the temperature. On the other hand, the growth timescale for the gravitational instability is given by the free-fall time (e.g., Larson 1985)

$$t_{\rm ff} = \sqrt{\frac{32}{3\pi G\rho}}. \tag{4.5}$$

As long as the cooling is effective enough and so $t_{\rm cool}(\simeq t_{\rm dyn}) \lesssim t_{\rm ff}$, the post-shock layer continues to be compressed isobarically. However, once the cooling becomes ineffective and $t_{\rm cool}$ exceeds $t_{\rm ff}$, the contraction of the layer halts and a dense layer begins to develop inside the post-shock region. For example, since the growth rate of the baryonic mass in halos of $\sim 10^8\ M_\odot$ at $z \sim 10$ is $\sim 4 \times 10^{-2}\ M_\odot\ {\rm yr}^{-1}$ (Dekel et al. 2009), a gas of $\gtrsim 10^5\ M_\odot$ can accumulate in $\gtrsim 3 \times 10^6$ yrs. If sufficient gas supply is available through the accretion flow, the dense layer eventually satisfies the Jeans criterion, i.e., the sound-crossing time $t_{\rm cross}$ becomes longer than the free-fall time ($t_{\rm cross} \gtrsim t_{\rm ff}$). The layer then fragments by the gravitational instability to produce Jeans-scale clouds. In this section, assuming that the continuous gas supply to induce the Jeans instability is available, we estimate the fragmentation mass scale by the condition $t_{\rm ff} \sim t_{\rm cool}$ in accordance with Yamada and Nishi (1998).

After fragmentation, the cloud collapses with its self-gravity, and its evolution cannot be modelled as a steady flow anymore. Density evolution in a cloud collapsing by the self-gravity is described by the Penston-Larson self-similar solution (Penston 1969; Larson 1969). We here calculate the evolution in the central-core part by using a one-zone model as we described in section 3.1. Namely, after the condition for fragmentation ($t_{\rm cool} \gtrsim t_{\rm ff}$) is satisfied, we switch the density evolution described by equations (4.1)-(4.2) to that by equation (3.1) in our calculation and solve equation (4.3) for this density evolution.

4.1.3 Initial conditions

According to numerical simulations of the first galaxy formation (Greif et al. 2008; Wise et al. 2008), the pre-shock number density and temperature of cold flows and the shock velocity are typically 10^3 cm^{-3}, 200 K, and 20 km s^{-1}, respectively, which correspond to the post-shock density 4×10^3 cm^{-3} and temperature 9000 K. With those fiducial values in mind, we carry out calculations for a wide range of initial number density and temperature: $10^2\ {\rm cm^{-3}} < n_{\rm H,0} < 10^7\ {\rm cm^{-3}}$ and $3000\ {\rm K} < T_0 < 10^5$ K. Since H_2, the main coolant below 8000 K, forms through the electron-catalyzed reactions (H^- process), the initial ionization degree $x_{\rm e,0}$, along with the initial H_2 concentration $x_{\rm H_2,0}$, is important quantities for the subsequent thermal evolution. In reference to the results of Kang and Shapiro (1992), who studied the chemical abundances in the pre-shock gas considering photo-ionization and dissociation by UV radiation emitted from the shock, we regard $x_{\rm e,0} \sim 10^{-2}$ and $x_{\rm H_2,0} \sim 10^{-6}$ as typical ionization degree and molecular fraction, respectively. However, since cold accretion flows are far denser ($\sim 10^3$ cm^{-3}) than the range Kang and Shapiro (1992) assumed ($\lesssim 10^{-2}$ cm^{-3}), the electron recombination as well as the shielding of the UV photo-ionization/dissociation probably lower the pre-shock ionization degree $x_{\rm e,0}$ and elevate molecular fraction $x_{\rm H_2}$ from those values. Taking this uncertainty into account, we study the cases with a wide range of initial ionization degree and H_2 fraction: $10^{-5} \le x_{\rm e,0} \le 10^{-1}$ and $10^{-6} \le x_{\rm H_2,0} \le 10^{-3}$.

4.2 Results

In this section, we present our results for thermal evolution after the gas experiences the cold accretion shock. We first consider the cases of primordial gas and then discuss effects of small metal enrichment.

4.2.1 Primordial-gas case

In Fig. 4.1, we show the temperature evolution of primordial gas for four post-shock conditions, indicated by two each open and filled circles. We here set the initial ionization degree and molecular fraction to $x_{\mathrm{e},0} = 10^{-2}$ and $x_{\mathrm{H_2},0} = 10^{-6}$, respectively. First, we see the cases from the open-circle initial conditions in Fig. 4.1, whose temperature evolution is shown by the dashed lines. In the lower initial-density case ($n_{\mathrm{H},0}$, T_0)=(5×10^2 cm^{-3}, 3.6×10^4 K) among them, the post-shock gas cools by the Lyα emission and is compressed isobarically. Although the Lyα cooling becomes inefficient below 8000 K, enough $\mathrm{H_2}$ for cooling has already been formed by this time, which enables further temperature decrease. HD is formed abundantly for $\lesssim$ 150 K, whose cooling eventually lowers the temperature to $\sim$ 50 K. At this point, without efficient coolant anymore, t_{cool} becomes longer than t_{ff}. Clouds with Jeans mass of several 10 $M_{\odot}$ are produced by the gravitational instability. Also, in the case of lower initial temperature (10^5 cm^{-3}, 3.3×10^3 K), abundant $\mathrm{H_2}$ is formed immediately. The cooling by $\mathrm{H_2}$ and then by HD allows the temperature to plummet isobarically until $\sim$ 100 K, where the fragmentation mass scale of a few 10 $M_{\odot}$ is imprinted. In both the cases, temperature evolution after fragmentation converges to the well-known track for clouds collapsing by the self-gravity and cooling by $\mathrm{H_2}$ and HD (lower thin solid line; Uehara and Inutsuka 2000; Nagakura and Omukai 2005).

Next, we see the two cases starting from the filled-circle initial conditions in Fig. 4.1, whose evolutionary tracks are indicated by the dash-dotted lines. In the higher initial temperature case (10^4 cm^{-3}, 3.6×10^4 K), the gas cools isobarically until 8000 K as in the open-circle cases. At $\sim$ 8000 K, however, the density exceeds $\sim 10^4$ cm^{-3}, the critical density for $\mathrm{H_2}$ to reach LTE. For higher density, $\mathrm{H_2}$ is rapidly dissociated collisionally from the excited rovibrational levels, and thus sufficient $\mathrm{H_2}$ for cooling is never formed. Consequently, the gas cannot cool below $\sim$ 8000 K, and massive clouds with $\gtrsim 10^5$ $M_{\odot}$ are formed by fragmentation. Also, in the case of initial temperature somewhat lower than 8000 K (2×10^5 cm^{-3}, 5×10^3 K), $\mathrm{H_2}$ cooling is suppressed by the collisional dissociation and fragmentation occurs immediately producing massive clouds with $\gtrsim 10^5$ $M_{\odot}$, whose temperature increases to 8000 K by the compressional heating in the course of gravitational collapse. In both cases, the massive clouds thereafter collapse almost isothermally by the Lyα cooling until very high density ($\sim 10^{16}$ cm^{-3}), where the cloud becomes optically thick to the $\mathrm{H^-}$ bound-free absorption (Omukai 2001). Such isothermally contracting clouds do not fragment in the later phase and thus collapse monolithically to SMSs, which eventually evolve to seeds of SMBHs (Bromm et al. 2003; Shang et al. 2010).

As seen above, the behaviors of thermal evolution can be classified into two types. The thick solid line in Fig. 4.1 corresponds to the boundary of initial conditions, from

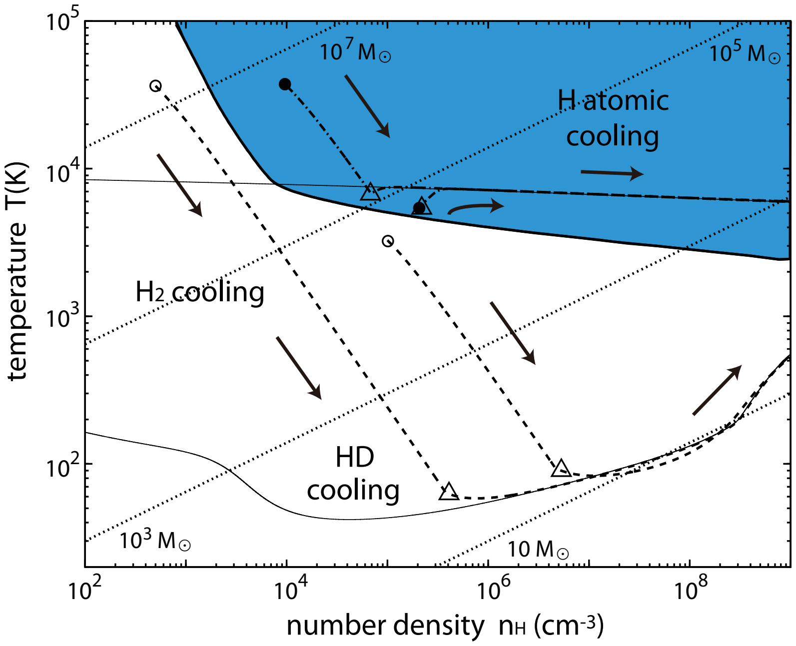

Figure 4.1: The temperature evolution of primordial gas after heated by the cold accretion shock for the initial ionization degree $x_{e,0} = 10^{-2}$ and H_2 fraction $x_{H_2,0} = 10^{-6}$. The evolutionary tracks are shown with dashed and dash-dotted lines for four combinations of initial temperature and density, indicated by two each open and filled circles. The triangle symbol on each track indicates the epoch when the post-shock layer fragments by the gravitational instability. The thick solid line, the domain above which is hatched, divides the initial conditions leading to these two different ways of thermal evolution. The two thin solid lines show the temperature evolution by the H atomic cooling (upper) and the H_2 and HD cooling (lower), respectively. The diagonal dotted lines (lower-left to upper-right) indicate the constant Jeans masses, whose values are denoted by numbers in the Figure. This figures is taken from Inayoshi and Omukai (2012).

the above or below which subsequent thermal evolution bifurcates. Namely, the post-shock conditions above the boundary (the hatched region) lead to the isothermal evolution at $\sim$ 8000 K, while those below it result in the isobaric temperature decrease until $\lesssim$ 100 K. The boundary on the low-density side ($n_{\rm H,0} \lesssim 10^4\ {\rm cm}^{-3}$) can be fitted as

$$T_0 \gtrsim 8 \times 10^3 \left(\frac{n_{\rm H,0}}{7 \times 10^3\ {\rm cm}^{-3}} \right)^{-1}\ {\rm K}. \tag{4.6}$$

This means that, after isobaric cooling to 8000 K, if the density exceeds the H_2 critical value for LTE ($\sim 10^4\ {\rm cm}^{-3}$), the gas cannot continue further isobaric compression and starts isothermal collapse. For higher densities $n_{\rm H,0} \gtrsim 10^4\ {\rm cm}^{-3}$, the boundary is given by

$$T_0 \gtrsim 5 \times 10^3 \left(\frac{n_{\rm H,0}}{10^5\ {\rm cm}^{-3}} \right)^{-0.1}\ {\rm K}. \tag{4.7}$$

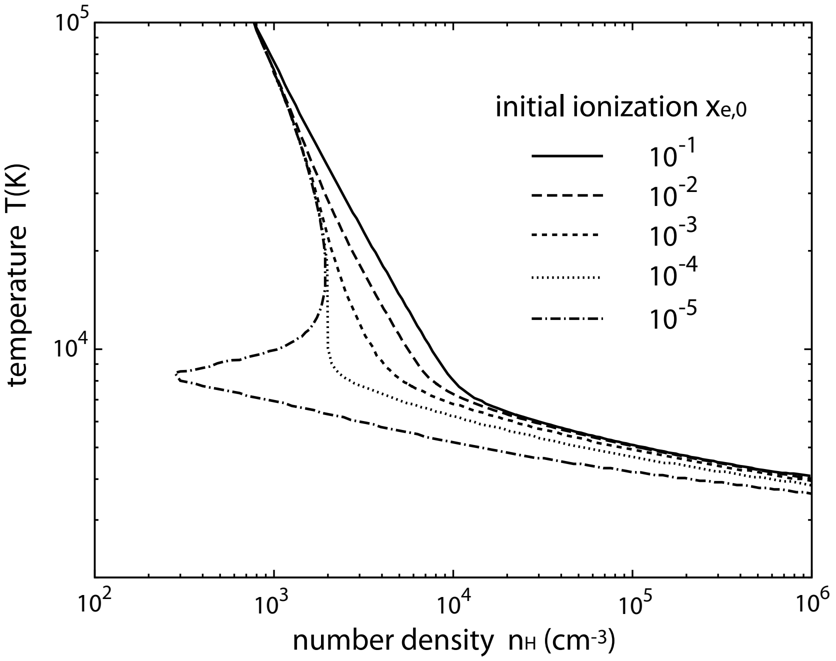

Figure 4.2: The effect of initial ionization degree on the range of post-shock initial conditions leading to isothermal collapse by H atomic cooling and thus SMS formation. The lines present their boundaries for the cases with different initial ionization degrees of $x_{\rm e,0} = 10^{-1}$ (solid), 10^{-2} (long-dashed), 10^{-3} (short-dashed), 10^{-4} (dotted), and 10^{-5} (dash-dotted), respectively. The molecular fraction $x_{\rm H_2,0} = 10^{-6}$ for all cases. This figures is taken from Inayoshi and Omukai (2012).

In Section 4, we discuss physical processes determining the location of the boundary in more detail.

We mention the effect of initial chemical composition on thermal evolution. In Fig. 4.2, we show the boundaries for the SMS-forming conditions for different initial ionization degrees ($10^{-5} \leq x_{\rm e,0} \leq 10^{-1}$). The positions of the boundaries are almost independent of $x_{\rm e,0}$ for $\gtrsim 10^4$ cm^{-3}, while the portions at $\lesssim 10^4$ cm^{-3} move to lower density with decreasing $x_{\rm e,0}$. In particular, for $x_{\rm e,0} = 10^{-5}$, this results in the spiky domain around 8000 K extending as low as $\sim 3 \times 10^2$ cm^{-3}. With the higher initial ionization degree, the more H_2 is formed by the electron-catalyzed reactions, which results in the wider range of post-shock conditions for H_2 cooling, i.e., the smaller range for SMS formation. The boundary for $x_{\rm e,0} \leq 10^{-2}$ asymptotically approaches that for higher $x_{\rm e,0}$ at $\gtrsim 3 \times 10^4$ K since the ionization degree jumps up immediately to $\sim 10^{-1}$, even with smaller initial value, by effective collisional ionization

$$\mathrm{H} + \mathrm{e}^- \rightarrow \mathrm{H}^+ + 2\ \mathrm{e}^-, \tag{4.8}$$

in this temperature range. We also studied the cases with different molecular fraction $x_{\rm H_2,0} = 10^{-6}, 10^{-4}$ and 10^{-3}, and found that the boundaries for SMS formation is

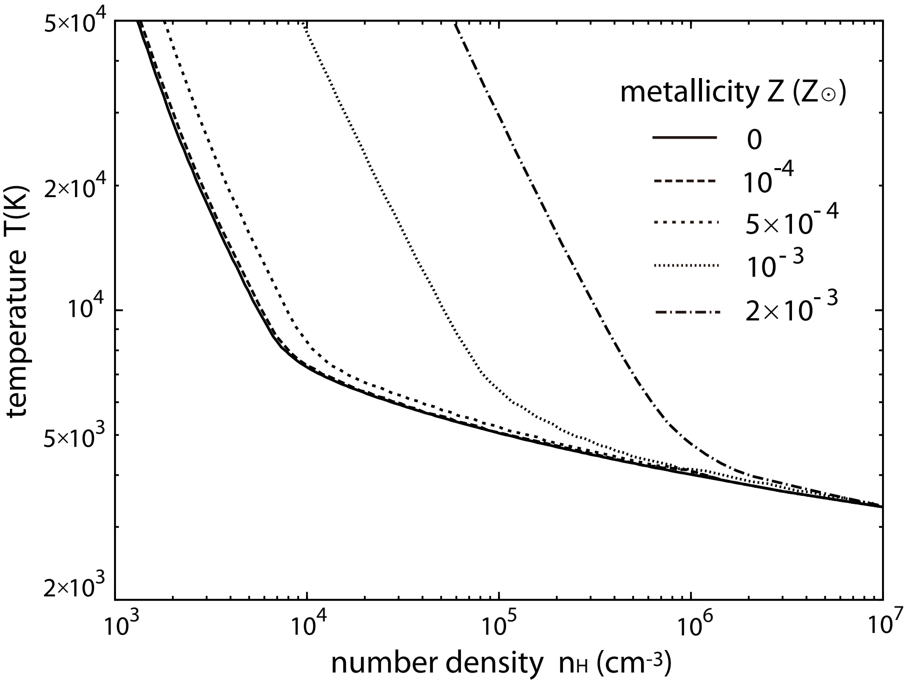

Figure 4.3: The effect of metallicity on the range of post-shock initial conditions leading to SMS formation. The lines present their boundaries for the cases of metallicity $Z = 0$ (solid), 10^{-4} (long-dashed), 5×10^{-4} (short-dashed), 10^{-3} (dotted), 2×10^{-3} $Z_{\odot}$ (dot-dashed), respectively. With metallicity higher than $Z_{\rm cr} = 10^{-3}$ $Z_{\odot}$, the boundary remarkably shifts toward higher density. The initial ionization degree and molecular fraction are $x_{\rm e,0} = 10^{-2}$ and $x_{\rm H_2,0} = 10^{-6}$, respectively. This figures is taken from Inayoshi and Omukai (2012).

almost independent of $x_{\rm H_2,0}$. This is because, even with high initial value, H_2 is rapidly dissociated collisionally for $\lesssim 10^4 {\rm cm}^{-3}$, and its fraction reaches the equilibrium one, which is independent of initial value.

4.2.2 Metallicity effect

Next, we consider the cases with slight metal enrichment. In Fig. 4.3, we present the boundaries for SMS-forming initial conditions for various metallicities with $0 \leq Z \leq 2 \times 10^{-3}$ $Z_{\odot}$. With some metals, cooling by the fine-structure line emission of $\rm C_{II}$ and $\rm O_{I}$ can exceed that by H_2 and plays an important role in thermal evolution. With metallicity as low as $Z \lesssim 5 \times 10^{-4}$ $Z_{\odot}$, the metal cooling does not affect thermal evolution around 8000 K and the boundary does not move from the primordial case. As seen in Section 3.1, from initial conditions hotter and denser than the boundary (i.e., the hatched region of Fig. 4.1), enough H_2 for cooling is not formed and only massive clouds are produced, which collapse isothermally thereafter. With increasing metallicity, the metal-line cooling becomes able to make the gas to cool below ~ 5000

K isobarically even without H_2. Once the temperature decreases and the collisional dissociation becomes ineffective, abundant H_2 eventually forms and the gas cools to $\lesssim 100$ K by its cooling. By this additional cooling, the boundary of the SMS-forming initial conditions moves to higher density. With metallicity as high as $Z \sim 10^{-3}\ Z_\odot$, the cooling rate by $C_{\rm II}$ and $O_{\rm I}$ becomes comparable to the compressional heating at ~ 8000 K and $\sim 10^4$ cm^{-3}. Therefore, even without help of H_2 cooling, the metal cooling alone is able to lower the temperature to the range where the H_2 collisional dissociation is ineffective, and thus the boundary shifts to higher density.

In summary, with metallicity higher than the critical value $Z_{\rm cr} \sim 10^{-3}\ Z_\odot$, the boundary density becomes far higher than the typical post-shock value by the cold accretion shock $\sim 10^3$ cm^{-3} and such an initial condition would be very difficult to be realized. Thus the possibility of SMS formation is strongly reduced for higher metallicity. On the other hand, as long as $Z < Z_{\rm cr}$, the range of initial conditions for SMS formation remains the same as in the primordial case.

4.3 Mechanism for the bifurcation of thermal evolution of the post-shock gas

In this Section, we explain what processes are responsible for the bifurcation of thermal evolution in the region where the cold accretion shock is thermalized, and give a physical interpretation for the location of the bifurcation boundary for the post-shock conditions in Figs. 4.1 and 4.2.

Efficient Lyα cooling drives temperature in a hot gas rapidly to $\simeq 8000$ K, where its cooling rate is sharply cut off as the atomic hydrogen is not excited for lower temperature. In Fig. 4.4, we show the cut-off temperature (dotted line), below which H_2 takes over the role of the dominant coolant. Thus, for the post-shock gas to continue the isobaric cooling below 8000 K, the H_2 cooling must become effective and keep the cooling time $t_{\rm cool}$ shorter than the free-fall time $t_{\rm ff}$. The cooling time by the H_2 cooling is given by

$$t_{\rm cool} = \frac{(3/2)k_{\rm B}T}{\mathcal{L}_{\rm H_2} x_{\rm H_2}}, \tag{4.9}$$

where $\mathcal{L}_{\rm H_2} = \Lambda_{\rm H_2}/(n_{\rm H} x_{\rm H_2})$ is the cooling rate per an H_2 molecule (erg s^{-1}) and has the density dependence $\mathcal{L}_{\rm H_2} \propto (1 + n_{\rm H,cr}/n_{\rm H})^{-1}$ ($n_{\rm H,cr} \simeq 10^4$ cm^{-3} is the H_2 critical density for LTE). In conditions under consideration (below the dotted line of Fig. 4.4), the H_2 fraction $x_{\rm H_2}$ is set by the equilibrium between the electron-catalyzed formation reaction and collisional dissociation reaction [*], and so

$$x_{\mathrm{H}_2} = \frac{k_{\mathrm{form}}}{k_{\mathrm{cd}}} x_{\mathrm{e}}, \tag{4.10}$$

where k_{form} ($\mathrm{H} + \mathrm{e}^- \rightarrow \mathrm{H}^- + \gamma$) and k_{cd} ($\mathrm{H}_2 + \mathrm{H} \rightarrow 3\mathrm{H}$) are reaction rate coefficients for the indicated reactions, respectively. Note that k_{cd} depends on the fraction of H_2 in excited states and thus on the density. The rate coefficient k_{cd} significantly increases with density near the H_2 critical density $n_{\mathrm{H,cr}}$, which results in the rapid decrease of x_{H_2} by the effective collisional dissociation at $\gtrsim 10^3$ cm^{-3}.

Furthermore, since x_{H_2} is proportional to x_{e}, the recombination also can be a key reaction to determine t_{cool} ($\propto x_{\mathrm{e}}^{-1}$) at $\lesssim 8000$ K. Since the recombination time t_{rec} ($= 1/\alpha_{\mathrm{rec}} n_{\mathrm{H}} x_{\mathrm{e}}$; α_{rec} is the recombination rate coefficient) has the same dependence on x_{e} as t_{cool}, the ratio of these two timescales becomes independent of x_{e} and is approximately given by

$$\begin{aligned} \frac{t_{\mathrm{cool}}}{t_{\mathrm{rec}}} &= \frac{(3/2) n_{\mathrm{H}} k_{\mathrm{B}} T}{\mathcal{L}_{\mathrm{H}_2}} \frac{k_{\mathrm{cd}} \alpha_{\mathrm{rec}}}{k_{\mathrm{form}}} \\ &\simeq 0.9 \left(\frac{T}{5000\ \mathrm{K}} \right)^{9.0} \left(\frac{n_{\mathrm{H}}}{10^4\ \mathrm{cm}^{-3}} \right). \end{aligned} \tag{4.11}$$

The last expression above is valid for the density and temperature around $t_{\mathrm{cool}} \simeq t_{\mathrm{rec}}$ and $\gtrsim 10^4$ cm^{-3}, and the large temperature dependence of equation (4.11) is due to that of k_{cd}. In Fig.4.4, we show the range of the parameters satisfying $t_{\mathrm{cool}} > t_{\mathrm{rec}}$ (the hatched region), where the recombination effectively works during the isobaric contraction. Note that the hatched region appears only at $\gtrsim 10^3$ cm^{-3}, where k_{cd} is enhanced significantly. On the other hand, the ionization degree is frozen during the isobaric compression at the density lower than the hatched region as $t_{\mathrm{cool}} < t_{\mathrm{rec}}$. Under constant x_{e}, the cooling time becomes shorter and shorter with decreasing temperature as $t_{\mathrm{cool}} \propto T^{9.7}$ (at $\simeq 5000$ K) because the collisional dissociation is strongly suppressed for lower temperature. Thus the efficient H_2 cooling and resultant isobaric evolution continue until ~ 100 K.

We first consider the cases with $x_{\mathrm{e},0} \gtrsim 10^{-4}$ and defer the discussion for the lower ionization cases later. As an example, in Fig. 4.4 we present the evolutionary tracks of the shocked gas with $x_{\mathrm{e},0} = 10^{-2}$ for different initial temperatures (solid lines) and the bifurcation boundary of the SMS-forming initial condition (right dashed line). While the gas passes through the hatched region where $t_{\mathrm{rec}} > t_{\mathrm{cool}}$, the ionization degree and thus H_2 fraction fall rapidly. If such a gas runs out of H_2 before reaching the region where $t_{\mathrm{cool}} < t_{\mathrm{rec}}$, the condition for fragmentation $t_{\mathrm{cool}} \gtrsim t_{\mathrm{ff}}$ is immediately satisfied and the clouds formed in this way collapse isothermally thereafter (the solid

---

[*] Only with high $x_{\mathrm{e}} \sim 10^{-1}$, the charge exchange reaction ($\mathrm{H}_2 + \mathrm{H}^+ \rightarrow \mathrm{H}_2{}^+ + \mathrm{H}$) becomes the main dissociation reaction of H_2 at $\lesssim 10^3$ cm^{-3}. However, since the bifurcation boundary for $x_{\mathrm{e},0} = 10^{-1}$ locates at higher density ($\gtrsim 10^4$ cm^{-3}), the charge exchange reaction does not have any influences on the location of the boundary. Thus, we adopt equation (4.10) even for $x_{\mathrm{e}} \sim 10^{-1}$.

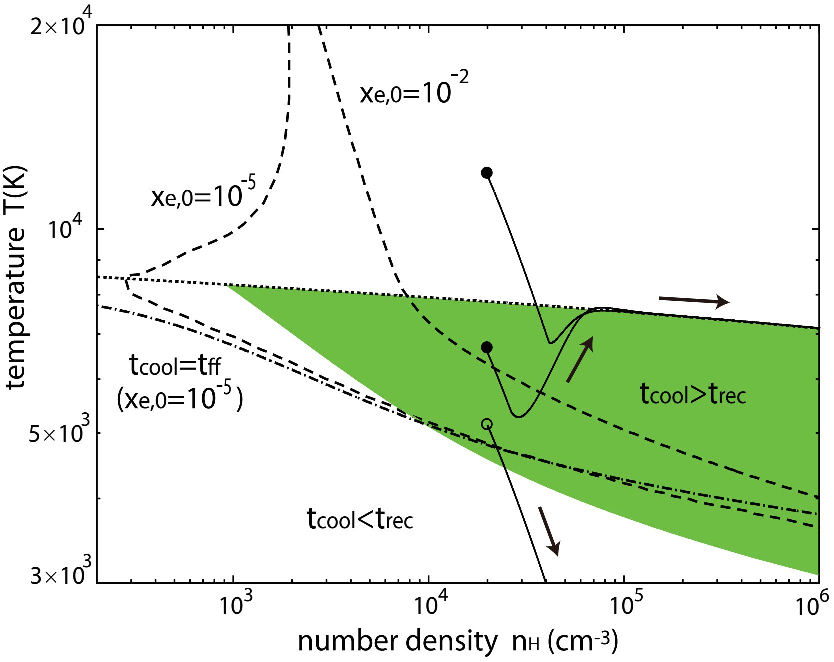

Figure 4.4: The diagram showing relevant processes in setting the bifurcation of the thermal evolution of the shocked gas. The solid lines show the evolutionary tracks of the shocked gas with $x_{\rm e,0} = 10^{-2}$, whose post-shock conditions are $n_{\rm H,0} = 2 \times 10^4$ $\rm cm^{-3}$ and $T_0 = 1.2 \times 10^4$, 6.6×10^3, and 5.1×10^3 K, respectively. Two dashed lines present the bifurcation boundaries of the SMS-forming initial conditions for $x_{\rm e,0} = 10^{-2}$ and 10^{-5}, respectively. The dotted line is the same as the upper thin line in Fig. 4.1, which corresponds to the cut-off temperature below which the H_2 line-emission becomes the main cooling process instead of the Lyα emission. In the hatched region, the ionization degree rapidly falls by effective recombination within the cooling time of H_2 ($t_{\rm cool} > t_{\rm rec}$). The dot-dashed line presents the condition of $t_{\rm ff} = t_{\rm cool}$ for $x_{\rm e} = 10^{-5}$. Here, the cooling time $t_{\rm cool}$ is evaluated by using equation (4.10). This figures is taken from Inayoshi and Omukai (2012).

lines starting from the filled circles in Fig.4.4). However, there is a small margin of the initial parameter range above the line $t_{\rm cool} = t_{\rm rec}$ from which the gas manages to maintain a small fraction of H_2 and can reach the region where $t_{\rm cool} < t_{\rm rec}$. In this case, the post-shock layer can continue the isobaric contraction until ~ 100 K (the solid line starting from the open circle in Fig.4.4). In summary, if the fragmentation condition $t_{\rm cool} \gtrsim t_{\rm ff}$ is met in the range where $t_{\rm rec} < t_{\rm cool}$, the post-shock layer cannot cool further and clouds formed at this moment begin the isothermal collapse. The set of initial conditions from which the evolutionary tracks meet the condition $t_{\rm ff} = t_{\rm cool}$ just on the line $t_{\rm rec} = t_{\rm cool}$ corresponds to the boundary for the SMS formation in Fig. 4.1 in the high density regime (i.e., equation 4.7). Note that the boundary given by equation (4.7) reflects the density-temperature relation of $t_{\rm rec} = t_{\rm cool}$, which is mainly determined by the temperature dependence of $k_{\rm cd}$. Due to the strong dependence of $k_{\rm cd}$ on temperature, the $\rm H_2$ is collisionally dissociated very efficiently for the temperature higher than given by equation (4.7). On the other hand, if the density is lower than the $\rm H_2$ critical density $n_{\rm H,cr}$ ($\sim 10^4\ {\rm cm}^{-3}$) after cooling isobarically to 8000 K, the gas continues further isobaric contraction to several 100 K by the ineffective collisional dissociation of $\rm H_2$. This explains the fact that the low-density side of the boundary of SMS-forming parameters in Fig. 4.1 (i.e., equation 4.6) corresponds to the isobaric contraction track whose density at $\simeq 8000$ K is $\sim 10^4\ {\rm cm}^{-3}$.

Next, we consider the low ionization cases with $x_{\rm e,0} \lesssim 10^{-4}$. As seen in Fig. 4.4, the portion of the bifurcation boundary (left solid line) for $x_{\rm e,0} = 10^{-5}$ locates in the region $t_{\rm rec} > t_{\rm cool}$, where $x_{\rm e}$ is frozen during the isobaric compression. Therefore, if the cooling condition $t_{\rm cool} < t_{\rm ff}$ is initially satisfied in the post-shock layer, the gas continues to cool isobarically until $\lesssim 100$ K, where it produces $\sim 10\ M_{\odot}$ fragments. Thus, the boundary of the SMS-forming condition is simply given by the requirement $t_{\rm ff} \lesssim t_{\rm cool}$ for their initial values without the need for considering the recombination effect. The dot-dashed line in Fig. 4.4 presents the condition $t_{\rm ff} = t_{\rm cool}$ for $x_{\rm e} = 10^{-5}$ and in fact coincides with the boundary on the low-temperature side ($\lesssim 8000$ K).

4.4 Conclusion and Discussion

In this chapter, we have proposed a new scenario for supermassive star (SMS) formation in central hot and dense regions of the halos formed by the cold accretion shocks in the first galaxy formation. Since the gas cools effectively by Lyα emission in halos with virial temperature $T_{\rm vir} \gtrsim 10^4$ K, location of the accretion shock does not stay at the virial radius and shrinks inward. The gas instead flows supersonically along cold and dense filaments to the central region of the first galaxy, where the flows collide each other to produce a hot ($\gtrsim 10^4$ K) and dense ($\gtrsim 10^3\ {\rm cm}^{-3}$) material by a shock (Birnboim and Dekel 2003; Kereš et al. 2005; Dekel and Birnboim 2006; Wise and Abel 2007; Greif et al. 2008; Wise et al. 2008; Dekel et al. 2009; Bromm and Yoshida 2011). We have calculated thermal evolution in such a hot and dense region formed by the cold accretion shock. For $\gtrsim 8000$ K, the efficient Lyα cooling allows the post-shock gas to cool and to contract isobarically at the value of ram pressure from the shock front. To continue the isobaric cooling also below 8000 K, abundant $\rm H_2$ needs to be formed and its cooling must be effective. If the density at $\simeq 8000$ K is high enough ($\gtrsim 10^4\ {\rm cm}^{-3}$) to make the $\rm H_2$ rovibrational levels to reach the local thermodynamic equilibrium, the $\rm H_2$ is dissociated effectively by the collisional reaction from excited levels, which suppresses the cooling to lower temperature by $\rm H_2$. At this epoch, gravitational instability of the post-shock layer produces massive fragments with $\gtrsim 10^5\ M_{\odot}$, which subsequently collapse isothermally at ~ 8000 K by the Lyα cooling. We have studied thermal evolution of the post-shock gas for a wide range of initial conditions (10^2 cm^{-3} $< n_{\rm H,0} <$ 10^7 cm^{-3} and 3000 K$< T_0 <$ 10^5 K) and have pinned down the conditions leading to the isothermal collapse (the hatched region in Fig. 4.1): $T_0 \gtrsim 6000$ $(n_{\rm H,0}/10^4$ cm$^{-3})^{-1}$ K for $n_{\rm H,0} \lesssim 10^4$ cm^{-3} and $T_0 \gtrsim 5000 - 6000$ K for $n_{\rm H,0} \gtrsim 10^4$ cm^{-3}, for the pre-shock ionization degree at $x_{\rm e,0} = 10^{-2}$. Since $\rm H_2$ is formed by the electron-catalyzed reactions, the above condition depends somewhat on the initial ionization degree (see Fig. 4.2): for smaller $x_{\rm e,0}$, the domain of initial conditions leading to the isothermal collapse extends towards lower density. Those massive clouds continue isothermal collapse until very high density $\sim 10^{16}$ cm^{-3}, where they become optically thick to the $\rm H^-$ bound-free absorption (Omukai 2001). The clouds are supposed to collapse directly to SMSs without further fragmentation (e.g., Bromm and Loeb 2003; Regan and Haehnelt 2009a,b; Shang et al. 2010). Eventually, the SMSs collapse by the post-Newtonian instability, swallowing most of their material, to become seeds of SMBHs (Shibata and Shapiro 2002).

The first galaxies may be enriched with metals to some extent as well as dusts dispersed by supernova (SN) explosions of previous generations of stars. With high enough metallicity, the gas can cool to low temperature (~ 100 K) by metal-line cooling alone even without $\rm H_2$. In this case, the SMS formation would be strongly suppressed. We have then repeated the same analysis by considering as well as the metal cooling by $\rm C_{II}$ and $\rm O_I$. We have found that as long as the metallicity is lower than $Z_{\rm cr} \simeq 10^{-3}\ Z_\odot$, the metal-line cooling does not change the condition for SMS formation from that in the primordial case (see Fig. 4.3). According to some cosmological simulations of the assembly of first galaxies (Greif et al. 2010; Wise et al. 2012), the dense gas at the center of galaxies is uniformly enriched to $\sim 10^{-3}\ Z_\odot$ by a pair instability SN of massive population III stars with $140\ M_\odot \lesssim {\rm M} \lesssim 260\ M_\odot$. On the other hand, typical population III stars are recently considered to be less massive $\sim 40\ M_\odot$ (Hosokawa et al. 2011; Stacy et al. 2012) and end their lives as ordinary core collapse SNe. In this case, the resultant metallicity reduces by a factor of $\sim$10 (Heger and Woosley 2002; Nomoto et al. 2006) and thus becomes lower than the critical metallicity for SMS formation we estimated.

We here stress that our scenario naturally explains the formation of seed BHs in the conditions of first-galaxy formation without invoking extremely strong UV radiation as envisaged in the previous scenario. The necessary condition for SMS formation in halos with $T_{\rm vir} \gtrsim 10^4$ K is the isothermal collapse by the atomic cooling as a result of suppression of the $\rm H_2$ cooling in the entire density range. So far, as a mechanism to suppress $\rm H_2$ cooling, photodissociation by FUV radiation has been considered. In this scenario, however, extremely strong FUV intensity $J_{21}^{\rm LW} \gtrsim 10^2 - 10^3$ (in unit of 10^{-21} erg s^{-1} cm^{-2} Hz^{-1} sr^{-1}) is required to quench the $\rm H_2$ cooling (Omukai 2001; Bromm and Loeb 2003; Shang et al. 2010), and halos irradiated by such intense radiation are extremely rare ($\lesssim 10^{-6}$ at $z \sim 10$; Dijkstra et al. 2008). Moreover, if external ionization by cosmic rays or X-rays, which promotes the $\rm H_2$ formation, is present as well, the FUV intensity needed for SMBH formation is elevated. There would be little possibility

($\ll 10^{-6}$) for such an intense FUV field to be realized in any haloes and thus the SMS formation could strongly suppressed (Inayoshi and Omukai 2011). On the other hand, in our scenario, collisional dissociation, rather than photodissociation, suppresses the H_2 cooling. Thus, even without FUV radiation, which has been considered to be indispensable previously, the isothermal collapse and thus SMS formation can be realized as long as the right condition is met for the cold accretion shock. Note, however, this mechanism for SMS formation cannot operate in all first galaxies since SMBHs are rare objects. If we use the number density of halos with mass $\sim 10^8\ M_\odot$ at $z \sim 10$, ~ 10 Mpc^{-3} (comoving) and assume each of them had a SMS of $\sim 10^5\ M_\odot$, the predicted mass density of SMBHs $\sim 10^6\ M_\odot$ Mpc^{-3} (comoving) will exceed the total present-day BH mass density $\sim 3 \times 10^5\ M_\odot$ Mpc^{-3} estimated by Yu and Tremaine (2002). Therefore, our conditions for SMS formation would be satisfied only in a small fraction of first galaxies or some other processes, e.g., turbulent fragmentation, lack of accreting material etc., suppress this mechanism to work for avoiding overproduction of BHs.

We here briefly discuss the effect of dust cooling, which has not been considered in this chapter. If the depletion factor of metals to dust grains is as high as the present-day Galactic value $f_{\rm dep} \simeq 0.5$, the thermal evolution deviates from the isothermal one at $\gtrsim 10^{10}$ cm^{-3} due to the dust cooling, if metallicity is higher than $Z_{\rm cr,dust} \simeq 10^{-5}\ Z_\odot$ (Omukai et al. 2008). Although this critical metallicity $Z_{\rm cr,dust}$ is smaller than the critical value due to metal-line cooling $Z_{\rm cr} \simeq 10^{-3}\ Z_\odot$ by two orders of magnitude, the depletion factor in the first-galaxy forming environment is highly uncertain. According to theoretical models of dust formation and destruction in the first SNe, typically only a few % of dust formed at the explosion survives, after being swept by the reverse shock, depending on the ambient density (Nozawa et al. 2006; Bianchi and Schneider 2007). For example, with $f_{\rm dep} \simeq 0.05$, the critical metallicity becomes $Z_{\rm cr,dust} \simeq 10^{-4}\ Z_\odot$, which makes the constraint on metal pollution less severe. In any case, to predict whether the isothermal collapse continues in spite of metal enrichment, we need more accurate knowledge of the depletion factor $f_{\rm dep}$.

In this chapter, we consider the hot and dense central regions owing to shocks by the cold accretion flows in the forming first galaxies. Likewise, a galaxy merging event drives inflows, creating a similar environment around the galaxy center (e.g., Mayer et al. 2010). If the shocked region satisfies our post-shock criterion for the H_2 collisional dissociation, the SMS formation is expected also in this case. In merging galaxies, however, star formation and also metal enrichment are expected to have already proceeded significantly. Therefore, in the case of the inflows by galaxy merger, SMS formation is probably prohibited by the metal-cooling effect. The cold accretion shocks in the first galaxy formation would provide more easily the suitable conditions for SMS formation. Recently, assuming seed BHs with $\sim 10^5\ M_\odot$, Di Matteo et al. (2012) and Khandai et al. (2012) discussed their growth by the cold accretion flows in the process of the first galaxy formation. Their results demonstrate that the cold flows are less susceptible to feedbacks from the growing BHs and high accretion rate is maintained until mass of the galaxy reaches $\gtrsim 10^{12}\ M_\odot$, where the cold mode of accretion turns the usual hot virialization mode. As a result, the BH is able to grow to $\gtrsim 10^9\ M_\odot$ by $z \sim 6$. Our scenario for the SMS formation provides a mechanism for seeding BHs of $\sim 10^5\ M_\odot$ in forming galaxies, which has been assumed in studies of Di Matteo et al. (2012) and Khandai et al. (2012), while their results complementary demonstrated those seed BHs can in fact grow to SMBHs.

Finally, we remark remaining issues to be explored. In our scenario, the physical condition in the post-shock gas (especially, its density) is crucial for the SMS formation. We have considered a range of density ($10^2 - 10^7 \mathrm{cm}^{-3}$) and temperature ($3000 - 10^5$ K) as the post-shock conditions. Currently, we only know the typical values of those parameters (Greif et al. 2008; Wise et al. 2008), but are still lacking knowledge of the relationship between the post-shock conditions and formation conditions (i.e., mass, virialization epoch, etc.) of first galaxies. In addition, our assumption that the enough mass supply for Jeans instability is available through the streaming flow is need further investigation. Safranek-Shrader et al. (2010) evaluated the amount of accreted gas to be $\sim 10^5\ M_\odot$, which is inhomogeneously organized by turbulence (e.g., Wise and Abel 2007; Greif et al. 2008). Therefore, the outcome of the shocked material in most of halos could be numerous small sub-regions, rather than a massive layer envisaged in this chapter. On the other hand, even if the turbulent motion dominates, a gravitational unstable cloud with $\sim 10^5\ M_\odot$ could form in the center and collapse subsequently (Wise et al. 2008). As a future project, we need to study in what halos the SMS forming conditions are satisfied by way of realistic cosmological simulations, including e.g., molecular cooling and the radiative and chemical feedbacks, for evaluating more quantitatively the feasibility of SMS formation in the first galaxies.

In this chapter, we have supposed that, for the SMS formation, massive clouds must collapse isothermally without fragmentation. In fact, three-dimensional hydrodynamical simulations by Bromm and Loeb (2003) confirmed in some cases that the cloud collapsing isothermally by the atomic cooling does not experience fragmentation at least in the range $\lesssim 10^9\ \mathrm{cm}^{-3}$ and, consequently, a supermassive clump forms at the center. Even with some angular momentum, fragmentation resulted at most in a binary system in their calculation. However, depending on such initial conditions as degrees of rotation or turbulence, the clouds would fragment into less massive clumps during the isothermal collapse. As a future study, it is awaited to clarify the conditions under which the clouds elude fragmentation by way of three-dimensional hydrodynamical calculation.

Chapter 5

Formation of supermassive stars via direct collapse

As seen in the previous chapters, a supermassive cloud without H_2 molecules collapses almost isothermally (~ 8000 K) by the H atomic cooling (e.g., Lyα emissions) and continuum cooling (Omukai 2001). Some three-dimensional simulations (Bromm and Loeb 2003; Wise et al. 2008) suggest that the cloud can avoid efficient fragmentation and continues to collapse monotonically until the protostar forms at the center. After the protostellar formation, the protostar rapidly grows via accretion from the hot envelope at $\dot{M}_{\rm acc} \gtrsim 0.1\ M_{\odot}\ {\rm yr}^{-1}$. Under such high accretion rate, the protostar evolves stably without experiencing the radiative feedback (Hosokawa et al. 2012a) and mass-loss driven by the stellar pulsations (Inayoshi et al. 2013).

We here perform the three-dimensional hydrodynamical simulations for the collapse of a supermassive cloud until a protostar forms at the center. Most previous simulations [*] assume that the Lyα cooling is optically thin and the H_2 cooling never works during the collapse. However, the Lyα emissions becomes optically thick and the continuum radiative cooling instead dominates at high density regime ($> 10^6\ {\rm cm}^{-3}$). Therefore, the resultant gas temperature decreases compared to the previous ones. Furthermore, the H_2 fraction rapidly increases through three-body reactions at $n > 10^{10}\ {\rm cm}^{-3}$. Then, the H_2 cooling can be effective and rapidly decrease the gas temperature (i.e., *thermal instability*) if the turbulent motions delay the gravitational collapse. When the thermal instability is driven, the supermassive cloud could strongly fragments into many clumps with a small jeans mass ($\sim$ a few $M_{\odot}$) instead of forming a supermassive star. Therefore, we here investigate the fate of a supermassive cloud with turbulent motions considering the continuum and H_2 line cooling and non-equilibrium chemical networks consistently.

---

[*] Shang et al. (2010) considers the H_2 line cooling in the collapse stage at low density regime $< 10^{10}$ ${\rm cm}^{-3}$.

5.1 Methods

We perform the three-dimensional hydrodynamical simulations of a collapse of a supermassive cloud using a public code Enzo, which is an Eulerian adaptive mesh refinement (AMR) code (The Enzo Collaboration et al. 2013). The basic equations are given by

$$\frac{\partial \rho}{\partial t} + \nabla \cdot (\rho \mathbf{v}) = \mathbf{0}, \tag{5.1}$$

$$\frac{\partial \rho \mathbf{v}}{\partial t} + \nabla \cdot (\rho \mathbf{v}\mathbf{v} + p\mathbf{I}) = -\rho \nabla \phi, \tag{5.2}$$

$$\frac{\partial E}{\partial t} + \nabla \cdot [(E + p)\,\mathbf{v}] = -\rho \mathbf{v} \cdot \nabla \phi - \Lambda + \Gamma, \tag{5.3}$$

and

$$\frac{\partial n_i}{\partial t} + \nabla \cdot (n_i \mathbf{v}) = \sum_j k_{ij} n_i n_j + \sum_{jl} k_{ijl} n_i n_j n_l + \cdots, \tag{5.4}$$

where ρ, $\mathbf{v}$, E, p, ϕ are the gas density, velocity, total fluid energy, pressure, and gravitational potential. Λ and Γ are the cooling/heating rate (in unit of erg s^{-1} cm^{-3}), respectively. The chemical abundance of i-th species n_i evolves following the rate equation, where k_{ij} (k_{ijl}) is the reaction rate coefficient of the two (three)-body reaction including the creation and dissociation of i-th species.

Our main aim is to investigate of the gas dynamics over the wide range of the density ($10^{-21} \lesssim \rho \lesssim 10^{-6}$ g cm^{-3}). As the initial condition of the cloud, we use the spherical density profile increased by a factor f ($= 1.6$) from the critical Bonnor-Ebert (BE) sphere, which is the isothermal sphere with hydrostatic equilibrium supported by the external pressure. For the critical BE sphere, the central density is $n_c = 10^4$ cm^{-3}, the temperature $T = 10^4$ K, and the radius is $R_c = 6.46 c_s (4\pi G \rho_c)^{-1/2} = 10.8$ pc, where c_s is the isothermal speed of sound, G the gravitational constant, ρ_c the central mass density. The total mass of the cloud is $M = f M_{\mathrm{BE}} = 1.17 \times 10^5$ $M_{\odot}$. Then, we set a simulation box with $(50\ \mathrm{pc})^3$ and the maximum refinement level to 23 (the maximum spatial resolution is $\lesssim 0.1$ AU). In order to prevent the artificial fragmentation, we impose the refinement criterion that one jeans length is resolved by at least 16 grids (Truelove et al. 1997).

Furthermore, some simulations for the first galaxy formation (e.g., Wise and Abel 2007; Greif et al. 2008) suggest highly turbulent gas could develops at the central region during the structure formation. To consider the density and velocity perturbations due to turbulent motions, we initially impose a subsonic velocity field ($v_{\mathrm{rms}} = 0.1\ c_s$) with power spectrum $P(k) \propto k^{-4}$, which corresponds to the expected spectrum for giant molecular clouds (Larson 1981; Mac Low 1999). To ensure the turbulence modes were adequately resolved, we selected a maximum k-mode value of 1/10th of the number of cells across the cloud.

To investigate the SMS formation, the chemical networks and cooling/heating in the gas are the most important processes. We must treat the non-equilibrium primordial chemistry including 6 species (H, H_2, e, H^+, H_2^+, and H^-) and 14 reactions required to estimate the cooling/ heating rate on the atomic cooling path. Our main aim is to follow the evolution of a supermassive cloud until the protostars are formed. So, we need solve the chemical networks at high density enough to reach the chemical equilibrium. We here use the "piecewise exact solution method" to simulate the chemical evolution stably (Inoue and Inutsuka 2008) instead of the original Enzo solver, so-called the differential backward method (red). Moreover, we consider all radiative cooling processes to follow the thermal evolution: atomic cooling (Lyα, two photon emissions, H^- free-bound, and free-free emissions; Omukai 2001) and H_2 cooling (line and collision-induced emissions). To study the formed protostars, we evaluate the suppression of the cooling rate estimating the optical depth ($= \rho \kappa_R L$) consistently with the chemical evolution, where κ_R is the Rosseland mean opacity (H_2 rayleigh scattering, H_2 collision-induced absorption, and the self-absorption of the H^- free-free emissions) and L the local jeans length.

5.2 Results

5.2.1 thermal and chemical evolution

Figure 5.1 and 5.1 show the temperature and H_2 fraction of a collapsing supermassive cloud as a function of the gas density just after a protostar forms at the center. Since the center of the cloud collapses runaway and the density profile follows the self-similar solution (e.g., Penston 1969; Larson 1969), this diagram also roughly means the thermal evolution of the central region.

Figure 5.1 shows that the collapsing gas has two thermal phase. First, we discuss the hot component, which finally becomes a protostar. The hot component collapses almost isothermally until $\rho \sim 10^{-7}$ g cm^{-3} keeping the temperature $3000 < T < 8000$ K. At low density regime ($\rho < 10^{-16}$ g cm^{-3}), the main coolants are the Lyα (2p → 1s) and two photon (2s → 1s) emissions. At high density regime ($\rho > 10^{-16}$ g cm^{-3}), the dominant cooling shifts to the H^- bound-free emission ($H + e \rightarrow H^- + \gamma$). When the cloud collapse until $\rho > 10^{-9}$ cm^{-3}, the H^- free-bound emissions are self-absorbed and scattered by the H_2 molecules (Rayleigh scattering). After that, the cloud cools until $\rho \gtrsim 10^{-8}$ g cm^{-3} by the H^- free-free emissions ($H + e \rightarrow H + e + \gamma$). Finally, all continuum cooling processes become optically thick and a hydrostatic core (i.e., protostar) is formed at the central region. The gas is heated up through the accretion shock and the temperature increases adiabatically in the protostar.

Next, figure 5.2 presents the H_2 fraction as a function of the gas density. The H_2 fraction initially decreases and approaches the equilibrium value ($\sim 10^{-8}$) between the formation through H^- ion ($H^- + H \rightarrow H_2 + H$) and the collisional dissociation ($H_2 + H \rightarrow 3H$). Here, we do not consider the H_2 photodissociation by FUV radiations, which is required to suppress the H_2 cooling. However, even for strong FUV radiation ($J_{21} \gtrsim 10^3$), the self-shielding effect becomes effective at the H_2 column density higher

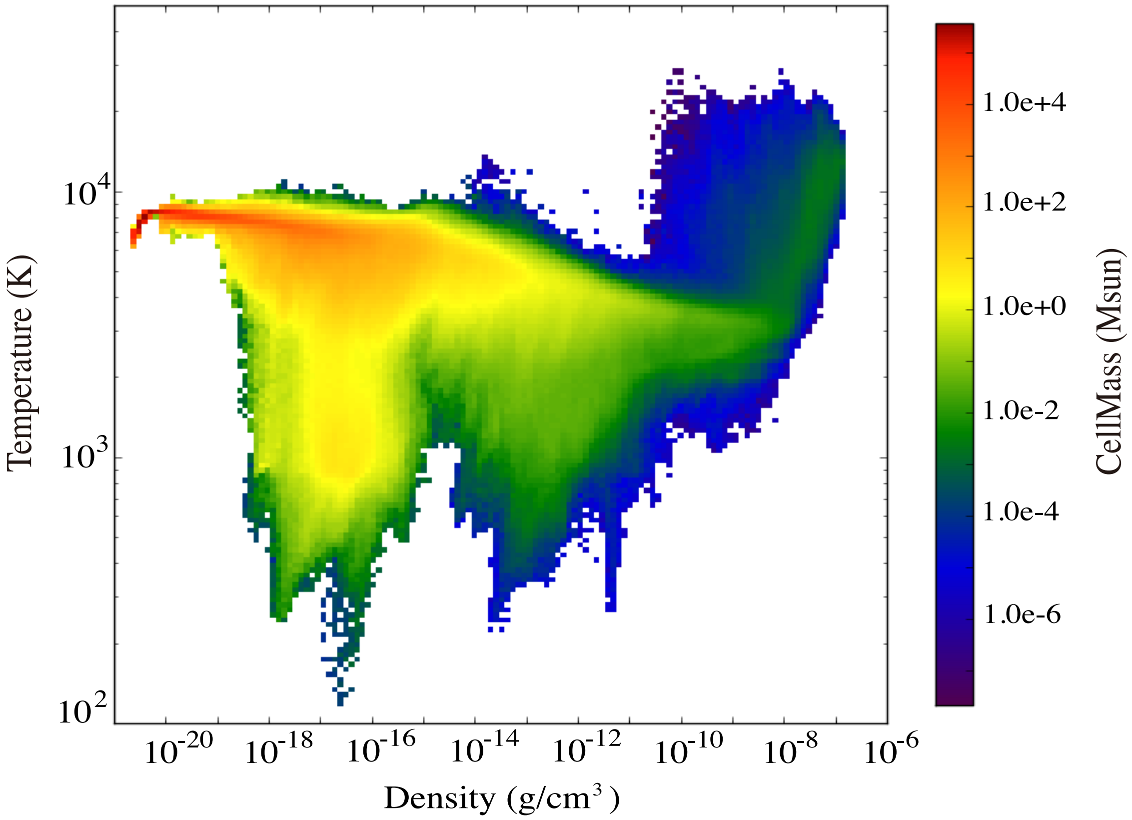

Figure 5.1: Density-temperature diagram of a collapsing supermassive cloud just after a protostar forms at the center. The color bar indicates the sum of the cell mass for the grids. The gas has two thermal phase: (1) hot component which collapses and form a protostar and (2) cold component which appears owing to the thermal instability.

than 10^{22} cm^{-2} ($\rho \gtrsim 10^{-20}$ g cm^{-3}), where the collisional dissociation dominates instead of the photo-dissociation. At high density regime ($\rho > 10^{-13}$ g cm^{-3}), the three-body reaction ($3\mathrm{H} \rightarrow \mathrm{H}_2 + \mathrm{H}$) rapidly enhances the H_2 fraction. The central region of the cloud approaches a full H_2 molecules, but both the H_2 line and CIE cooling never play a significant role for the thermal evolution at $\rho \gtrsim 10^{-8}$ g cm^{-3}. The interior of the protostar is so hot that the H_2 molecules are strongly dissociated.

On the other hand, some cold components exist at the density region lower than 10^{-10} g cm^{-3}. This component appears because of the adiabatic cooling induced by the turbulent expansion and H_2 molecular cooling. Once the gas temperature decreases by the adiabatic cooling, the dissociation of H_2 molecules becomes inefficient, which promotes the H_2 formation (H^- process and three-body reaction) and its line cooling. This abrupt cooling proceeds with the temperature decreasing, which is a kind of the thermal instability associated with the chemical reactions. Since the cold component

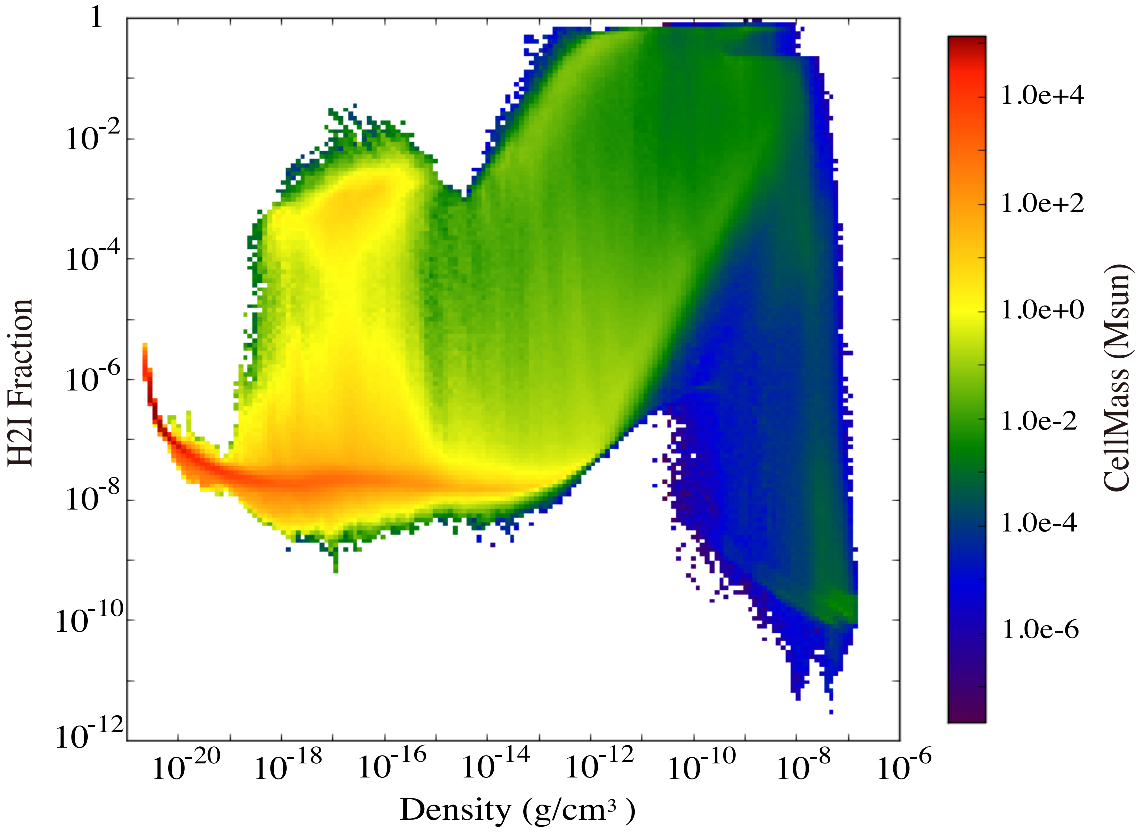

Figure 5.2: Density-H_2 fraction diagram of a collapsing supermassive cloud just after a protostar forms at the center. In the cold parts, the H_2 fraction increases to $\gtrsim 10^{-2}$. The color bar indicates the sum of the cell mass for the grids.

is so less massive that the gas does not collapse until higher density and have any influences on the evolution of the central collapsing region.

5.2.2 Hydrodynamics

Figure 5.3 and 5.4 show the slice plots of the density and temperature distribution at the end of this simulation. The density distributions are shown within the box of $L = 2$ pc and 0.2 pc for the $z = 0$ plane, respectively. See from Figure 5.3, the central region of the cloud collapses runaway to higher density. Owing to turbulent motions, the filamentary structures are formed and accrete on to the center. Similar structures continue to be formed within 0.05 pc. The temperature distribution are presented within the box of $L = 1$ pc for the $x = 0$ (left) and $z = 0$ (right) plane, respectively. This figure shows that the gas cloud is divided into the hot and cold components (see Figure 5.1). Most of the gas are hot keeping $T \sim 8000$ K, which have the complex structures associated with the gas filaments. The cold gas are mainly formed outside

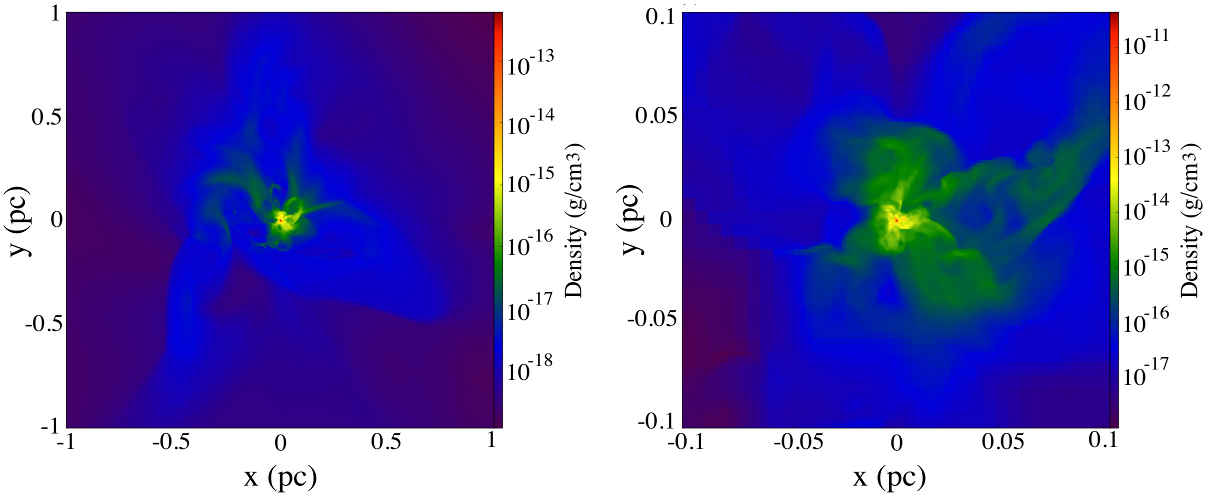

Figure 5.3: Slice plot of the density distribution ($z = 0$) of the collapsing cloud at the large scale: (left panel) $L = 2$ pc and (right panel) $L = 0.2$ pc, respectively.

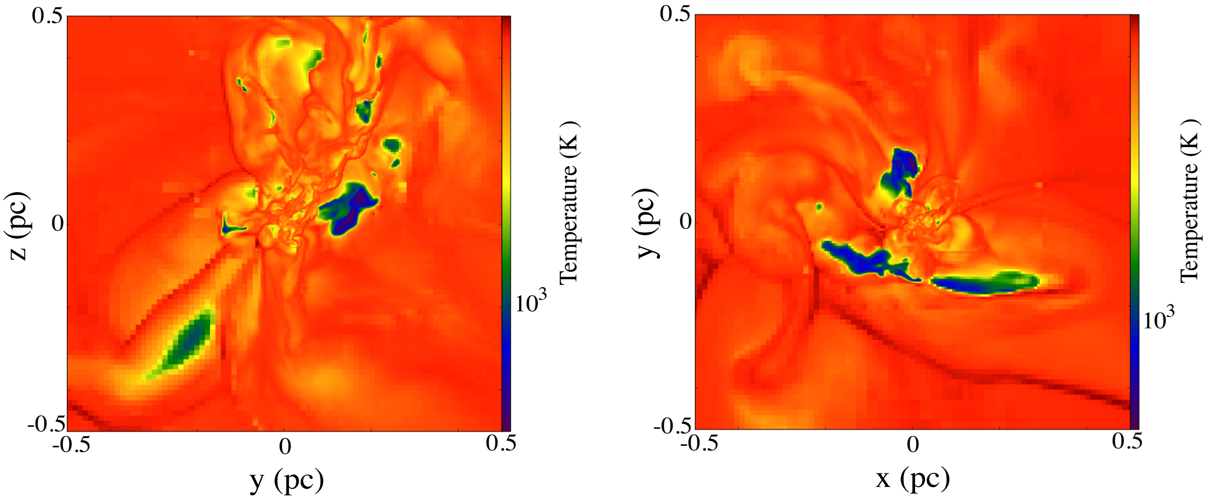

Figure 5.4: Slice plot of the temperature distribution of the collapsing cloud at the large scale ($L = 1$ pc): (left panel) $x = 0$ and (right panel) $z = 0$ plane, respectively.

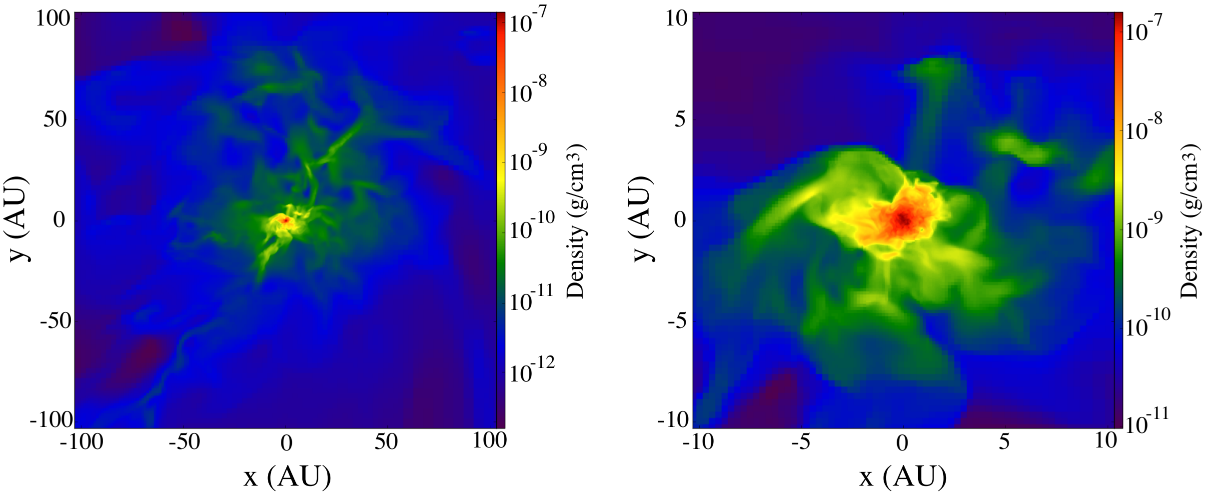

Figure 5.5: Slice plot of the density distribution ($z = 0$) of the collapsing cloud at the large scale: (left panel) $L = 200$ AU and (right panel) $L = 20$ AU, respectively.

the central collapsing region ($\gtrsim$ 0.1 pc) and the typical size is as large as $\sim$ 0.1 pc. These cold clumps are expected to fall on to the central protostar.

Figure 5.5 shows the density distribution at the central region within 100 AU and 10 AU, respectively. The filamentary gas inflows hierarchically continue to the central protostar ($\rho \sim 10^{-8}$ g cm^{-3}), and rapidly feed the protostar. Right panel shows the density distribution of the central protostar. The yellow contour roughly presents the radius of the hydrostatic core (i.e., protostellar radius). The radius is as large as $\sim$ 2 AU, which is well resolved in this simulation. In this simulation, the protostar grows via accretion to $\sim 3\ M_{\odot}$.

Figure 5.6 presents the profile of the accretion rate defined by $\dot{M}_{\rm acc} = -4\pi\rho r^2 v_{\rm rad}$ for each epoch, where $v_{\rm rad}$ is the radial velocity. The dashed lines show the parts where $v_{\rm rad} > 0$ (i.e., expansion). When the protostar is formed (green and red lines), the radial velocity rapidly decreases at $\sim$ 1 AU because of the accretion shock. Typical accretion rate is as high as $\sim 3\ M_{\odot}\ {\rm yr}^{-1}$, which is somewhat higher than that of the self-similar solution $\sim$ a few $\times\ 10^{-1}\ M_{\odot}$. The protostar is expected to grow via such rapid accretion up to a supermassive star with $\gtrsim 10^5\ M_{\odot}$ within its lifetime. In this result, when the protostellar grows rapidly and its mass reaches a few $\times\ M_{\odot}$, its radius is as large as $\sim$ 2 AU. This value is consistent with that obtained by the calculations of the stellar-structure evolution (Hosokawa et al. 2012), which is obtained under the assumption of the spherical accretion.

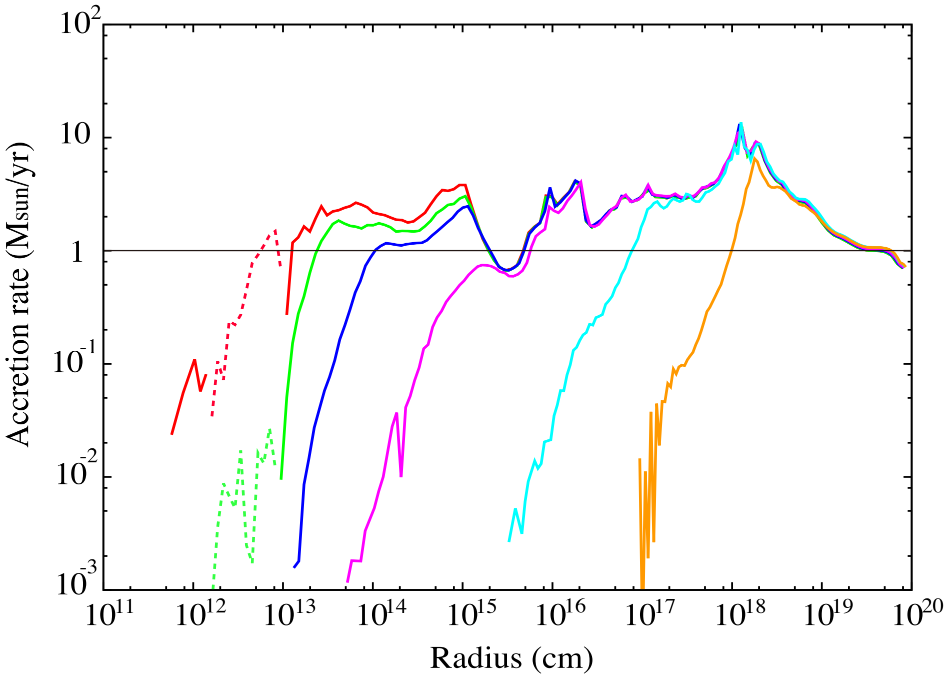

Figure 5.6: The profile of the accretion rate ($\dot{M}_{\rm acc} = -4\pi\rho r^2 v_{\rm rad}$) for each epoch. The dashed lines show the parts where $v_{\rm rad} > 0$ (i.e., expansion). For comparison, the horizontal line ($\dot{M}_{\rm acc} = 1.0\ M_\odot\ {\rm yr}^{-1}$) is shown.

5.3 Conclusion and Discussion

We perform the numerical simulation of a supermassive cloud with mass of $\gtrsim 10^5\ M_\odot$. To investigate the hydrodynamical and thermal evolution over the wide spacial range, we use an Eulerian adaptive mesh refinement (AMR) code. The most crucial problem for the supermassive star formation is whether the cloud fragments into many clumps or not. The efficiency of the fragmentation is determined by the thermal state (i.e., equation of state). Although the thermal state strongly depends on the radiative cooling processes, the previous studies have considered only the most simple cooling (Lyα emission). So, we here consider all processes necessary to study the evolution of a supermassive cloud. Among them, the H_2 line cooling is the most significant because its cooling could promote the thermal instability and efficient fragmentation. Moreover, recent numerical simulations suggest that the gas is highly turbulent in the galaxy formation. We here consider that the density perturbations due to the turbulence following the power spectrum $P(k) \propto k^{-4}$, which is the spectrum well-known form the observations of the interstellar medium.

Even in cases with turbulence, a supermassive cloud can collapse runaway almost following the self-similar density profile ($\rho \propto r^{-2}$) without efficient fragmentation. When the density increases to $> 10^{-13}$ g cm^{-3}, the H_2 fractions are rapidly enhanced by the three-body reaction ($3H \rightarrow H_2 + H$). Then, the central region of the cloud approaches a full H_2 molecules, but the H_2 cooling (both of line and continuum emission) never play a significant role for the thermal evolution at such dense region. Finally, just when the all radiative cooling becomes optically thick ($\rho \gtrsim 10^{-7}$ g cm^{-3}), a hydrostatic core (i.e., protostar) is formed. On the other hand, many cold clumps are formed surrounding the central protostar (low density regime) by the thermal instability due to efficient H_2 line cooling.

The formed protostar grows via rapid accretion fed the dense filamentary flows. The accretion rate is so high ($\dot{M}_{\rm acc} \sim 3\ M_{\odot}$ yr^{-1}) that the protostar is expected to evolve up to a supermassive star with $\gtrsim 10^5\ M_{\odot}$ within its lifetime. At the end of this simulation, the radius of the protostar is as large as ~ 2 AU, which is well resolved in this simulation, and the mass grows up to $\sim 3\ M_{\odot}$. The properties of the central protostar are consistent with the result of the stellar-structure evolution by Hosokawa et al. (2012), who assumes the spherical accretion.

In this chapter, we discuss the evolution of a supermassive cloud assuming the initial condition as a Bonnor-Ebert sphere with turbulence. Although a protostar forms without efficient fragmentation in our case, there might be the case that gas fragmentation efficiently occurs for other initial conditions. Thus, we need investigate the dependence of the fate of the supermassive cloud on the choices of the initial conditions (e.g., the enhanced factor of the density f, cloud rotation, Mach number of turbulence, and so on). Finally, it is strongly required to conclude whether supermassive stars are formed in the early universe, performing the cosmological simulations, which provide more proper initial condition of the collapsing cloud.

Chapter 6

Pulsational instability of supergiant protostars

This monolithic contraction of the cloud leads to a formation of a small protostar ($\sim 0.01\ M_\odot$) at its center. The embryo protostar subsequently grows to a SMS via rapid accretion of the surrounding envelope. In the H atomic cooling case, the accretion rate onto the protostar is $\sim 0.1\ M_\odot\ \mathrm{yr}^{-1}$. This is due to the high temperature in the atomic cooling cloud ($\simeq 10^4$ K) because the accretion rate is set by the temperature in the star-forming cloud as $\dot{M}_{\mathrm{acc}} \sim 7 \times 10^{-2}\ M_\odot\ \mathrm{yr}^{-1}(T/10^4\ \mathrm{K})^{1.5}$ (e.g., Shu 1977; Stahler et al. 1986). This rapid accretion with $\sim 0.1\ M_\odot\ \mathrm{yr}^{-1}$ drastically changes the protostellar evolution. Figure 6.1 shows the evolution of the radii of accreting protostars at different accretion rates. In the ordinary Pop III protostar case ($\dot{M}_{\mathrm{acc}} \simeq 10^{-3}\ M_\odot\ \mathrm{yr}^{-1}$), after the so-called *adiabatic-accretion phase*, where adiabatic heat input expands the star gradually with mass and the protostar starts to contract by losing its entropy via radiative diffusion (the *Kelvin-Helmholtz contraction*) until the nuclear ignition occurs at the center. The protostar reaches the zero-age main sequence (ZAMS) stage at this point (Stahler et al. 1986; Omukai and Palla 2001, 2003). On the other hand, with the accretion rate as high as $\dot{M}_{\mathrm{acc}} \gtrsim 0.1\ M_\odot\ \mathrm{yr}^{-1}$, the protostar continues expanding without the KH contraction as recently found by Hosokawa et al. (2012a) (hereafter HOY12) (see Figure 6.1). In such a star, while most of the interior material contracts, the outermost layer significantly swells up like a red-giant star ("*supergiant protostar*" phase). This is because the outer layer absorbs a part of the outward heat flux and obtains a very high specific entropy. Also in this case the contraction at the center ceases with the hydrogen ignition, but the envelope continuously expands with the increase of stellar mass.

If rapid accretion at $\dot{M}_{\mathrm{acc}} \gtrsim 0.1\ M_\odot\ \mathrm{yr}^{-1}$ is maintained, the stellar mass exceeds $10^5\ M_\odot$ within its lifetime. Such SMSs are general-relativistically unstable (e.g., Zeldovich and Novikov 1971; Shapiro and Teukolsky 1983) and collapse as a whole to a BH (Shibata and Shapiro 2002), which can be a seed for the SMBHs residing in the early universe ($z \gtrsim 7$). With the stellar mass increasing, however, the stars become more

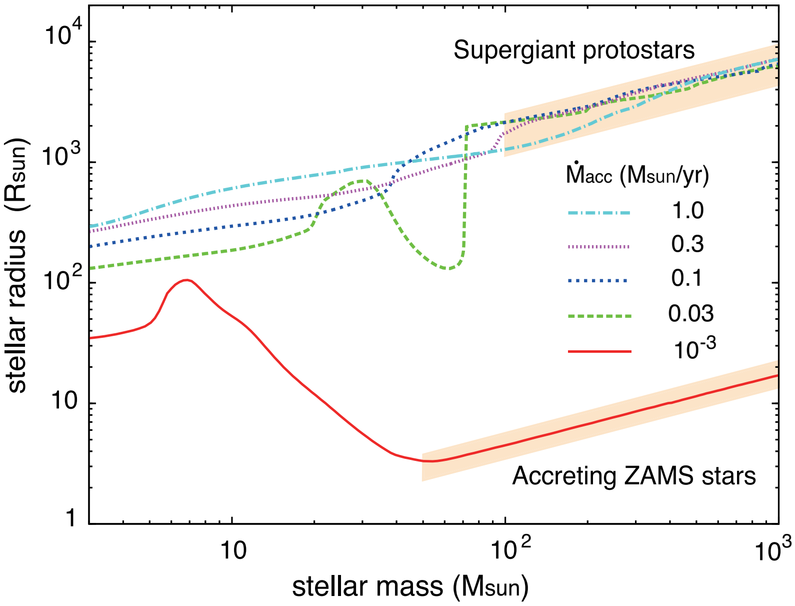

Figure 6.1: Evolution of the protostellar radius with various accretion rates $\dot{M}_{\rm acc} = 10^{-3}$, 0.03, 0.1, 0.3, and 1.0 $M_\odot$ yr^{-1}. In this paper, we analyze the pulsational stability of the stars located in the shaded zones; accreting ZAMS stars for $\dot{M}_{\rm acc} = 10^{-3}$ $M_\odot$ yr^{-1}, and supergiant protostars for $\dot{M}_{\rm acc} > 10^{-3}$ $M_\odot$ yr^{-1}. This figures is taken from Inayoshi et al. (2013).

radiation-pressure dominated and approach a marginally stable state. This may induce pulsational instability of the massive stars and result in mass-loss from the surface. If this mass loss surpasses the accretion onto the star, the stellar growth will be terminated at that point. To see whether the SMS formations are indeed possible in spite of such mass loss, we examine the pulsational stability of the supergiant protostars in this chapter.

Pulsational stability of non-accreting Pop III stars has been studied by Baraffe et al. (2001) and Sonoi and Umeda (2012) in the range 120 $M_\odot \leq M_* \leq 3 \times 10^3$ $M_\odot$. They showed that those stars are unstable against pulsation caused by the nuclear burning (the so-called ϵ mechanism), and that the resulting mass-loss rate is $\dot{M}_{\rm loss} \gtrsim 10^{-5}$ $M_\odot$ yr^{-1}. Gamgami (2007) studied this mass-loss process from the Pop III stars using spherically symmetric hydrodynamical simulations, and showed that pulsation accelerates the surface material to the escape velocity and causes eruptive mass-loss for $M_* \gtrsim 500$ $M_\odot$. On the other hand, the Pop I red-giant stars are known to be pulsationally unstable by the opacity-driven mechanism (the so-called κ mechanism, e.g., Li and Gong 1994; Heger et al. 1997, and the typical mass-loss rate is $\sim 10^{-5}$ $M_\odot$ yr^{-1} (Yoon and Cantiello 2010). With the Pop III composition while having similar structure to the Pop I red-giants, the supergiant protostars can also be pulsationally unstable.

We here study their stability by performing the linear stability analysis for the mass range $M_* \lesssim 10^3\ M_\odot$, which has been calculated by HOY12. By estimating the mass-loss rate, we discuss whether supergiant protostars grow via accretion despite the pulsation-driven mass loss. In section 5.2, we introduce the method for the linear stability analysis against the pulsation and for the estimation of the mass-loss rates for unstable stars. In section 5.3, we present our results and explain how the stability changes with the different stellar masses and accretion rates. Finally, in section 5.4, we summarize our study and present our discussions. In Appendix A, we describe the details (the basic equations and boundary conditions) of the linear stability analysis.

6.1 Stability analysis

We study the pulsational stability of protostars growing at constant accretion rates $\dot{M}_{\rm acc} = 10^{-3}$, 0.03, 0.1, 0.3, and 1.0 $M_\odot\ {\rm yr}^{-1}$, whose structures have been numerically calculated in HOY12. Figure 6.1 presents the evolution of the stellar radii for these rates. We apply the linear stability analysis (see Appendix for the details) to stellar models either in the ZAMS (for $\dot{M}_{\rm acc} = 10^{-3}\ M_\odot\ {\rm yr}^{-1}$) or supergiant protostar (for higher accretion rates), indicated by the shaded areas in Figure 6.1. We consider the perturbations proportional to $e^{i\sigma t}$, where $\sigma = \sigma_{\rm R} + i\sigma_{\rm I}$ is the eigen frequency, $\sigma_{\rm R}$ the frequency of the pulsation, and $|\sigma_{\rm I}|$ the growing or damping rate of the pulsation depending on its sign; the stars are stable (respectively unstable) if $\sigma_{\rm I} > 0$ (respectively $\sigma_{\rm I} < 0$). According to previous studies, massive main-sequence Pop III stars are unstable only under the radial perturbations (Baraffe et al. 2001; Sonoi and Umeda 2012). We thus consider only the radial mode, hereafter, at which the supergiant protostars are also expected to be the most unstable.

A useful quantity in the stability diagnosis is the work integral W (Cox 1980; Unno et al. 1989),

$$W(M_r) = \frac{\pi}{\sigma_{\rm R}} \int_0^{M_r} \Re \left[\frac{\delta T^*}{T} \left(\delta\epsilon - \frac{d}{dM_r} \delta L_{\rm rad} \right) \right] dM_r, \tag{6.1}$$

where M_r is the enclosed mass, T is the temperature, ϵ is the nuclear energy generation rate per unit mass, $L_{\rm rad}$ is the radiative luminosity, and the symbols with δ represent the Lagrange perturbations, where symbol $\Re$ denotes the real part of the quantity indicated in the bracket. The work integral has the physical meaning of the pulsation energy gained inside M_r in a single period. If the sign of the work integral is positive at the stellar surface, i.e., $W(M_*) > 0$, the stars gain kinetic energy in each period and are unstable. The pulsation amplitude increases during the growth timescale of the instability $\sigma_{\rm I}^{-1}$. If $W(M_*) < 0$, on the other hand, the pulsation damps inside the stars and are stable. The first term in the bracket on the right-hand side of equation (6.1), proportional to $\delta\epsilon$, represents the driving of instability by the nuclear burning (i.e., the ϵ mechanism). The second term is related to the radiative energy transport. In most cases, the radiative diffusion damps the pulsation, and thus the second term contributes to the stabilization. However, in the surface layer where the opacity changes remarkably, the energy flux transported via radiation can be absorbed and be converted into the pulsation energy by the κ mechanism. The growth (or damping) rate of the pulsation per single period $\eta \equiv -\sigma_{\rm I}/\sigma_{\rm R}$ is written as

$$\eta \equiv -\frac{\sigma_{\rm I}}{\sigma_{\rm R}} = \frac{W(M_*)}{4\pi E_{\rm W}}, \tag{6.2}$$

(see Cox 1980; Unno et al. 1989), where

$$E_{\rm W} = \frac{\sigma_{\rm R}^2}{2} \int_0^{M_*} |\xi_r|^2 dM_r \tag{6.3}$$

is the pulsation energy, and ξ_r is the radial displacement of fluid elements from their equilibrium positions.

In stars which are unstable under linear perturbations, the pulsation amplitude will grow to the non-linear regime. Such a strong pulsation is expected to cause a mass loss from the stellar surface (Appenzeller 1970a,b; Papaloizou 1973a,b). Appenzeller (1970a,b) studied the non-linear growth of the radial-pulsation instability for Pop I massive stars of $M_* = 130$ and 270 $\dot{M}_{\rm acc}$ using one-dimensional hydrodynamical calculations. He showed that after the pulsation enters the non-linear regime, the surface velocity reaches the speed of sound and weak shocks emerge just inside the photosphere. The shocks recurrently propagate outward and accelerate the gas in the surface layer (e.g., Lamers and Cassinelli 1999), generating mass shells exceeding the escape velocity which is then lost from the star.

In this paper, we evaluate the mass-loss rate following Baraffe et al. (2001) and Sonoi and Umeda (2012). As shown by Appenzeller (1970a,b), outflows are launched when the pulsation velocity at the surface reaches the speed of sound $c_{\rm s}$. At this moment, the pulsation amplitude at the surface is

$$\xi_{r,{\rm surf}} = \frac{c_{\rm s}}{\sigma_{\rm R}}. \tag{6.4}$$

Using this, we can estimate the pulsation energy $E_{\rm W}$ as well as the work integral W. Assuming that all the pulsation energy is converted into the kinetic energy of the outflows, the mass-loss rate $\dot{M}_{\rm loss}$ can be obtained from the energy conservation:

$$\frac{\dot{M}_{\rm loss}}{2} v_{\rm esc}^2 = \frac{\sigma_{\rm R}}{2\pi} W(M_*) = -2\sigma_{\rm I} E_{\rm W}, \tag{6.5}$$

where $v_{\rm esc} = (2GM_*/R_*)^{1/2}$ is the escape velocity.

Note that the assumption of energy conservation above is not always valid because some pulsation energy can be lost by radiative dissipation. In fact, (Papaloizou 1973a,b) obtains a mass-loss rate lower than that of Appenzeller (1970a,b) by one order of magnitude by including this effect. The mass-loss rate derived below can thus be regarded as a conservative upper limit.

6.2 Results

In this section, we describe the results for two different regimes of the accretion rate separately: (a) high accretion-rate cases ($\dot{M}_{\rm acc} \geq 0.03\ M_\odot\ {\rm yr}^{-1}$), where the accreting stars become supergiant protostars, and (b) a low accretion-rate case ($\dot{M}_{\rm acc} = 10^{-3}\ M_\odot\ {\rm yr}^{-1}$), where it reaches the ordinary ZAMS. The high-rate regime corresponds to the cases of the SMS formations, while the lower rates are expected in the ordinary Pop III star formation. The latter results are presented for comparison with the previous studies (Baraffe et al. 2001; Sonoi and Umeda 2012). Since we have found that accreting protostars are unstable only for the radial mode without nodes (fundamental mode or "F-mode"), we present the results for the F-mode below.

6.2.1 High accretion-rate cases: supergiant protostars

We see here the high accretion-rate cases $\dot{M}_{\rm acc} \geq 0.03\ M_\odot\ {\rm yr}^{-1}$, where the protostars grow in mass through the supergiant-protostar phase (Figure 6.1). We first explain the case with the highest accretion rate $\dot{M}_{\rm acc} = 1.0\ M_\odot\ {\rm yr}^{-1}$ and then the cases with the lower rates.

Highest Accretion-Rate Case ($\dot{M}_{\rm acc} = 1.0\ M_\odot\ {\rm yr}^{-1}$)

Figure 6.2 shows the stellar interior structure when the stellar mass reaches $10^3\ M_\odot$ with $\dot{M}_{\rm acc} = 1.0\ M_\odot\ {\rm yr}^{-1}$. No convective core develops in the interior since the hydrogen burning has not yet started. The star instead consists of a radiative core and an outer convective layer. Although the convective layer only constitutes 10% of the stellar mass, and the remaining 90% is the radiative core, it covers a large portion of the radius. This structure consisting of the central core and bloated envelope is similar to that of red-giant stars. With $\dot{M}_{\rm acc} = 1.0\ M_\odot\ {\rm yr}^{-1}$, the protostar reaches this structure at $M_* > 200\ M_\odot$. In this evolutionary stage, the stellar luminosity is close to the Eddington value ($L_* \simeq L_{\rm Edd} \propto M_*$), and the effective temperature remains almost constant at $T_{\rm eff} \simeq 5000$ K due to the strong temperature-dependence of the H^- bound-free opacity. With these two conditions, the mass-radius relationship of the supergiant protostars is analytically written as

$$R_* \simeq 8.2 \times 10^3\ R_\odot \left(\frac{M_*}{10^3\ M_\odot} \right)^{1/2}, \tag{6.6}$$

which well agrees with the numerical results (HOY12).

Figure 6.3 shows the spatial distributions of the work integral for the radial F-mode at the stellar masses of 300, 500, and $10^3\ M_\odot$. The work integral W changes remarkably near the surface ($< 3 \times 10^5$ K), in particular, around 4×10^4 K, due to a opacity bump by the He^+ ionization. At 300 and 500 $M_\odot$, the work integrals are negative at the surface and the stars are stable. At $M_* = 10^3\ M_\odot$, on the other hand,

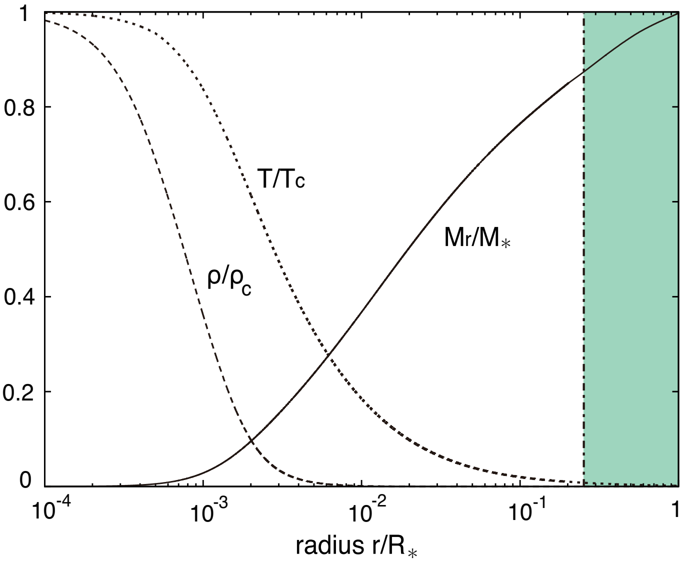

Figure 6.2: The interior structure of the accreting 10^3 $M_\odot$ protostar with $\dot{M}_{\rm acc} = 1.0$ $M_\odot$ yr^{-1} as a function of the relative radius r/R_*. The lines present the radial profiles of the enclosed mass (solid), density (dashed), and temperature (dotted), respectively. The enclosed mass is normalized by the stellar mass and others are normalized by their central values; $\rho_{\rm c} = 0.2$ g cm^{-3} and $T_{\rm c} = 2.1 \times 10^7$ K. The vertical line at $r/R_* \simeq 0.25$ denotes the inner boundary of the convective envelope. This figures is taken from Inayoshi et al. (2013).

the work integral at the stellar surface is positive, i.e., the protostar is pulsationally unstable by the κ mechanism excited in the He$^+$ ionization layer.

All the work integrals shown in Figure 6.3 are constant in the outer H^0 and He^0 ionization layers since the radiative energy transport is efficient enough there. The κ mechanism neither excite nor damp the pulsation. This can be seen by comparing the following two timescales, the cooling time in the layer outside a radius r in the unperturbed state (thermal timescale; e.g., Sonoi and Shibahashi 2011)

$$t_{\rm th} \equiv \frac{\int_r^{R_*} 4\pi c_P T \rho r^2 dr}{L}, \tag{6.7}$$

and the period of the pulsation

$$t_{\rm dyn} \equiv \frac{2\pi}{\sigma_{\rm R}}. \tag{6.8}$$

The open circles in the Figure 6.3 indicate the transition points where the two timescales equal each other ($t_{\rm th} = t_{\rm dyn}$). Outside this point, $t_{\rm th}$ is shorter than $t_{\rm dyn}$ as the density and the specific heat decrease outward. We call this region where $t_{\rm th} < t_{\rm dyn}$ as the *non-adiabatic zone*. The variation of the work integral is almost zero there because the entropy is rapidly dissipated during a pulsation period. Thus, the surface value of

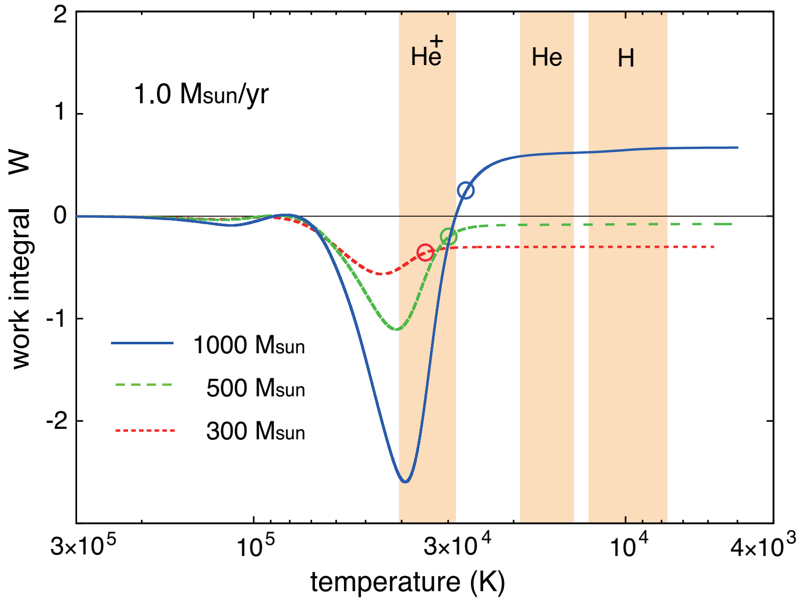

Figure 6.3: Radial distributions of the work integral W (in an arbitrary unit) near the stellar surface ($T < 3 \times 10^5$ K) for $\dot{M}_{\rm acc} = 1.0\ M_\odot\ {\rm yr}^{-1}$. The lines represent the $M_* = 300$ (dotted), 500 (dashed), and $10^3\ M_\odot$ (solid) stars. The shaded zones denote the ionization layers of He$^+$, He, and H from left to right. Open circles mark the transition points, where the thermal timescale is equal to the dynamical timescale, $t_{\rm th} = t_{\rm dyn}$. This figures is taken from Inayoshi et al. (2013).

the work integral, which determines the pulsational stability of the star, is fixed at the transition point to the non-adiabatic zone, where $t_{\rm th} = t_{\rm dyn}$.

As seen in Figure 6.3, the surface value of the work integral $W(M_*)$ increases with the stellar mass and eventually becomes positive for $> 500\ M_\odot$: the protostar becomes pulsationally unstable. Since the work integral grows in the He$^+$ ionization layer inside the transition point but remains constant outside. This increase of the surface value $W(M_*)$ with the stellar mass can be understood by the concomitant outward-shift of the transition point, which in turn can be explained by comparing the two timescales;

$$t_{\rm th} \propto \frac{R_*^3}{L_*}, \tag{6.9}$$

and

$$t_{\rm dyn} \propto \sqrt{\frac{R_*^3}{M_*}} \tag{6.10}$$

near the surface. In deriving the equation (6.9), we used the fact that the term $c_P T \rho$ in equation (6.7) changes only slightly for $T < 4 \times 10^5$ K in the range $10^2\ M_\odot < M_* < 10^3\ M_\odot$. Note that the dynamical timescale (equation 6.10) has the same dependence as the free-fall timescale of the star. Eliminating R_* and L_* in equations (6.9) and (6.10) with equation (6.6) and $L_* \simeq L_{\rm Edd}$, we obtain:

$$\frac{t_{\rm dyn}}{t_{\rm th}} \propto M_*^{-1/4}, \tag{6.11}$$

the thermal timescale becomes longer with respect to the dynamical timescale near the surface with increasing stellar mass. In other words, the surface layer becomes more adiabatic: the non-adiabatic zone on the surface layer becomes thinner and the transition point moves outward as seen in Figure 6.3. As a result, the surface value of the work integral increases and the stars become more unstable as the stellar mass increase.

The growth rate of the pulsation η and the resulting mass-loss rate $\dot{M}_{\rm loss}$ are shown in Figure 6.4 as a function of the stellar mass. At $M_* \simeq 600\ M_\odot$, the star becomes pulsationally unstable and the mass loss rate increases with the stellar mass thereafter. At $M_* \simeq 10^3\ M_\odot$, the mass-loss rate reaches $2 \times 10^{-3}\ M_\odot\ {\rm yr}^{-1}$, two orders of magnitude higher than that in the ZAMS case with accretion rate $\dot{M}_{\rm acc} = 10^{-3}\ M_\odot\ {\rm yr}^{-1}$ (see section 6.2.2 below). This is, however, still lower than the accretion rate by a factor of 500. In the case with spherical symmetry, therefore, pulsation-driven outflow would be completely quenched by the rapid accretion. With some angular momentum, the accretion onto the star proceeds mostly through a circumstellar disk. In this case, the outflow escapes unhindered in the polar directions where the stellar surface is not covered by the accreting flow. We thus expect that the supergiant protostar loses some material via bipolar pulsation-driven outflows, while simultaneously growing in mass due to a more rapid accretion from the disk.

Variation with different accretion rates

Next we see the cases with lower accretion rate $0.03 - 0.3\ M_\odot\ {\rm yr}^{-1}$. Figure 6.5 presents the growth rate η for the radial F-mode in these cases as functions of the stellar mass. Roughly speaking, at a given stellar mass, the growth rate η is higher for higher accretion rates. In our analysis, stars are unstable (i.e. $\eta > 0$) only in the two highest accretion rate cases,: those with $1.0\ M_\odot\ {\rm yr}^{-1}$ for $M_* > 600\ M_\odot$ and with $0.3\ M_\odot\ {\rm yr}^{-1}$ for $M_* > 900\ M_\odot$.

This tendency of instability toward higher accretion rates can be understood again from the outward-shift of the transition point between the adiabatic and non-adiabatic zones inside the He$^+$ ionization layer, which makes the surface value of the work integral $W(M_*)$ higher (see section 6.2.1). The behavior of work integral W is shown in Figure 6.6 for three accretion rates of 0.1, 0.3, and $1.0\ M_\odot\ {\rm yr}^{-1}$ at $M_* = 10^3\ M_\odot$. The ratio of the timescales $t_{\rm dyn}/t_{\rm th}$ depends on the accretion rate $\dot{M}_{\rm acc}$ only through the stellar surface luminosity L_* (see equations 6.6, 6.7, and 6.8 and note that the stellar radius is independent of $\dot{M}_{\rm acc}$). As shown in Figure 6.7 (a) the surface luminosity L_* and the ratio $t_{\rm dyn}/t_{\rm th}$ is lower for higher $\dot{M}_{\rm acc}$. In other words, the surface region be-

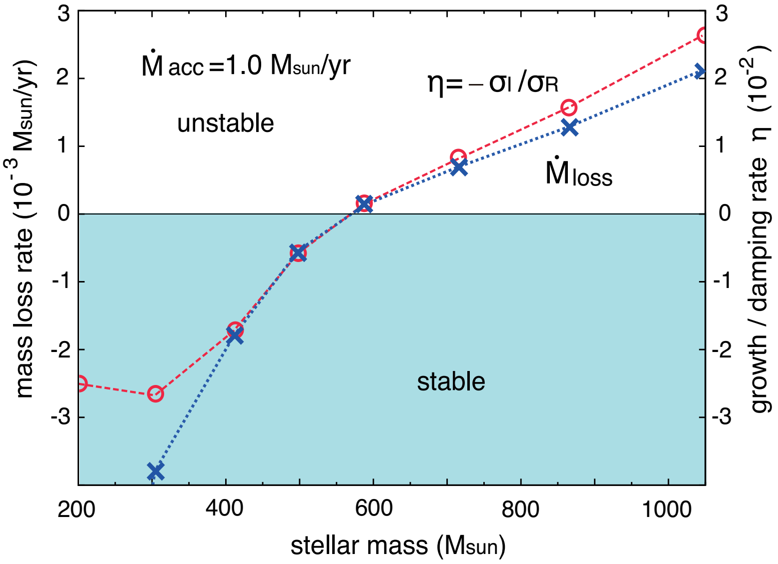

Figure 6.4: The growth/damping rate $\eta(= -\sigma_{\rm I}/\sigma_{\rm R})$ and the mass-loss rate $\dot{M}_{\rm loss}$ as a function of stellar mass for $\dot{M}_{\rm acc} = 1.0\ M_\odot\ {\rm yr}^{-1}$. The left (right) vertical axis shows $\dot{M}_{\rm loss}$ in unit of $10^{-3}\ M_\odot\ {\rm yr}^{-1}$ (η in unit of 10^{-2}, respectively). In the shaded area the star is stable against the radial pulsation, i.e., $\eta < 0$. This figures is taken from Inayoshi et al. (2013).

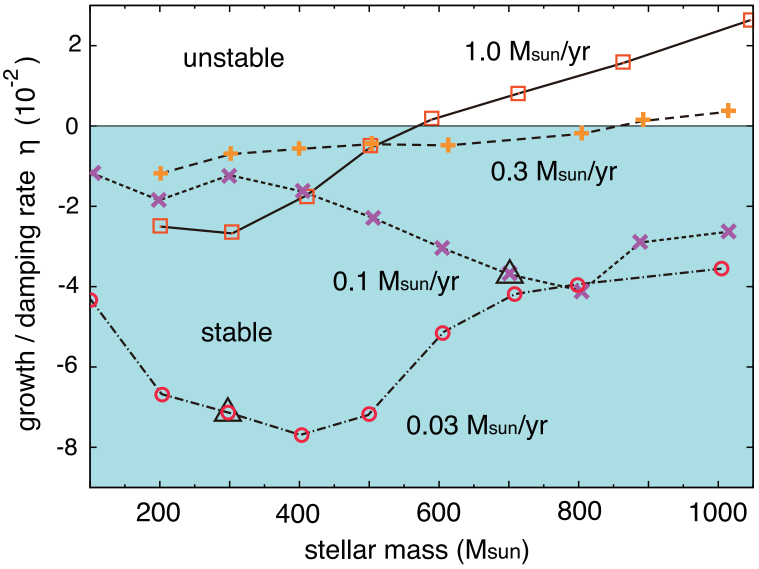

Figure 6.5: The growth/damping rate $\eta = -\sigma_{\rm I}/\sigma_{\rm R}$ as a function of stellar mass for $\dot{M}_{\rm acc} = 1.0$ (solid), 0.3 (long-dashed), 0.1 (short-dashed), 0.03 $M_\odot\ {\rm yr}^{-1}$ (dash-dotted), respectively. In the shaded area the star is stable against the radial pulsation ($\eta < 0$). The symbols on the lines show the models for which we analyze the stability. Large open triangles on the cases with 0.1 and 0.03 $M_\odot\ {\rm yr}^{-1}$ indicate the onset of the hydrogen burning. This figures is taken from Inayoshi et al. (2013).

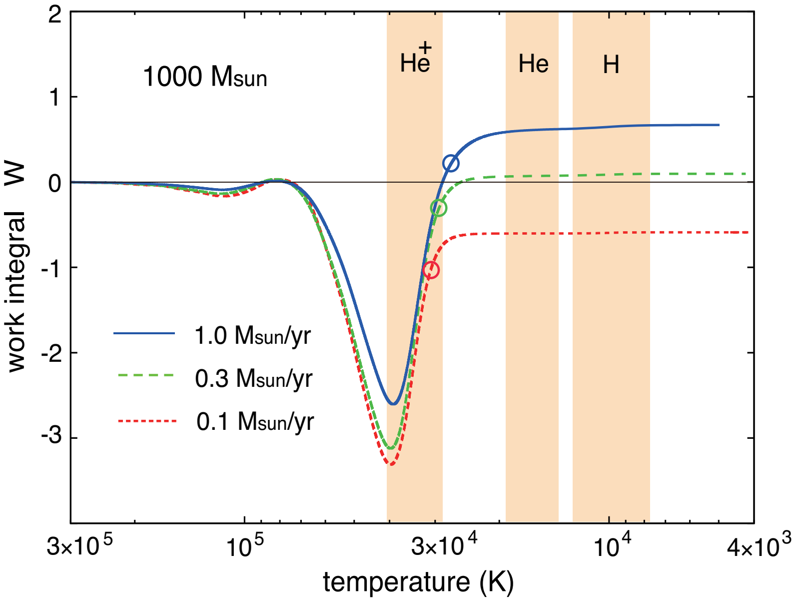

Figure 6.6: The same as Figure 6.3, but for the stellar models at 10^3 $M_\odot$ with three different accretion rates $\dot{M}_{\rm acc}$ = 1.0 $M_\odot$ yr^{-1} (solid), 0.3 $M_\odot$ yr^{-1} (dashed), and 0.1 $M_\odot$ yr^{-1} (dotted). This figures is taken from Inayoshi et al. (2013).

comes more adiabatic and the transition point moves closer to the surface at higher $\dot{M}_{\rm acc}$, which makes the surface value of work integral higher as well.

The above relation of L_* and $\dot{M}_{\rm acc}$ can be understood in the following way. With lower $\dot{M}_{\rm acc}$, the central part of the star has longer time to lose its entropy and the star takes a more centrally concentrated structure at a given stellar mass maintaining the same stellar radius (see Figure 6.7 b). As the radiative energy transport is efficient in the inner hot and dense part, such a star has larger radiative core. Since the luminosity grows proportionally to the enclosed mass M_r inside the radiative core but remains roughly constant outside (see Figure 6.7 a), the large radiative core at low $\dot{M}_{\rm acc}$ results in high value of surface luminosity L_*.

Although the overall behavior of the growth rate η shown in Figure 6.5 can be understood with the above considerations, η evolves in a somewhat complicated way at $\dot{M}_{\rm acc}$ = 0.03 and 0.1 $M_\odot$ yr^{-1}; i.e., η decreases with mass early in the evolution. The reason is as follows. As seen above, a supergiant protostar becomes more centrally concentrated and thus more stable (i.e., lower η) with the increasing mass. At the same time, however, there is also a destabilization effect with mass which is due to the shrinking of the non-adiabatic layer of the surface, as discussed in section 6.2.1. These two effects compete each other. With the highest accretion rates of $\dot{M}_{\rm acc}$ = 0.3 and 1.0 $M_\odot$ yr^{-1}, the destabilization is more important, while in the cases with low accretion rate of $\dot{M}_{\rm acc}$ = 0.03 and 0.1 $M_\odot$ yr^{-1}, the stabilization first dominates until

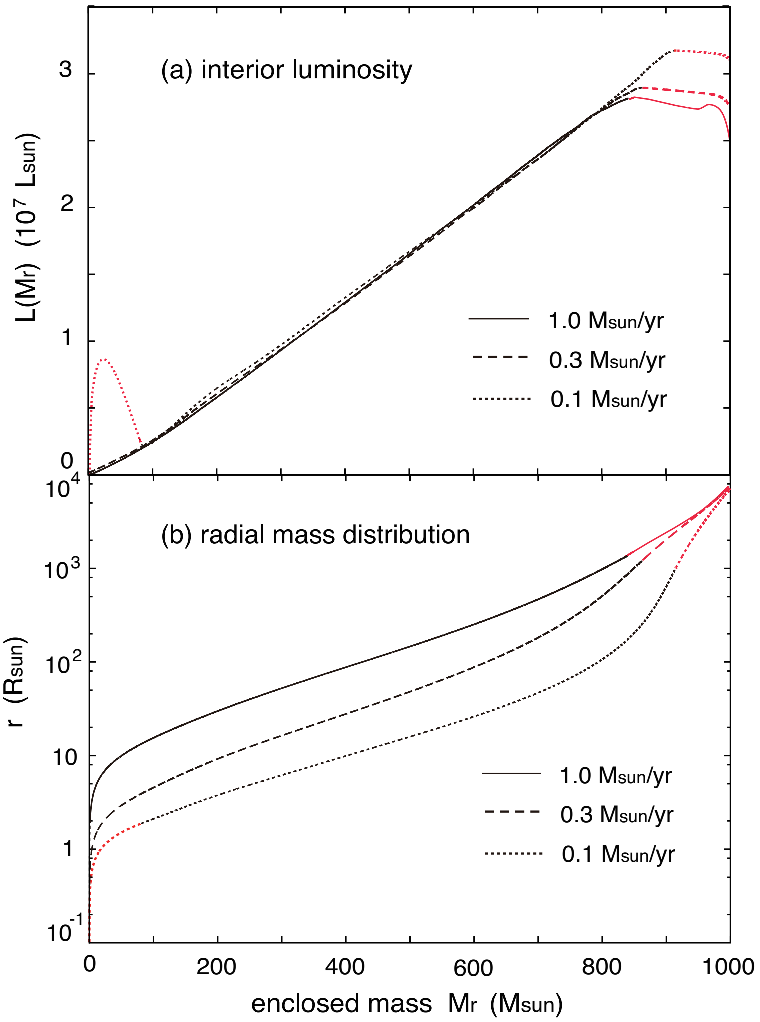

Figure 6.7: Comparison of the interior structure of 10^3 $M_{\odot}$ protostars with different accretion rates. The panels (a) and (b) present the radial distributions of the luminosity and enclosed mass, respectively. In the both panels, the red portions denote the convective zones. This figures is taken from Inayoshi et al. (2013).

the onset of hydrogen burning, after which the central concentration remains almost constant and the stabilizing effect no longer operates. Thus, at this point η begins to increase as seen in Figure 6.5.

6.2.2 Lowest accretion-rate case: Accreting ZAMS stars

Next, we will see the lowest accretion-rate case in our calculation with $\dot{M}_{\rm acc} = 10^{-3}\ M_{\odot}\ {\rm yr}^{-1}$, where the protostar reaches the ZAMS at $M_* \simeq 50\ M_{\odot}$ after the KH contraction (e.g., Omukai and Palla 2003).

Figure 6.8 presents the interior structure of the protostar $M_* = 10^3\ M_{\odot}$: the radial profiles of the mass, the temperature, the density, and the nuclear energy production

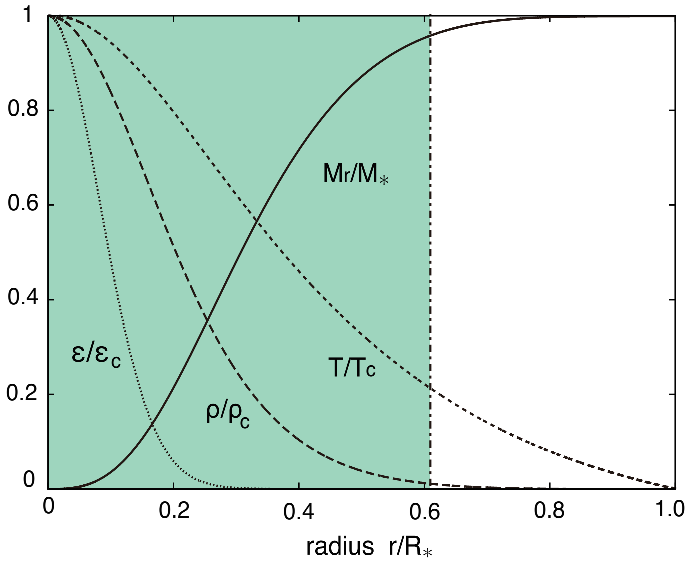

Figure 6.8: The same as Figure 2, but for the 10^3 $M_\odot$ protostar with $\dot{M}_{\rm acc} = 10^{-3}$ $M_\odot$ yr^{-1}. The energy production rate due to the nuclear burning is also shown (dotted). The enclosed mass is normalized by the stellar mass, and others are by their central values: $\rho_{\rm c} = 11$ g cm^{-3}, $T_{\rm c} = 1.3 \times 10^8$ K, and $\epsilon_{\rm c} = 6.9 \times 10^5$ erg s^{-1} g^{-1}. The vertical line at $r/R_* \simeq 0.6$ denotes the outer boundary of the convective core. This figures is taken from Inayoshi et al. (2013).

rate. The central hydrogen burning via CN-cycle renders the 95% of the stellar mass (covering 60% in radius) to be convective. The vertical line (dot-dashed) in Figure 6.8 indicates the boundary between the convective core and the outer radiative envelope.

Figure 6.9 shows the radial distributions of the work integral W, its derivative dW/dM_r, its nuclear-energy production rate ϵ, and its opacity κ within this star. The ϵ-mechanism drives the pulsational instability and thus the work integral W increases inside the convective core. On the other hand, the pulsation is slightly damped (i.e. $dW/dM_r < 0$) in the radiative layer because of the energy dissipation. The κ mechanism does not work as the opacity is almost constant in the envelope due to high surface temperature ($\sim 10^5$K). The small mass inside the surface region cannot totally damp the pulsation excited by the ϵ mechanism. The star is thus unstable, i.e., $W(M_*) > 0$.

Figure 6.10 presents the growth rate of the pulsation η and the resulting mass-loss rate $\dot{M}_{\rm loss}$ as a function of the stellar mass. After hydrogen ignition at $M_* \simeq 50$ $M_\odot$, the star remains stable until 140 $M_\odot$ when the stabilization by radiative damping overcomes the pulsation by the ϵ mechanism. As the stellar mass increases, however, the star becomes more radiation-pressure dominated and the average adiabatic exponent of the star $\Gamma_1 \equiv (\partial \ln p/\partial \ln \rho)_S$ approaches the marginal gravitational stability value of 4/3. Consequently, the pulsation becomes increasingly strong in the central convective core and exceeds the radiative damping effect (Cox 1980; Shapiro and Teukolsky 1983).

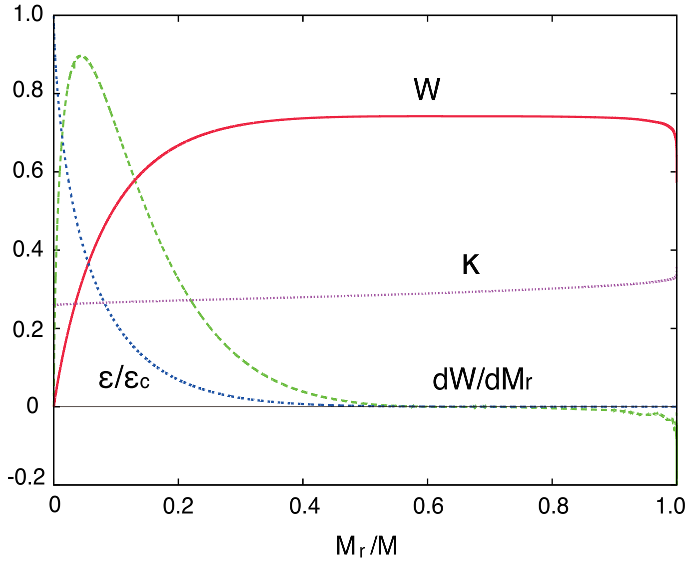

Figure 6.9: Radial distributions of several quantities within the $M_* = 10^3\ M_\odot$ star with $\dot{M}_\mathrm{acc} = 10^{-3}\ M_\odot\ \mathrm{yr}^{-1}$. The work integral W (solid line) and its derivative dW/dM_r (long-dashed line) are presented in arbitrary units. The nuclear energy production rate ϵ (normalized by the central value) and the opacity κ (in $\mathrm{cm}^2\ \mathrm{g}^{-1}$) are plotted with the short-dashed and dotted lines, respectively. This figures is taken from Inayoshi et al. (2013).

The star becomes unstable at 140 $M_\odot$ and the growth rate of the pulsation increases thereafter. The mass-loss rate is typically $\dot{M}_\mathrm{loss} \simeq 10^{-6} - 10^{-5}\ M_\odot\ \mathrm{yr}^{-1}$ (the dotted line in Figure 6.10). Since this mass-loss rate is lower than the accretion rate $\dot{M}_\mathrm{acc} = 10^{-3}\ M_\odot\ \mathrm{yr}^{-1}$, the stellar growth via accretion would not be prevented by the pulsation-driven mass-loss as in the supergiant protostar cases.

Baraffe et al. (2001) and Sonoi and Umeda (2012) also studied the pulsational instability of non-accreting massive Pop III stars. For example, Sonoi and Umeda (2012) estimate the growth rate of the pulsation and mass-loss rate for a 500 $M_\odot$ star as $\eta = 3.02 \times 10^{-8}$ and $\dot{M}_\mathrm{loss} = 2.0 \times 10^{-5}\ M_\odot\ \mathrm{yr}^{-1}$, respectively. Although their growth rate agrees well with our results, their mass-loss rate is higher than ours by a factor of four. This difference in mass-loss rates comes from the different values of the surface density between the accreting and non-accreting stars. With accretion, the surface density is higher than that without accretion. In this case, the gas pressure is relatively higher than the radiation pressure, i.e., higher $\beta \equiv p_\mathrm{gas}/p_\mathrm{tot}$. This results in a lower sound velocity $c_\mathrm{s} = \sqrt{\Gamma_1 p/\rho}$ ($\propto \beta^{-1/2}$) at the surface and a lower pulsation amplitude at the onset of the mass loss, which is proportional to the speed of sound (equation 6.4). Therefore, the pulsation energy E_W and the mass-loss rate become lower in the accreting case than in the non-accreting case.

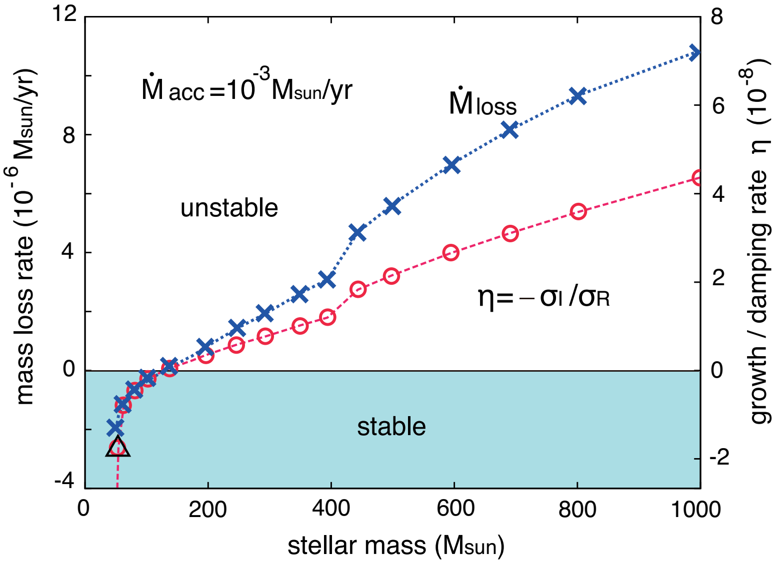

Figure 6.10: The growth/damping rate $\eta(= -\sigma_{\rm I}/\sigma_{\rm R})$, and the mass loss rate $\dot{M}_{\rm loss}$ as a function of stellar mass for $\dot{M}_{\rm acc} = 10^{-3}\ M_\odot\ {\rm yr}^{-1}$. The left (right) vertical axis shows $\dot{M}_{\rm loss}$ in unit of $10^{-6}\ M_\odot\ {\rm yr}^{-1}$ (η in unit of 10^{-8}, respectively). The protostar is stable ($\eta < 0$) against the radial pulsation (F-mode) in the shaded area. Open triangles indicate the onset of the hydrogen burning. This figures is taken from Inayoshi et al. (2013).

6.3 Conclusion and Discussion

In this paper, we have studied the pulsational stability of primordial protostars growing via very rapid accretion, ($\dot{M}_{\rm acc} \sim 0.1\ M_\odot\ {\rm yr}^{-1}$), through the method of the linear perturbation analysis, which is expected in the case of supermassive star formation in the early universe. We have evaluated mass-loss rate if the protostar is pulsationally unstable and examined whether the mass loss is strong enough to prevent the stellar growth via the accretion. We focused on early stellar evolution of $M_* < 10^3\ M_\odot$, which has been studied in our recent work (HOY12). Our results are summarized as follows.

First, we have studied the high accretion-rate cases with $\dot{M}_{\rm acc} > 0.03\ M_\odot\ {\rm yr}^{-1}$, where the protostar has the a contracting core and a bloated envelope similar to a giant star (*supergiant protostar*; HOY12). With low effective temperature $T_{\rm eff} \simeq 5000$ K, the supergiant protostar has the H and He ionization layers within its envelope. We have found that although pulsation is driven due to blocking of radiative flux at the opacity bump from the He$^+$ ionization (the so-called κ mechanism), the supergiant protostars are pulsationally unstable only with the highest accretion rate $\simeq 1.0\ M_\odot\ {\rm yr}^{-1}$ we studied. In the lower accretion-rate cases, the protostars are stable at least until $M_* \simeq 10^3\ M_\odot$. Even in the most unstable cases, the mass-loss rates are typically

$\sim 10^{-3}\ M_\odot\ \mathrm{yr}^{-1}$, which are lower than their accretion rates by more than two orders of magnitude. We thus conclude that the mass loss driven by pulsation does not prevent the growth of the supergiant protostar via rapid accretion.

Next, for comparison with the previous studies, we have analyzed a lower accretion-rate case with $\dot{M}_{\mathrm{acc}} = 10^{-3}\ M_\odot\ \mathrm{yr}^{-1}$, which is expected in the ordinary Pop III star formation. In this case, the protostar reaches the ZAMS at $M_* \simeq 50\ M_\odot$ after the KH contraction stage (e.g., Omukai and Palla 2001, 2003). We have found that the protostars are unstable by the ϵ mechanism in the range $M_* > 140\ M_\odot$, where a large part of the stellar interior is radiation-pressure dominated. Estimated mass-loss rate $10^{-6} - 10^{-5}\ M_\odot\ \mathrm{yr}^{-1}$ is roughly consistent with the previous results for non-accreting stars (Baraffe et al. 2001; Sonoi and Umeda 2012) although smaller by few factors because of the difference in the surface density due to the accretion.

In this paper, we have limited our analysis to the mass range $M_* < 10^3\ M_\odot$ due to the lack of stellar data in the higher mass range. We here speculate the later evolution based on the current results. Further studies on the protostellar evolution for $M_* > 10^3\ M_\odot$ as well as on its pulsational stability are thus awaited. If we linearly extrapolate the mass-loss rate in the case of $\dot{M}_{\mathrm{acc}} = 1.0\ M_\odot\ \mathrm{yr}^{-1}$ shown in Figure 6.4 to higher mass range,

$$\dot{M}_{\mathrm{loss}} \sim 5.0 \times 10^{-4} \left(\frac{M_*}{100\ M_\odot} - 6 \right)\ M_\odot\ \mathrm{yr}^{-1}; \tag{6.12}$$

the mass loss catches up with the accretion at $M_* \simeq 2 \times 10^5\ M_\odot$. At this point, the growth of the protostar via accretion possibly halts and the final mass is set. However, because of our assumption that all the pulsation energy is converted to the kinetic energy of the outflows, the mass-loss rate by equation (6.12) should be regarded as an upper limit (e.g., Papaloizou 1973a,b). Furthermore, the mass loss of the Pop I red-giant stars are usually driven by the radiation pressure exerted on dust grains formed in the cool envelope (e.g., Willson 2000). Without the dust as in our case, acceleration of the outflows could be more inefficient. We expect that, with such rapid accretion, the final stellar mass can exceed $\sim 10^5\ M_\odot$ despite the pulsation-driven mass loss.

Although mass-loss rate is much lower than the accretion rate until $M_* = 10^3\ M_\odot$ as studied in this paper, these values could be comparable to $M_* > 10^5\ M_\odot$. Since the accretion of gas with some angular momentum onto the star proceeds via a circumstellar disk, the outflows would escape most easily in the polar regions, where the density is relatively low. The dynamical interaction between the inflows and outflows needs to be studied in detail to determine the exact value of the stellar final mass.

Our estimate of the mass-loss rate is based on the previous works (e.g., Appenzeller 1970a,b; Papaloizou 1973a,b), in which the non-linear development of pulsation for non-accreting main-sequence stars is studied numerically. For the accreting stars, however, we have a very limited knowledge on the non-linear behavior of pulsation (e.g., Gamgami 2007). More detailed studies on this issue by radiative hydrodynamical simulations is awaited.

So far, we have only considered stars forming from the metal-free ($Z = 0$) gas. However, SMSs could potentially be formed from the gas slightly polluted with heavy elements, if that is below the critical amount $Z_{\rm cr}$, i.e., $\sim 10^{-3}\ Z_{\odot}$ without dust grains, or $\sim 10^{-5}\ Z_{\odot}$ with dust grains (Omukai et al. 2008; Inayoshi and Omukai 2012). Metal enrichment lowers the central temperature of a star by enhancing the energy production efficiency by nuclear fusion and also creates another opacity bump near the surface which make the pulsation stronger via the ϵ and κ mechanisms, respectively. However, for the κ mechanism, for which the supergiant protostars are unstable, this effects becomes important only with metallicity higher than $2 \times 10^{-3}\ Z_{\odot}$ in the case of non-accreting stars (Baraffe et al. 2001), which is higher than the critical value $Z_{\rm cr}$. We thus speculate that even if small amount of metals below $Z_{\rm cr}$ are present, the pulsational stability of supergiant protostars should be similar to the zero-metallicity case studied above.

Finally, we discuss the validity of the frozen-in approximation of convective energy flux used in our analysis (see Appendix A), where perturbations of the convective flux is neglected. At the present time, this is a widely-used approximation due to our limited knowledge on the interaction between the convective and pulsational motions. Although some other models including this effect have been proposed (e.g., Unno 1967; Gough 1977; Dupret et al. 2005), they rely on the still-developing time-dependent convection theories, which require different assumptions depending on modeling, beyond the classical mixing-length theory (Böhm-Vitense 1958). Recent results by Penev et al. (2009) and Shiode et al. (2012), who studied this interaction numerically, showed that the convective damping weakens the pulsation by the ϵ mechanism, but does not influence through the κ mechanism. Therefore, protostars with modest accretion rate $\dot{M}_{\rm acc} \simeq 10^{-3}\ M_{\odot}\ {\rm yr}^{-1}$, which are unstable by the ϵ mechanism (section 6.2.2), can be somewhat stabilized by this convective damping. On the other hand, we speculate that this would not significantly affect the pulsation in supergiant protostars, which is driven by the κ mechanism.

Chapter 7

Evolution of supermassive stars by rapid mass accretion

In the previous studies of the stellar evolution (Hosokawa et al. 2012a, hereafter HYO12), the protostellar radius is found to expand monolithically with mass as $R_* \propto M_*^{1/2}$ for $M_* \gtrsim 100\ M_\odot$ (see equation 6.6). The bloated envelope has the low effective temperature ~ 5000 K during the expansion phase and thus the resulting stellar UV luminosity is very low. The pulsational instability of the accreting protostar is also studied (Inayoshi et al. 2013, hereafter IHO13). For $\dot{M}_{\rm acc} \gtrsim 10^{-1}\ M_\odot$, the protostar becomes unstable against the pulsations but drives outflows at the rate lower than the accretion rate. From these results, we expect that the protostar is not prevented the rapid growth. However, these studies only focused on the early evolution up to stellar masses of $10^3\ M_\odot$. Therefore, it is required to investigate the subsequent evolutionary stage until the protostar evolves to a supermassive star with $\sim 10^5\ M_\odot$. Here, we extend the previous work of HOY12 and discuss the evolution up to stellar masses $10^5\ M_\odot$ and effect of pulsational instability at the high mass range.

7.1 Evolution of stellar radius

We performed the calculations of the structure evolution for the accreting protostar as HYO12 did. We here use the numerical code developed by Yorke and Bodenheimer (2008), where the Henyey method (Henyey et al. 1964) is employed to solve the stellar interior structure. Figure 7.1 presents the evolution of the stellar radius and effective temperature with high accretion rates ($\dot{M}_{\rm acc} = 0.1$ and $1.0\ M_\odot\ {\rm yr}^{-1}$). We see that the evolution of the stellar radii agrees well with the previous results in an early stage for $M_* \lesssim 10^3\ M_\odot$ (HOY12). The small deviations for $M_* \lesssim 100\ M_\odot$ are mostly due to the difference of the boundary conditions imposed at the stellar surface, which does not affect the stellar structure for $M_* \lesssim 10^3\ M_\odot$. The stellar radii monolithically expand with mass according to the analytic relation (equation 6.6) for $100\ M_\odot \lesssim M_* \lesssim 10^4\ M_\odot$. For $M_* \gtrsim 3 \times 10^4\ M_\odot$, the protostar begins to shrink and the effective temperature

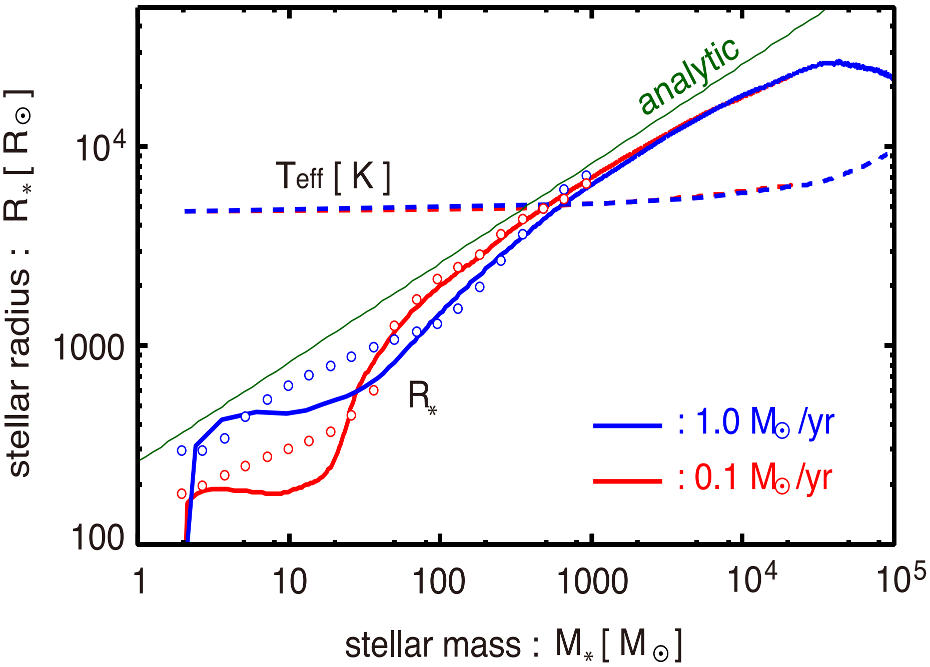

Figure 7.1: Protostellar evolution over $\sim 10^5$ years with accretion rates ($\dot{M}_{\rm acc} = 0.1\ M_\odot\ {\rm yr}^{-1}$ and $1.0\ M_\odot\ {\rm yr}^{-1}$). Upper panel: evolution of the stellar radius (solid lines). The open circles represent our previous results taken from Hosokawa et al. (2012a) for $M_* \lesssim 10^3\ M_\odot$ with $\dot{M}_{\rm acc} = 0.1$ and $1.0\ M_\odot\ {\rm yr}^{-1}$. The thin green line shows the analytic mass-radius relation given by equation (6.6). The evolution of the stellar effective temperature is also overlaid on the above plots (dashed lines), using the same scale as for the stellar radius. This figures is taken from Hosokawa et al. (2013).

simultaneously increases. When the stellar mass reaches $\sim 10^5\ M_\odot$, the stellar radius remains very large at $R_* \simeq 2 \times 10^4\ R_\odot \simeq 100$ AU. On the other hand, through the stellar evolution for $M_* \gtrsim 100\ M_\odot$, the interior continues to contract and thus the whole structure becomes highly inhomogeneously.

To understand why the radius begins to decrease for $M_* \gtrsim 10^4\ M_\odot$, we note that the constant effective temperature ($T_{\rm eff} \simeq 5000$ K) is assumed to derive the analytic relation (equation 6.6) from

$$L_* = 4\pi R_*^2 T_{\rm eff}^4 \simeq L_{\rm Edd} \propto M_*. \tag{7.1}$$

This is because H$^-$ bound-free opacity, which dominates near the stellar surface, has the strong temperature-dependence and thus the effective temperature is locked at several $\times\ 10^3$ K (Hayashi 1961). However, when the stellar mass exceeds $M_* > 10^4\ M_\odot$, the density of the outermost layer decrease to $\lesssim 10^{-11}$ g cm^{-3}. In such low-density surface, the opacity value drops to the floor given by the Thomson scattering because the H$^-$

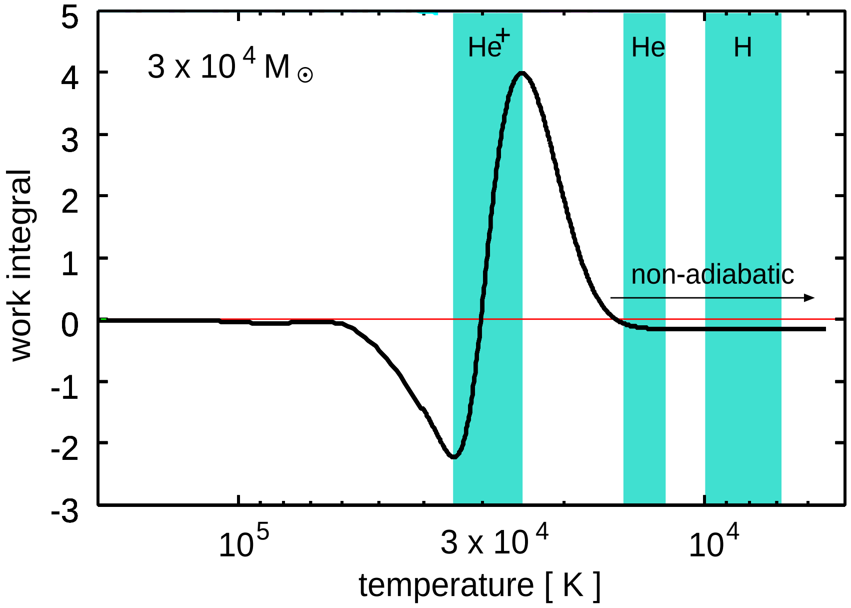

Figure 7.2: The work integral (in arbitrary units) for a 3×10^4 $M_\odot$ star accreting at the rate $\dot{M}_{\rm acc} = 1.0$ $M_\odot$ yr^{-1}. Only the distribution near the stellar surface is presented as a function of the interior temperature. The shaded backgrounds represent the ionization layers of He$^+$, He, and H. The outermost part is the non-adiabatic layer, where the pulsation instability is not excited because of radiative diffusion. This figures is taken from Hosokawa et al. (2013).

opacity is proportional to the density squared ($\sim n_{\rm H} n_{\rm e}$). At the point when H$^-$ ions no longer dominate the opacity in surface layers, these surface layers no longer efficiently absorb the heat flux coming from the contracting interior. In this case, the effective temperature does not keep to the constant value and increases as the protostar grows (see Figure 7.1). We thus predict that the stellar radius will continue to decrease as $R_* \propto M_*^{1/2} T_{\rm eff}^{-2}$ after the stellar mass exceeds 10^5 $M_\odot$,

7.2 Negative feedback effects

7.2.1 Stability against the stellar pulsations

We study the pulsation stability of accreting SMSs and estimate the resulting mass-loss rates for unstable cases. Following our previous work (IHO13), we apply linear stability analysis to the stellar models with different masses. IHO13 show that an SMS is more unstable with higher accretion rates and at higher stellar masses. We thus focus on the case with the highest accretion rate $\dot{M}_{\rm acc} = 1.0$ $M_\odot$ yr^{-1} for examining whether the mass loss caused by the stellar pulsation can limit stellar growth via mass accretion. Since accreting SMSs are most unstable against radial perturbations for $M_* \lesssim 10^3\ M_\odot$ (IHO13), we also analyze the stability against radial perturbations. Our current results allow us to extend the analysis to the high mass range of $10^3\ M_\odot \le M_* \le 10^5\ M_\odot$. The basic procedure of our linear stability analysis is briefly summarized in Appendix A.

In agreement with our previous analysis we find that the instability is excited by the κ mechanism due to the opacity bump in the He^+ ionization layer. The accreting SMS is always unstable, except within the narrow mass range $10^4\ M_\odot \lesssim M_* \lesssim 3 \times 10^4\ M_\odot$. The growth rate of the instability reaches the maximum value at $M_* \lesssim 6\times10^3\ M_\odot$. The maximum mass-loss rate is estimated as $5 \times 10^{-3}\ M_\odot\ \mathrm{yr}^{-1}$. At the second unstable phase ($\gtrsim 3 \times 10^4\ M_\odot$), the mass-loss rate hardly rises in spite of the growth rate increasing with stellar mass. This is primarily because the escape velocity increases with stellar mass (see eq. 6.5), as the stellar expansion slows down for $M_* \gtrsim 10^4\ M_\odot$ (see Fig. 7.1). Since the mass-loss rates are much lower than the assumed accretion rate, we conclude that the pulsation instability does not prevent the formation of an SMS via rapid mass accretion.

When the stellar mass exceeds $6 \times 10^3\ M_\odot$, the pulsation is stabilized and the pulsation-driven outflows are also suppressed. Figure 7.2 shows the radial profile of the work integral near the surface of a $3 \times 10^4\ M_\odot$ star. We see that the work integral increases outward within the He^+ ionization layer, but decreases beyond it because of radiative diffusion. In the outermost layers with $T \lesssim 1.8 \times 10^4$ K, where the radiative cooling time is shorter than the pulsation period, the work integral remains constant without excitation or damping (the *non-adiabatic region*; $t_{\mathrm{th}} < t_{\mathrm{dyn}}$). In this case, the work integral at the stellar surface is negative and the protostar is stable. In the most unstable case when $M_* = 6 \times 10^3\ M_\odot$, on the other hand, radiative cooling in the outermost part is more efficient and the non-adiabatic region extends further inward. The transition point to the non-adiabatic region is located just outside of the He^+ ionization layer. Therefore, the stellar pulsation excited in the He^+ ionization layer does not suffer from damping via radiative diffusion outside the ionization layer. Such a profile of the work integral is displayed in Figure 6.3, where by simply extrapolating the available results for $M_* < 10^3\ M_\odot$ without considering the damping effect outside the He^+ ionization layer, we had speculated that the mass-loss rates would increase with stellar mass for $M_* > 10^3\ M_\odot$. By contrast, our current results show that the pulsation instability is strongly suppressed for $M_* \gg 10^3\ M_\odot$ and mass-loss is much lower than predicted by IHO13 (equation 6.12).

7.2.2 UV feedback

As seen in Figure 6.1, for cases of usual Pop III star formation ($\dot{M}_{\mathrm{acc}} \simeq 10^{-3}\ M_\odot\ \mathrm{yr}^{-1}$), the stellar radius shrinks with increasing the mass (i.e., KH contraction) and reaches the

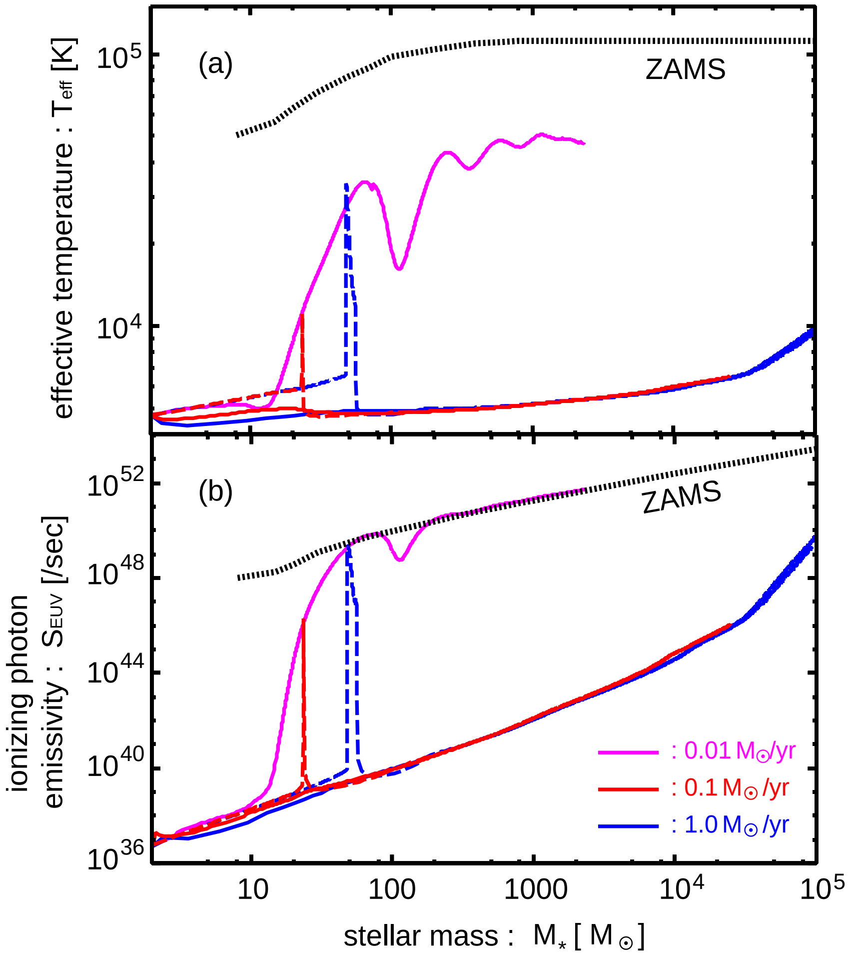

Figure 7.3: Evolution of the stellar effective temperature (*upper panel*) and ionizing photon emissivity (*lower panel*). The dotted line presents the values of ZAMS stars. This figures is taken from Hosokawa et al. (2013).

ZAMS stage. The effective temperature of the metal-free ZAMS star is higher than that of metal-enriched Pop II/I stars, which results in stronger emission of ionizing photons exceeding $\sim 10^{50}$ s^{-1} for $M_* > 10^2$ $M_\odot$ (see Figure 7.3). In this case, stellar UV feedback becomes so strong that the gas supply onto the star is rapidly prevented by the heating due to ionization (McKee and Tan 2008; Hosokawa et al. 2011; Stacy et al. 2012; Hosokawa et al. 2012a). On the other hand, in the case when SMSs forms via rapid mass accretion, the emissivity of the ionizing photons from the stellar surface remains very low even after the stellar mass exceeds 10^4 $M_\odot$. Figure 7.3 also shows that the luminosity of the ionizing photons for $\dot{M}_{\mathrm{acc}} = 1.0$ $M_\odot$ yr^{-1} at $M_* \simeq 10^5$ $M_\odot$ is still comparable to that of ZAMS stars with $M_* \lesssim 100$ $M_\odot$. This is because the protostar has the stellar envelope with low effective temperature resulting from the large stellar radius. For $\dot{M}_{\rm acc} = 1.0\ M_\odot\ {\rm yr}^{-1}$, the accretion rate of hydrogen atoms is $\simeq 3 \times 10^{49}\ {\rm sec}^{-1}$. If the stellar ionizing photon emissivity is lower than this hydrogen accretion rate, a $\rm H_{II}$ region cannot grow. Thus, the temporal increase of the ionizing luminosity in an early stage when $M_* < 100\ M_\odot$ (visible as a spike in Figure 7.3) [*], could affect the accreting flows. Even if this "flash" of ionizing radiation would occur, however, its duration of < 100 years is too short to significantly disturb the accretion flow. It is thus unlikely that the mass accretion onto rapidly accreting SMSs is hindered by stellar UV feedback, at least for $M_* \lesssim 10^5\ M_\odot$.

After the stellar mass exceeds $10^5\ M_\odot$, however, the stellar ionizing flux will continue to increase, so that an $\rm H_{II}$ region might finally emerge. The UV feedback caused by the dynamical expansion of the $\rm H_{II}$ region would shut off the mass accretion as expected in the ordinary cases of the primordial star formation. The maximum stellar mass by the UV feedback would be higher with more rapid mass accretion, as suggested in our radiation hydrodynamic numerical simulations (Hosokawa et al. 2011, 2012b).

7.3 Conclusion and Discussion

In this chapter, we study the evolution of an accreting protostar at the high rate ($\dot{M}_{\rm acc} > 0.1\ M_\odot\ {\rm yr}^{-1}$). We have solved the stellar structure numerically and found that such a protostar can grow up to a supermassive star with mass $\sim 10^5\ M_\odot$, which is expected to become a seed of SMBHs observed at $z \gtrsim 6$. Under rapid accretion, the stellar radius continues to increases monolithically with the stellar mass following $R_* \propto M_*^{1/2}$. The stellar interior inhomogeneously contracts by losing the thermal energy. These characteristics are consistent with that obtained by the previous study (Hosokawa et al. 2012a). The expansion phase ends and begins to contract when the mass exceeds $10^4\ M_\odot$. This is because the surface density decreases and thus the opacity of $\rm H^-$ ions drops to the Thomson scattering opacity. The maximum of the stellar radius is $R_* \simeq 4 \times 10^4\ R_\odot \sim 10^2$ AU for $M_* \gtrsim 10^4\ M_\odot$.

Our results suggest that SMSs form as very bloated supergiant stars as long as the rapid accretion continues. With this very large radius, the stellar effective temperature is less than 10^4 K even after the protostar becomes supermassive. Stellar UV radiation is much weaker than for non-accreting ZAMS stars. For instance, the ionizing luminosity of a rapidly accreting $10^5\ M_\odot$ star should be less than that of a $100\ M_\odot$ ZAMS star. Strong UV feedback, which could limit the mass accretion onto the star, is thus unlikely to operate in this case. We have also studied the pulsation stability of accreting SMSs with our calculated stellar models. Our analyses show that accreting SMSs become pulsation unstable due to the κ-mechanism (IHO13), but the resulting

---

[*] We investigated the stellar structure for various boundary conditions at the stellar surface relating to the energy input from accreting matter to the envelope. Depending on the choice of the boundary conditions, the evolution of the stellar radius somewhat different only in an early stage when $M_* < 100\ M_\odot$. Figure 7.3 shows the case that the emissivity of the ionizing photons is largest.

mass-loss rates are still much lower than the accretion rates for $M_* \gtrsim 10^3\ M_\odot$. We here note that our results of chapter 5 strongly support the rapid growth of the protostar at the rate as high as $\sim 3\ M_\odot\ \mathrm{yr}^{-1}$, which is larger than the threshold value to form the bloated supermassive star ($\sim 0.1\ M_\odot\ \mathrm{yr}^{-1}$). Therefore, we conclude that the SMSs formed via very rapid mass accretion are not significantly affected by stellar UV feedback or pulsational mass loss.

Chapter 8

Summary and conclusion

In this thesis, we have been discussed the origin and formation process of supermassive black holes (SMBHs; $\gtrsim 10^9\ M_\odot$) in the early universe through the direct collapse of supermassive stars (SMSs; $\gtrsim 10^5\ M_\odot$). We have investigated the formation of SMSs in the following three parts; (i) formation of supermassive clouds in the first galaxies, (ii) collapse phase of the supermassive cloud, (iii) evolution of the protostar up to a SMS. Below, we briefly summarize the results for each topics.

8.1 Formation of supermassive clouds

In chapter 3, we have reconsidered the conditions required to form SMSs in the early universe. In the previous studies, a strong far-ultraviolet (FUV) radiation field, which photodissociates H_2 and quenches its cooling, is expected to be a necessary condition for the SMS formation. However, candidates of FUV sources, including star-forming galaxies, are probably sources of strong CRs and X-rays too. We here have investigated the effects of external ionization by cosmic rays (CRs) and X-rays on the thermal evolution of primordial clouds under strong FUV radiation, and we have found the followings.

- An external ionization promotes H_2 production and elevates the threshold FUV intensity $J_{\rm crit}$ needed for SMBH formation for CR energy density $U_{\rm CR} \gtrsim 10^{-14}$ erg cm^{-3} or X-ray intensity $J_X \gtrsim 10^{-24}$ erg s^{-1} cm^{-2} sr^{-1} Hz^{-1} at 1 keV. The critical FUV flux increases as $J_{\rm crit} \propto U_{\rm CR}^{1/2}$ ($\propto J_X^{1/2}$) in the high CR (respectively X-ray) limit.
- With the same value of FUV intensity at the Lyman limit (13.6 eV), the H^- photodissociation rate, with a threshold of 0.755 eV, increases and the H_2 abundance decreases with decreasing effective temperature of the FUV sources T_*. A lower value of T_* thus results in a lower critical FUV flux $J_{\rm crit}$ at the Lyman limit.
- Using an empirical relation between the intensities of FUV and CRs/X-rays from

nearby star-forming galaxies, we find that the external ionization effect remarkably enhances the critical FUV flux for sources with T_* as high as 10^5 K and composed of stars with mass $\lesssim 100\ M_\odot$ to a level that is not realized in any halo.

Base on the above results, we conclude that to induce SMBH formation the FUV sources must be either Population II/I galaxies with low brightness temperature ($T_* \sim 10^4$ K), Population III galaxies ($T_* \sim 10^5$ K) with a very top-heavy initial mass function or Population III galaxies too young to harbor sources of CRs/X-rays, for example supernova remnants or high-mass X-ray binaries.

In chapter 4, we proposed a new scenario for SMS formation without assuming the strong FUV radiations, which are required in the previous studies. Recent numerical simulations indicate that assembly of a typical first galaxy with virial temperature $T_{\rm vir} \gtrsim 10^4$ K proceeds via cold and dense flows penetrating deep to the centre, where supersonic streams collide with each other to develop a hot ($\sim 10^4$ K) and dense ($\sim 10^3$ cm^{-3}) shocked gas. We have investigated the thermal evolution of the post-shock gas and found the followings.

- The post-shock layer first cools by efficient Lyα emission and contracts isobarically until $\simeq 8000$ K. If the density is high enough to excite H_2 rovibrational levels collisionally ($\gtrsim 10^4$ cm^{-3}), enhanced H_2 collisional dissociation suppresses the gas from cooling further.

- The range of post-shock conditions for SMS formation can be expressed as $T \gtrsim 6000$ K $(n_{\rm H}/10^4\ {\rm cm}^{-3})^{-1}$ for $n_{\rm H} \lesssim 10^4$ cm^{-3} and $T \gtrsim 5000-6000$ K for $n_{\rm H} \gtrsim 10^4$ cm^{-3}, depending somewhat on the initial ionization degree.

- Metal enrichment does not affect the above condition for metallicity below $\sim 10^{-3}\ Z_\odot$ if metals are in the gas phase, while condensation of several per cent of metals into dust decreases this critical value of metallicity by an order of magnitude.

Unlike the previously proposed scenario for SMS formation, which postulates extremely strong ultraviolet radiation to quench H_2 cooling, our scenario here naturally explains SMBH seed formation in the assembly process of the first galaxies, even without such strong radiation.

8.2 Collapse phase of the supermassive cloud

In chapter 5, we investigated the collapse phase of a supermassive cloud. Most previous studies simply have supposed that a massive primordial cloud without H_2 molecules can collapse monolithically avoiding strong fragmentation and form a supermassive star. Moreover, the H_2 cooling, which is the most important process to determine the efficiency of gas fragmentation, has been neglected in the previous hydrodynamical simulations. Then, we have investigated the fate of a supermassive cloud performing the three-dimensional hydrodynamical simulations and considering the all cooling processes which does work on the gas evolutionary track. We have found the following results.

- A supermassive cloud with turbulence can collapse runaway by various radiative cooling processes (Lyα, two-photon, H^- free-bound, free-free emissions) without efficient fragmentation. Though the H_2 fractions are rapidly enhanced by the three-body reaction ($3H \rightarrow H_2 + H$), the H_2 cooling (both of line and continuum emission) never play a significant role for the thermal evolution at the central region. Finally, single protostar is formed when the central region becomes optically thick.

- The H_2 cooling does work at somewhat low temperature region due to the turbulent motions (i.e., adiabatic cooling) because the H_2 dissociation rate rapidly decreases at such region. Then, many cold clumps are formed in the low-density envelope by the thermal instability due to the H_2 cooling.

- The formed protostar grows via rapid accretion fed the dense filamentary flows. The accretion rate is so high ($\dot{M}_{\rm acc} \sim 3\ M_\odot\ {\rm yr}^{-1}$) that the protostar is expected to evolve up to a supermassive star ($\gtrsim 10^5\ M_\odot$) within its lifetime.

- At the end our simulation, the protostar rapidly grows to $\sim 3\ M_\odot$, whose radius is as large as ~ 2 AU. The properties of the central protostar are consistent with the result of the stellar-structure evolution by Hosokawa et al. (2012), who assumes the spherical accretion.

8.3 Evolution of the protostar up to a SMS

In chapter 6, we have investigated the stability against the stellar pulsations of an protostar which rapidly grows to a SMS via gas accretion at the rate of $\gtrsim 0.01\ M_\odot\ {\rm yr}^{-1}$. Like massive stars as well as giant stars, both of which are known to be pulsationally unstable, rapidly accreting protostars may also be unstable to launch strong pulsation-driven outflows. If this is the case, the stellar growth via accretion will be hindered by the mass-loss. We have applied the linear stability analysis to the proto-stellar structures at the early stage ($M_* \lesssim 10^3\ M_\odot$) and found the followings.

- Massive protostars with $M_* \gtrsim 600\ M_\odot$ and very high accretion rate $\dot{M}_{\rm acc} \gtrsim 1.0\ M_\odot\ {\rm yr}^{-1}$ are unstable due to the κ mechanism. The pulsation is excited in the He^+ ionization layer in the envelope.

- Even under a conservative assumption that all the pulsation energy is converted into the kinetic energy of the outflows, the mass-loss rate is $10^{-3}\ M_\odot\ {\rm yr}^{-1}$, which is lower than the accretion rate by more than two orders of magnitude.

From these results, we concluded that rapidly accreting protostars should grow stably at least in the mass range we studied. As long as the rapid accretion is maintained in the later stage, protostars will become SMSs, which eventually produce seeds for the high-z SMBHs.

In chapter 7, we have solved the structures of the protostars growing via rapid gas accretion for $M_* \gtrsim 10^5\ M_\odot$. We also investigated the pulsational stability of the SMSs for higher mass range than that discussed in chapter 6, and found the followings.

- Under rapid accretion, the stellar radius continues to increases monolithically with the stellar mass following $R_* \propto M_*^{1/2}$. The stellar interior inhomogeneously contracts by losing the thermal energy. The expansion phase ends and begins to contract when the mass exceeds $10^4\ M_\odot$. The maximum of the stellar radius is $R_* \simeq 4 \times 10^4\ R_\odot \sim 10^2$ AU for $M_* \sim 10^4\ M_\odot$.
- Accreting SMSs become pulsation unstable due to the κ-mechanism as in seen chapter6, but the resulting mass-loss rates are still much lower than the accretion rates for $M_* > 10^3\ M_\odot$.
- With this very large radius, the stellar effective temperature is less than 10^4 K even after the protostar becomes supermassive. Stellar UV radiation is much weaker than for non-accreting ZAMS stars. Strong UV feedback, which could limit the mass accretion onto the star, is thus unlikely to operate in this case.

Therefore, we have concluded that the SMSs formed via very rapid mass accretion are not significantly affected by stellar UV feedback or pulsational mass loss.

Acknowledgements

I would like to express my deepest respect and most sincere gratitude to my supervisor, Kazuyuki Omukai for his continuous supports and encouragements during my graduate year. He provided me opportunities to start researches of start formation in the early universe. I also learned from him what a researcher should acquire. I extend sincere thank to Takashi Hosokawa and Kei Tanaka. Fruitful discussions with them help me to generate studies with basic and new concepts of star formation. I am also grateful to Shu-ichiro Inutsuka. He advised and recommended me to study astrophysics when I was an undergraduate student.

I would like to thank the current and former members of the TAP, theoretical astrophysical group and YITP, Yukawa institute for theoretical physics at Kyoto University, Takashi Nakamura, Tetsuya Shiromizu, Naoki Seto, Yoshiyuki Yamada, Jiro Soda, Masaki Ando, Tsutomu Kobayashi, Misao Sasaki, Masaru Shibata, Takahiro Tanaka, Atsushi Taruya, and Shigehiro Nagataki. I am also thankful to my colleagues, Kenta Hotokezaka, Kazuyuki Sugimura, Soichiro Isoyama, Yusuke Korai, and Jonathan White for giving me their friendships and encouragements. I enjoyed discussing many interesting subjects with Daisuke Nakauchi, Sanemichi Takahashi, Tomoya Kinugawa, Sho Fujibayashi, Taku Watanabe, Yudai Suwa, Yuichiro Sekiguchi, Kenta Kiuchi, Hiroki Nagakura, Takashi Yoshida, Atsushi Nishizawa, and Ryo Saito. I thank the members of the UTAP, university of Tokyo theoretical astrophysics, Naoki Yoshida, Shingo Hirano, and Gen Chiaki for precious comments and discussions. I am also grateful to Kiyoe Yokota and Tomoko Ozaki for their supports on my paperworks. I greatly thanks my parents, my sister, and my grandparents for their supports. Finally, I thank all my friends for my pleasant life in Kyoto.

Appendix A

Linear stability analysis against stellar pulsations

In this appendix, we describe our method of the linear perturbation analysis of the stellar pulsation stability (e.g., Cox 1980; Unno et al. 1989). The basic equations governing the stellar structure are

$$\frac{\partial\rho}{\partial t} + \nabla\cdot(\rho\mathbf{v}) = 0, \tag{A.1}$$

$$\frac{\partial\mathbf{v}}{\partial t} + (\mathbf{v}\cdot\nabla)\mathbf{v} = -\frac{1}{\rho}\nabla p - \nabla\Phi, \tag{A.2}$$

$$\nabla^2\Phi = 4\pi G\rho, \tag{A.3}$$

$$T\left[\frac{\partial S}{\partial t} + (\mathbf{v}\cdot\nabla)S\right] = \epsilon - \frac{1}{\rho}\nabla\cdot\mathbf{F}, \tag{A.4}$$

$$\mathbf{F}_{\rm rad} = -\frac{4ac}{3\kappa\rho}T^3\nabla T, \tag{A.5}$$

where ρ is the density, $\mathbf{v}$ the velocity, p the pressure, Φ the gravitational potential, T the temperature, S the specific entropy, ϵ the nuclear-energy generation rate per unit mass, κ the opacity, $\mathbf{F}$ the total energy flux, which is the sum of the radiative flux $\mathbf{F}_{\rm rad}$ and convective flux $\mathbf{F}_{\rm conv}$, G the gravitational constant, c the speed of light, and a the radiation constant. The radial mode, i.e., perturbations which radially oscillate with an eigen frequency σ, is studied.

We consider the radial displacement of fluid elements from the equilibrium positions in the form $\xi_r(r,t) \equiv \xi_r(r)e^{i\sigma t}$. We define the resulting Euler perturbation of a physical quantity Q as $Q' \equiv Q(r,t) - Q_0(r,t)$, where Q_0 is the value in the unperturbed state. We also use the Lagrange perturbation $\delta Q \equiv Q(r+\xi_r,t) - Q_0(r,t)$ for some physical quantities. The linearized equations (A.1)-(A.5) with the perturbations $Q'(r,t) = Q'(r)e^{i\sigma t}$ and $\delta Q(r,t) = \delta Q(r)e^{i\sigma t}$ are written as

$$\frac{1}{r^2}\frac{d}{dr}(r^2\xi_r) - \frac{g}{c_{\rm s}^2}\xi_r + \frac{p'}{\rho c_{\rm s}^2} = \upsilon_{\rm T}\frac{\delta S}{c_{\rm P}}, \tag{A.6}$$

$$\frac{1}{\rho}\frac{dp'}{dr} + \frac{g}{\rho c_{\mathrm{s}}^2}p' + (N^2 - \sigma^2)\xi_r + \frac{d\Phi'}{dr} = g\upsilon_{\mathrm{T}}\frac{\delta S}{c_{\mathrm{P}}}, \tag{A.7}$$

$$\frac{1}{r^2}\frac{d}{dr}\left(r^2\frac{d\Phi'}{dr}\right) - 4\pi G\rho\left(\frac{p'}{\rho c_{\mathrm{s}}^2} + \frac{N^2}{g}\xi_r\right) = -4\pi G\rho\upsilon_{\mathrm{T}}\frac{\delta S}{c_{\mathrm{P}}}, \tag{A.8}$$

$$i\sigma T\delta S = \delta\epsilon - \frac{d\delta L_{\mathrm{rad}}}{dM_r}, \tag{A.9}$$

$$\frac{\delta L_{\mathrm{rad}}}{L_{\mathrm{rad}}} = -\frac{\delta\kappa}{\kappa} + 4\frac{\delta T}{T} + 4\frac{\xi_r}{r} + \frac{d(\frac{\delta T}{T})/d\ln r}{d\ln T/d\ln r}, \tag{A.10}$$

where c_{s} ($= \sqrt{\Gamma_1 p/\rho}$) is the sound velocity, $\Gamma_1 = (\partial\ln p/\partial\ln\rho)_S$ the adiabatic exponent, r the radius, g the gravitational acceleration, L_{rad} the radiative luminosity, M_r the enclosed mass, $c_{\mathrm{P}} = T(\partial S/\partial T)_p$ the isobaric specific heat, $\upsilon_{\mathrm{T}} \equiv -(\partial\ln\rho/\partial\ln T)_p$, and $N^2 \equiv -g(d\ln\rho/dr + g/c_{\mathrm{s}}^2)$ the Brunt-Väisärä frequency. In the above equations, for simplicity, a physical quantity "Q" indicates its value in the unperturbed state instead of Q_0.

Note that, in equations (A.9) and (A.10), we ignore the perturbation of the convective energy flux, i.e., $\delta\mathbf{F}_{\mathrm{conv}} = 0$. This so-called "frozen-in" approximation has been widely used in analyzing the pulsational stability of stars (Baraffe et al. 2001 and Sonoi & Umeda 2012). To facilitate the comparison between their results, we also adopt this assumption here (see Section 6.3 for more discussions).

From equations (A.6) and (A.8) and the regularity of Φ' at the center,

$$\frac{d\Phi'}{dr} + 4\pi G\rho\xi_r = 0. \tag{A.11}$$

Eliminating the term $d\Phi'/dr$ in equations (A.7)-(A.10) with this relation, we obtain four linear ordinary first-order differential equations for four variables ξ_r, p', δS, and δL_{rad}. Here, we impose the following boundary conditions:

$$\frac{d}{dr}\left(\frac{\xi_r}{r}\right) = 0, \quad \frac{d}{dr}\left(\frac{\delta L_{\mathrm{rad}}}{L_{\mathrm{rad}}}\right) = 0 \qquad (r = 0), \tag{A.12}$$

$$\frac{d}{dr}\left(\frac{\delta p}{p}\right) = 0 \qquad (r = R_*), \tag{A.13}$$

from the regularity of the perturbations at the center and surface, and

$$\frac{\delta F_{\mathrm{rad},r}}{F_{\mathrm{rad},r}} = 4\frac{\delta T}{T} \qquad (r = R_*), \tag{A.14}$$

which guarantees outward propagation of the energy flux at the surface (e.g., Cox 1980; Saio, Winget & Robinson 1983). In this system of the differential equations and boundary conditions, the normalization of the variables ξ_r, p', δS, δL_{rad} still remains as a degree of freedom. We solve the system as an eigenvalue problem by formally introducing a differential equation for the eigenvalue σ,

$$\frac{d\sigma}{dr} = 0. \tag{A.15}$$

The whole system here is the five first-order differential equations for ξ_r, p', δS, $\delta L_{\rm rad}$, and σ with the four boundary conditions and one normalization condition. We set the arbitrary normalization condition at the surface, $\xi_r(r = R_*) = R_*$. We obtain numerical solutions of the eigen functions and eigenvalue using the relaxation method (e.g., Unno et al. 1989).

Bibliography

T. Abel, P. Anninos, Y. Zhang, and M. L. Norman. Modeling primordial gas in numerical cosmology. New A, 2:181–207, August 1997. doi: 10.1016/S1384-1076(97)00010-9.

M. A. Abramowicz, B. Czerny, J. P. Lasota, and E. Szuszkiewicz. Slim accretion disks. ApJ, 332:646–658, September 1988. doi: 10.1086/166683.

B. Agarwal, S. Khochfar, J. L. Johnson, E. Neistein, C. Dalla Vecchia, and M. Livio. Ubiquitous seeding of supermassive black holes by direct collapse. MNRAS, 425: 2854–2871, October 2012. doi: 10.1111/j.1365-2966.2012.21651.x.

M. A. Alvarez, J. H. Wise, and T. Abel. Accretion onto the First Stellar-Mass Black Holes. ApJ, 701:L133–L137, August 2009. doi: 10.1088/0004-637X/701/2/L133.

I. Appenzeller. The evolution of a vibrationally unstable main-sequence star of 130 M sun. A&A, 5:355–371, May 1970a.

I. Appenzeller. Mass Loss Rates for Vibrationally Unstable Very Massive Main-sequence Stars. A&A, 9:216, December 1970b.

P. J. Armitage and P. Natarajan. Accretion during the Merger of Supermassive Black Holes. ApJ, 567:L9–L12, March 2002. doi: 10.1086/339770.

I. Baraffe, A. Heger, and S. E. Woosley. On the Stability of Very Massive Primordial Stars. ApJ, 550:890–896, April 2001. doi: 10.1086/319808.

M. C. Begelman. Black holes in radiation-dominated gas - an analogue of the Bondi accretion problem. MNRAS, 184:53–67, July 1978.

M. C. Begelman and I. Shlosman. Angular Momentum Transfer and Lack of Fragmentation in Self-Gravitating Accretion Flows. ApJ, 702:L5–L8, September 2009. doi: 10.1088/0004-637X/702/1/L5.

M. C. Begelman, R. D. Blandford, and M. J. Rees. Massive black hole binaries in active galactic nuclei. Nature, 287:307–309, September 1980. doi: 10.1038/287307a0.

M. C. Begelman, M. Volonteri, and M. J. Rees. Formation of supermassive black holes by direct collapse in pre-galactic haloes. MNRAS, 370:289–298, July 2006. doi: 10.1111/j.1365-2966.2006.10467.x.

A. R. Bell. The acceleration of cosmic rays in shock fronts. I. MNRAS, 182:147–156, January 1978.

M. C. Bentz, B. M. Peterson, H. Netzer, R. W. Pogge, and M. Vestergaard. The Radius-Luminosity Relationship for Active Galactic Nuclei: The Effect of Host-Galaxy Starlight on Luminosity Measurements. II. The Full Sample of Reverberation-Mapped AGNs. ApJ, 697:160–181, May 2009. doi: 10.1088/0004-637X/697/1/160.

S. Bianchi and R. Schneider. Dust formation and survival in supernova ejecta. MNRAS, 378:973–982, July 2007. doi: 10.1111/j.1365-2966.2007.11829.x.

Y. Birnboim and A. Dekel. Virial shocks in galactic haloes? MNRAS, 345:349–364, October 2003. doi: 10.1046/j.1365-8711.2003.06955.x.

E. Böhm-Vitense. Über die Wasserstoffkonvektionszone in Sternen verschiedener Effektivtemperaturen und Leuchtkräfte. Mit 5 Textabbildungen. ZAp, 46:108, 1958.

V. Bromm and A. Loeb. Formation of the First Supermassive Black Holes. ApJ, 596: 34–46, October 2003. doi: 10.1086/377529.

V. Bromm and N. Yoshida. The First Galaxies. ARA&A, 49:373–407, September 2011. doi: 10.1146/annurev-astro-081710-102608.

V. Bromm, N. Yoshida, and L. Hernquist. The First Supernova Explosions in the Universe. ApJ, 596:L135–L138, October 2003. doi: 10.1086/379359.

G. L. Bryan and M. L. Norman. Statistical Properties of X-Ray Clusters: Analytic and Numerical Comparisons. ApJ, 495:80–99, March 1998. doi: 10.1086/305262.

E. Caffau, P. Bonifacio, P. François, L. Sbordone, L. Monaco, M. Spite, F. Spite, H.-G. Ludwig, R. Cayrel, S. Zaggia, F. Hammer, S. Randich, P. Molaro, and V. Hill. An extremely primitive star in the Galactic halo. Nature, 477:67–69, September 2011. doi: 10.1038/nature10377.

M. Campanelli, C. O. Lousto, Y. Zlochower, and D. Merritt. Maximum Gravitational Recoil. *Physical Review Letters*, 98(23):231102, June 2007. doi: 10.1103/PhysRevLett.98.231102.

S. Chandrasekhar. The Dynamical Instability of Gaseous Masses Approaching the Schwarzschild Limit in General Relativity. ApJ, 140:417, August 1964a. doi: 10.1086/147938.

S. Chandrasekhar. Dynamical Instability of Gaseous Masses Approaching the Schwarzschild Limit in General Relativity. *Physical Review Letters*, 12:114–116, January 1964b. doi: 10.1103/PhysRevLett.12.114.

P. C. Clark, S. C. O. Glover, and R. S. Klessen. The First Stellar Cluster. ApJ, 672: 757–764, January 2008. doi: 10.1086/524187.

J. P. Cox. *Theory of stellar pulsation.* 1980.

J. Cuadra, P. J. Armitage, R. D. Alexander, and M. C. Begelman. Massive black hole binary mergers within subparsec scale gas discs. MNRAS, 393:1423–1432, March 2009. doi: 10.1111/j.1365-2966.2008.14147.x.

A. Dekel and Y. Birnboim. Galaxy bimodality due to cold flows and shock heating. MNRAS, 368:2–20, May 2006. doi: 10.1111/j.1365-2966.2006.10145.x.

A. Dekel, Y. Birnboim, G. Engel, J. Freundlich, T. Goerdt, M. Mumcuoglu, E. Neistein, C. Pichon, R. Teyssier, and E. Zinger. Cold streams in early massive hot haloes as the main mode of galaxy formation. Nature, 457:451–454, January 2009. doi: 10.1038/nature07648.

T. Di Matteo, N. Khandai, C. DeGraf, Y. Feng, R. A. C. Croft, J. Lopez, and V. Springel. Cold Flows and the First Quasars. ApJ, 745:L29, February 2012. doi: 10.1088/2041-8205/745/2/L29.

M. Dijkstra, Z. Haiman, A. Mesinger, and J. S. B. Wyithe. Fluctuations in the high-redshift Lyman-Werner background: close halo pairs as the origin of supermassive black holes. MNRAS, 391:1961–1972, December 2008. doi: 10.1111/j.1365-2966.2008.14031.x.

G. Dopcke, S. C. O. Glover, P. C. Clark, and R. S. Klessen. On the Initial Mass Function of Low-metallicity Stars: The Importance of Dust Cooling. ApJ, 766:103, April 2013. doi: 10.1088/0004-637X/766/2/103.

A. G. Doroshkevich. The space structure of perturbations and the origin of rotation of galaxies in the theory of fluctuation. *Astrofizika*, 6:581–600, 1970.

B. T. Draine and F. Bertoldi. Structure of Stationary Photodissociation Fronts. ApJ, 468:269, September 1996. doi: 10.1086/177689.

M.-A. Dupret, A. Grigahcène, R. Garrido, M. Gabriel, and R. Scuflaire. Convection-pulsation coupling. II. Excitation and stabilization mechanisms in δ Sct and γ Dor stars. A&A, 435:927–939, June 2005. doi: 10.1051/0004-6361:20041817.

G. Efstathiou and B. J. T. Jones. The rotation of galaxies - Numerical investigations of the tidal torque theory. MNRAS, 186:133–144, January 1979.

D. J. Eisenstein and A. Loeb. Origin of quasar progenitors from the collapse of low-spin cosmological perturbations. ApJ, 443:11–17, April 1995. doi: 10.1086/175498.

D. J. Eisenstein, I. Zehavi, D. W. Hogg, R. Scoccimarro, M. R. Blanton, R. C. Nichol, R. Scranton, H.-J. Seo, M. Tegmark, Z. Zheng, S. F. Anderson, J. Annis, N. Bahcall, J. Brinkmann, S. Burles, F. J. Castander, A. Connolly, I. Csabai, M. Doi, M. Fukugita, J. A. Frieman, K. Glazebrook, J. E. Gunn, J. S. Hendry, G. Hennessy, Z. Ivezić, S. Kent, G. R. Knapp, H. Lin, Y.-S. Loh, R. H. Lupton, B. Margon, T. A. McKay, A. Meiksin, J. A. Munn, A. Pope, M. W. Richmond, D. Schlegel, D. P. Schneider, K. Shimasaku, C. Stoughton, M. A. Strauss, M. SubbaRao, A. S. Szalay, I. Szapudi, D. L. Tucker, B. Yanny, and D. G. York. Detection of the Baryon Acoustic Peak in the Large-Scale Correlation Function of SDSS Luminous Red Galaxies. ApJ, 633: 560–574, November 2005. doi: 10.1086/466512.

X. Fan. Evolution of high-redshift quasars. New A Rev., 50:665–671, November 2006. doi: 10.1016/j.newar.2006.06.077.

X. Fan, J. F. Hennawi, G. T. Richards, M. A. Strauss, D. P. Schneider, J. L. Donley, J. E. Young, J. Annis, H. Lin, H. Lampeitl, R. H. Lupton, J. E. Gunn, G. R. Knapp, W. N. Brandt, S. Anderson, N. A. Bahcall, J. Brinkmann, R. J. Brunner, M. Fukugita, A. S. Szalay, G. P. Szokoly, and D. G. York. A Survey of $z > 5.7$ Quasars in the Sloan Digital Sky Survey. III. Discovery of Five Additional Quasars. AJ, 128:515–522, August 2004. doi: 10.1086/422434.

L. Ferrarese and D. Merritt. A Fundamental Relation between Supermassive Black Holes and Their Host Galaxies. ApJ, 539:L9–L12, August 2000. doi: 10.1086/312838.

D. Galli and F. Palla. The chemistry of the early Universe. A&A, 335:403–420, July 1998.

K. Gebhardt, R. Bender, G. Bower, A. Dressler, S. M. Faber, A. V. Filippenko, R. Green, C. Grillmair, L. C. Ho, J. Kormendy, T. R. Lauer, J. Magorrian, J. Pinkney, D. Richstone, and S. Tremaine. A Relationship between Nuclear Black Hole Mass and Galaxy Velocity Dispersion. ApJ, 539:L13–L16, August 2000. doi: 10.1086/312840.

S. C. O. Glover and P. W. J. L. Brand. Radiative feedback from an early X-ray background. MNRAS, 340:210–226, March 2003. doi: 10.1046/j.1365-8711.2003.06311.x.

D. O. Gough. Mixing-length theory for pulsating stars. ApJ, 214:196–213, May 1977. doi: 10.1086/155244.

T. H. Greif and V. Bromm. Two populations of metal-free stars in the early Universe. MNRAS, 373:128–138, November 2006. doi: 10.1111/j.1365-2966.2006.11017.x.

T. H. Greif, J. L. Johnson, V. Bromm, and R. S. Klessen. The First Supernova Explosions: Energetics, Feedback, and Chemical Enrichment. ApJ, 670:1–14, November 2007. doi: 10.1086/522028.

T. H. Greif, J. L. Johnson, R. S. Klessen, and V. Bromm. The first galaxies: assembly, cooling and the onset of turbulence. MNRAS, 387:1021–1036, July 2008. doi: 10.1111/j.1365-2966.2008.13326.x.

T. H. Greif, S. C. O. Glover, V. Bromm, and R. S. Klessen. The First Galaxies: Chemical Enrichment, Mixing, and Star Formation. ApJ, 716:510–520, June 2010. doi: 10.1088/0004-637X/716/1/510.

K. Gültekin, D. O. Richstone, K. Gebhardt, T. R. Lauer, S. Tremaine, M. C. Aller, R. Bender, A. Dressler, S. M. Faber, A. V. Filippenko, R. Green, L. C. Ho, J. Kormendy, J. Magorrian, J. Pinkney, and C. Siopis. The M-σ and M-L Relations in Galactic Bulges, and Determinations of Their Intrinsic Scatter. ApJ, 698:198–221, June 2009. doi: 10.1088/0004-637X/698/1/198.

Z. Haiman and A. Loeb. What Is the Highest Plausible Redshift of Luminous Quasars? ApJ, 552:459–463, May 2001. doi: 10.1086/320586.

Z. Haiman, M. J. Rees, and A. Loeb. H 2 Cooling of Primordial Gas Triggered by UV Irradiation. ApJ, 467:522, August 1996. doi: 10.1086/177628.

Z. Haiman, M. J. Rees, and A. Loeb. Destruction of Molecular Hydrogen during Cosmological Reionization. ApJ, 476:458, February 1997. doi: 10.1086/303647.

Z. Haiman, B. Kocsis, and K. Menou. The Population of Viscosity- and Gravitational Wave-driven Supermassive Black Hole Binaries Among Luminous Active Galactic Nuclei. ApJ, 700:1952–1969, August 2009. doi: 10.1088/0004-637X/700/2/1952.

T. Hanawa and T. Matsumoto. Stability of a Dynamically Collapsing Gas Sphere. PASJ, 52:241, April 2000.

S. Hayakawa, S. Nishimura, and T. Takayanagi. Radiation from the Interstellar Hydrogen Atoms. PASJ, 13:184, 1961.

K. Hayasaki, S. Mineshige, and H. Sudou. Binary Black Hole Accretion Flows in Merged Galactic Nuclei. PASJ, 59:427–441, April 2007.

C. Hayashi. Stellar evolution in early phases of gravitational contraction. PASJ, 13: 450–452, 1961.

A. Heger and S. E. Woosley. The Nucleosynthetic Signature of Population III. ApJ, 567:532–543, March 2002. doi: 10.1086/338487.

A. Heger, L. Jeannin, N. Langer, and I. Baraffe. Pulsations in red supergiants with high L/M ratio. Implications for the stellar and circumstellar structure of supernova progenitors. A&A, 327:224–230, November 1997.

L. G. Henyey, J. E. Forbes, and N. L. Gould. A New Method of Automatic Computation of Stellar Evolution. ApJ, 139:306, January 1964. doi: 10.1086/147754.

F. Herrmann, I. Hinder, D. Shoemaker, P. Laguna, and R. A. Matzner. Gravitational Recoil from Spinning Binary Black Hole Mergers. ApJ, 661:430–436, May 2007. doi: 10.1086/513603.

S. Hirano, T. Hosokawa, N. Yoshida, H. Umeda, K. Omukai, G. Chiaki, and H. W. Yorke. One Hundred First Stars : Protostellar Evolution and the Final Masses. *ArXiv e-prints*, August 2013.

D. Hollenbach and C. F. McKee. Molecule formation and infrared emission in fast interstellar shocks. III - Results for J shocks in molecular clouds. ApJ, 342:306–336, July 1989. doi: 10.1086/167595.

T. Hosokawa, K. Omukai, N. Yoshida, and H. W. Yorke. Protostellar Feedback Halts the Growth of the First Stars in the Universe. *Science*, 334:1250–, December 2011. doi: 10.1126/science.1207433.

T. Hosokawa, K. Omukai, and H. W. Yorke. Rapidly Accreting Supergiant Protostars: Embryos of Supermassive Black Holes? ApJ, 756:93, September 2012a. doi: 10.1088/0004-637X/756/1/93.

T. Hosokawa, N. Yoshida, K. Omukai, and H. W. Yorke. Protostellar Feedback and Final Mass of the Second-generation Primordial Stars. ApJ, 760:L37, December 2012b. doi: 10.1088/2041-8205/760/2/L37.

T. Hosokawa, H. W. Yorke, K. Inayoshi, K. Omukai, and N. Yoshida. Formation of Primordial Supermassive Stars by Rapid Mass Accretion. ApJ, 778:178, December 2013. doi: 10.1088/0004-637X/778/2/178.

K. Inayoshi and K. Omukai. Effect of cosmic ray/X-ray ionization on supermassive black hole formation. MNRAS, 416:2748–2759, October 2011. doi: 10.1111/j.1365-2966.2011.19229.x.

K. Inayoshi and K. Omukai. Supermassive black hole formation by cold accretion shocks in the first galaxies. MNRAS, 422:2539–2546, May 2012. doi: 10.1111/j.1365-2966.2012.20812.x.

K. Inayoshi, T. Hosokawa, and K. Omukai. Pulsational instability of supergiant protostars: do they grow supermassive by accretion? MNRAS, 431:3036–3044, June 2013. doi: 10.1093/mnras/stt362.

N. Indriolo, T. R. Geballe, T. Oka, and B. J. McCall. $H^+{}_3$ in Diffuse Interstellar Clouds: A Tracer for the Cosmic-Ray Ionization Rate. ApJ, 671:1736–1747, December 2007. doi: 10.1086/523036.

T. Inoue and S.-i. Inutsuka. Two-Fluid Magnetohydrodynamic Simulations of Converging H I Flows in the Interstellar Medium. I. Methodology and Basic Results. ApJ, 687:303–310, November 2008. doi: 10.1086/590528.

M. Jeon, A. H. Pawlik, T. H. Greif, S. C. O. Glover, V. Bromm, M. Milosavljević, and R. S. Klessen. The First Galaxies: Assembly with Black Hole Feedback. ApJ, 754:34, July 2012. doi: 10.1088/0004-637X/754/1/34.

L. Jiang, X. Fan, M. Vestergaard, J. D. Kurk, F. Walter, B. C. Kelly, and M. A. Strauss. Gemini Near-Infrared Spectroscopy of Luminous z ˜ 6 Quasars: Chemical Abundances, Black Hole Masses, and Mg II Absorption. AJ, 134:1150, September 2007. doi: 10.1086/520811.

L. Jiang, X. Fan, F. Bian, J. Annis, K. Chiu, S. Jester, H. Lin, R. H. Lupton, G. T. Richards, M. A. Strauss, V. Malanushenko, E. Malanushenko, and D. P. Schneider. A Survey of z ˜ 6 Quasars in the Sloan Digital Sky Survey Deep Stripe. II. Discovery of Six Quasars at z $_{AB}$¿21. AJ, 138:305–311, July 2009. doi: 10.1088/0004-6256/138/1/305.

J. L. Johnson, S. Khochfar, T. H. Greif, and F. Durier. Accretion on to black holes formed by direct collapse. MNRAS, 410:919–933, January 2011. doi: 10.1111/j.1365-2966.2010.17491.x.

J. L. Johnson, V. C. Dalla, and S. Khochfar. The First Billion Years project: the impact of stellar radiation on the co-evolution of Populations II and III. MNRAS, 428:1857–1872, January 2013. doi: 10.1093/mnras/sts011.

H. Kang and P. R. Shapiro. Radiative shocks and hydrogen molecules in pregalactic gas - The effects of postshock radiation. ApJ, 386:432–451, February 1992. doi: 10.1086/171029.

D. Kereš, N. Katz, D. H. Weinberg, and R. Davé. How do galaxies get their gas? MNRAS, 363:2–28, October 2005. doi: 10.1111/j.1365-2966.2005.09451.x.

N. Khandai, Y. Feng, C. DeGraf, T. Di Matteo, and R. A. C. Croft. The formation of galaxies hosting z $\sim$ 6 quasars. MNRAS, 423:2397–2406, July 2012. doi: 10.1111/j.1365-2966.2012.21047.x.

T. Kitayama and N. Yoshida. Supernova Explosions in the Early Universe: Evolution of Radiative Remnants and the Halo Destruction Efficiency. ApJ, 630:675–688, September 2005. doi: 10.1086/432114.

R. A. Knop, G. Aldering, R. Amanullah, P. Astier, G. Blanc, M. S. Burns, A. Conley, S. E. Deustua, M. Doi, R. Ellis, S. Fabbro, G. Folatelli, A. S. Fruchter, G. Garavini, S. Garmond, K. Garton, R. Gibbons, G. Goldhaber, A. Goobar, D. E. Groom,

D. Hardin, I. Hook, D. A. Howell, A. G. Kim, B. C. Lee, C. Lidman, J. Mendez, S. Nobili, P. E. Nugent, R. Pain, N. Panagia, C. R. Pennypacker, S. Perlmutter, R. Quimby, J. Raux, N. Regnault, P. Ruiz-Lapuente, G. Sainton, B. Schaefer, K. Schahmaneche, E. Smith, A. L. Spadafora, V. Stanishev, M. Sullivan, N. A. Walton, L. Wang, W. M. Wood-Vasey, and N. Yasuda. New Constraints on Ω_M, Ω, and w from an Independent Set of 11 High-Redshift Supernovae Observed with the Hubble Space Telescope. ApJ, 598:102–137, November 2003. doi: 10.1086/378560.

E. Komatsu, J. Dunkley, M. R. Nolta, C. L. Bennett, B. Gold, G. Hinshaw, N. Jarosik, D. Larson, M. Limon, L. Page, D. N. Spergel, M. Halpern, R. S. Hill, A. Kogut, S. S. Meyer, G. S. Tucker, J. L. Weiland, E. Wollack, and E. L. Wright. Five-Year Wilkinson Microwave Anisotropy Probe Observations: Cosmological Interpretation. ApJS, 180: 330–376, February 2009. doi: 10.1088/0067-0049/180/2/330.

M. Koppitz, D. Pollney, C. Reisswig, L. Rezzolla, J. Thornburg, P. Diener, and E. Schnetter. Recoil Velocities from Equal-Mass Binary-Black-Hole Mergers. *Physical Review Letters*, 99(4):041102, July 2007. doi: 10.1103/PhysRevLett.99.041102.

M. Kowalski, D. Rubin, G. Aldering, R. J. Agostinho, A. Amadon, R. Amanullah, C. Balland, K. Barbary, G. Blanc, P. J. Challis, A. Conley, N. V. Connolly, R. Covarrubias, K. S. Dawson, S. E. Deustua, R. Ellis, S. Fabbro, V. Fadeyev, X. Fan, B. Farris, G. Folatelli, B. L. Frye, G. Garavini, E. L. Gates, L. Germany, G. Goldhaber, B. Goldman, A. Goobar, D. E. Groom, J. Haissinski, D. Hardin, I. Hook, S. Kent, A. G. Kim, R. A. Knop, C. Lidman, E. V. Linder, J. Mendez, J. Meyers, G. J. Miller, M. Moniez, A. M. Mourão, H. Newberg, S. Nobili, P. E. Nugent, R. Pain, O. Perdereau, S. Perlmutter, M. M. Phillips, V. Prasad, R. Quimby, N. Regnault, J. Rich, E. P. Rubenstein, P. Ruiz-Lapuente, F. D. Santos, B. E. Schaefer, R. A. Schommer, R. C. Smith, A. M. Soderberg, A. L. Spadafora, L.-G. Strolger, M. Strovink, N. B. Suntzeff, N. Suzuki, R. C. Thomas, N. A. Walton, L. Wang, W. M. Wood-Vasey, J. L. Yun, and Supernova Cosmology Project. Improved Cosmological Constraints from New, Old, and Combined Supernova Data Sets. ApJ, 686:749–778, October 2008. doi: 10.1086/589937.

J. H. Krolik. Systematic Errors in the Estimation of Black Hole Masses by Reverberation Mapping. ApJ, 551:72–79, April 2001. doi: 10.1086/320091.

D. Lai. Global Nonradial Instabilities of Dynamically Collapsing Gas Spheres. ApJ, 540:946–961, September 2000. doi: 10.1086/309361.

H. J. G. L. M. Lamers and J. P. Cassinelli. *Introduction to Stellar Winds.* June 1999.

R. B. Larson. Numerical calculations of the dynamics of collapsing proto-star. MNRAS, 145:271, 1969.

R. B. Larson. Turbulence and star formation in molecular clouds. MNRAS, 194: 809–826, March 1981.

R. B. Larson. Cloud fragmentation and stellar masses. MNRAS, 214:379–398, June 1985.

M. A. Latif, D. R. G. Schleicher, W. Schmidt, and J. Niemeyer. Black hole formation in the early Universe. MNRAS, 433:1607–1618, August 2013a. doi: 10.1093/mnras/stt834.

M. A. Latif, D. R. G. Schleicher, W. Schmidt, and J. C. Niemeyer. The characteristic black hole mass resulting from direct collapse in the early Universe. MNRAS, 436: 2989–2996, December 2013b. doi: 10.1093/mnras/stt1786.

A. Lawrence, S. J. Warren, O. Almaini, A. C. Edge, N. C. Hambly, R. F. Jameson, P. Lucas, M. Casali, A. Adamson, S. Dye, J. P. Emerson, S. Foucaud, P. Hewett, P. Hirst, S. T. Hodgkin, M. J. Irwin, N. Lodieu, R. G. McMahon, C. Simpson, I. Smail, D. Mortlock, and M. Folger. The UKIRT Infrared Deep Sky Survey (UKIDSS). MNRAS, 379:1599–1617, August 2007. doi: 10.1111/j.1365-2966.2007.12040.x.

Y. Li and Z. G. Gong. Red supergiant variables in the Large Magellanic Cloud: Their evolution and puslations. A&A, 289:449–457, September 1994.

Y. Li, R. S. Klessen, and M.-M. Mac Low. The Formation of Stellar Clusters in Turbulent Molecular Clouds: Effects of the Equation of State. ApJ, 592:975–985, August 2003. doi: 10.1086/375780.

Y. Li, L. Hernquist, B. Robertson, T. J. Cox, P. F. Hopkins, V. Springel, L. Gao, T. Di Matteo, A. R. Zentner, A. Jenkins, and N. Yoshida. Formation of z˜6 Quasars from Hierarchical Galaxy Mergers. ApJ, 665:187–208, August 2007. doi: 10.1086/519297.

G. Lodato and P. Natarajan. Supermassive black hole formation during the assembly of pre-galactic discs. MNRAS, 371:1813–1823, October 2006. doi: 10.1111/j.1365-2966.2006.10801.x.

A. Loeb. Cosmological formation of quasar black holes. ApJ, 403:542–551, February 1993. doi: 10.1086/172224.

A. Loeb and F. A. Rasio. Collapse of primordial gas clouds and the formation of quasar black holes. ApJ, 432:52–61, September 1994. doi: 10.1086/174548.

M.-M. Mac Low. The Energy Dissipation Rate of Supersonic, Magnetohydrodynamic Turbulence in Molecular Clouds. ApJ, 524:169–178, October 1999. doi: 10.1086/307784.

A. I. MacFadyen and M. Milosavljević. An Eccentric Circumbinary Accretion Disk and the Detection of Binary Massive Black Holes. ApJ, 672:83–93, January 2008. doi: 10.1086/523869.

M. E. Machacek, G. L. Bryan, and T. Abel. Simulations of Pregalactic Structure Formation with Radiative Feedback. ApJ, 548:509–521, February 2001. doi: 10.1086/319014.

J. Magorrian, S. Tremaine, D. Richstone, R. Bender, G. Bower, A. Dressler, S. M. Faber, K. Gebhardt, R. Green, C. Grillmair, J. Kormendy, and T. Lauer. The Demography of Massive Dark Objects in Galaxy Centers. AJ, 115:2285–2305, June 1998. doi: 10.1086/300353.

A. Marconi and L. K. Hunt. The Relation between Black Hole Mass, Bulge Mass, and Near-Infrared Luminosity. ApJ, 589:L21–L24, May 2003. doi: 10.1086/375804.

A. Marconi, G. Risaliti, R. Gilli, L. K. Hunt, R. Maiolino, and M. Salvati. Local supermassive black holes, relics of active galactic nuclei and the X-ray background. MNRAS, 351:169–185, June 2004. doi: 10.1111/j.1365-2966.2004.07765.x.

P. Marigo, L. Girardi, C. Chiosi, and P. R. Wood. Zero-metallicity stars. I. Evolution at constant mass. A&A, 371:152–173, May 2001. doi: 10.1051/0004-6361:20010309.

P. Marigo, C. Chiosi, and R.-P. Kudritzki. Zero-metallicity stars. II. Evolution of very massive objects with mass loss. A&A, 399:617–630, February 2003. doi: 10.1051/0004-6361:20021756.

P. G. Martin, D. H. Schwarz, and M. E. Mandy. Master Equation Studies of the Collisional Excitation and Dissociation of H_2 Molecules by H Atoms. ApJ, 461:265, April 1996. doi: 10.1086/177053.

P. Marziani and J. W. Sulentic. Estimating black hole masses in quasars using broad optical and UV emission lines. New A Rev., 56:49–63, February 2012. doi: 10.1016/j.newar.2011.09.001.

L. Mayer, S. Kazantzidis, A. Escala, and S. Callegari. Direct formation of supermassive black holes via multi-scale gas inflows in galaxy mergers. Nature, 466:1082–1084, August 2010. doi: 10.1038/nature09294.

B. J. McCall, A. J. Huneycutt, R. J. Saykally, T. R. Geballe, N. Djuric, G. H. Dunn, J. Semaniak, O. Novotny, A. Al-Khalili, A. Ehlerding, F. Hellberg, S. Kalhori, A. Neau, R. Thomas, F. Österdahl, and M. Larsson. An enhanced cosmic-ray flux towards ζ Persei inferred from a laboratory study of the $H_3{}^+$-e^- recombination rate. Nature, 422:500–502, April 2003. doi: 10.1038/nature01498.

C. F. McKee and J. C. Tan. The Formation of the First Stars. II. Radiative Feedback Processes and Implications for the Initial Mass Function. ApJ, 681:771–797, July 2008. doi: 10.1086/587434.

D. Merritt and M. Y. Poon. Chaotic Loss Cones and Black Hole Fueling. ApJ, 606: 788–798, May 2004. doi: 10.1086/382497.

M. Milosavljević and E. S. Phinney. The Afterglow of Massive Black Hole Coalescence. ApJ, 622:L93–L96, April 2005. doi: 10.1086/429618.

M. Milosavljević, S. M. Couch, and V. Bromm. Accretion Onto Intermediate-Mass Black Holes in Dense Protogalactic Clouds. ApJ, 696:L146–L149, May 2009. doi: 10.1088/0004-637X/696/2/L146.

M. Mori, A. Ferrara, and P. Madau. Early Metal Enrichment by Pregalactic Outflows. II. Three-dimensional Simulations of Blow-Away. ApJ, 571:40–55, May 2002. doi: 10.1086/339913.

D. J. Mortlock, S. J. Warren, B. P. Venemans, M. Patel, P. C. Hewett, R. G. McMahon, C. Simpson, T. Theuns, E. A. Gonzáles-Solares, A. Adamson, S. Dye, N. C. Hambly, P. Hirst, M. J. Irwin, E. Kuiper, A. Lawrence, and H. J. A. Röttgering. A luminous quasar at a redshift of z = 7.085. Nature, 474:616–619, June 2011. doi: 10.1038/nature10159.

T. Nagakura and K. Omukai. Formation of Population III stars in fossil HII regions: significance of HD. MNRAS, 364:1378–1386, December 2005. doi: 10.1111/j.1365-2966.2005.09685.x.

K. Nomoto, N. Tominaga, H. Umeda, C. Kobayashi, and K. Maeda. Nucleosynthesis yields of core-collapse supernovae and hypernovae, and galactic chemical evolution. *Nuclear Physics A*, 777:424–458, October 2006. doi: 10.1016/j.nuclphysa.2006.05.008.

T. Nozawa, T. Kozasa, and A. Habe. Dust Destruction in the High-Velocity Shocks Driven by Supernovae in the Early Universe. ApJ, 648:435–451, September 2006. doi: 10.1086/505639.

K. Ohsuga, M. Mori, T. Nakamoto, and S. Mineshige. Supercritical Accretion Flows around Black Holes: Two-dimensional, Radiation Pressure-dominated Disks with Photon Trapping. ApJ, 628:368–381, July 2005. doi: 10.1086/430728.

K. Omukai. Protostellar Collapse with Various Metallicities. ApJ, 534:809–824, May 2000. doi: 10.1086/308776.

K. Omukai. Primordial Star Formation under Far-Ultraviolet Radiation. ApJ, 546: 635–651, January 2001. doi: 10.1086/318296.

K. Omukai and R. Nishi. Photodissociative Regulation of Star Formation in Metal-free Pregalactic Clouds. ApJ, 518:64–68, June 1999. doi: 10.1086/307285.

K. Omukai and F. Palla. On the Formation of Massive Primordial Stars. ApJ, 561: L55–L58, November 2001. doi: 10.1086/324410.

K. Omukai and F. Palla. Formation of the First Stars by Accretion. ApJ, 589:677–687, June 2003. doi: 10.1086/374810.

K. Omukai, T. Tsuribe, R. Schneider, and A. Ferrara. Thermal and Fragmentation Properties of Star-forming Clouds in Low-Metallicity Environments. ApJ, 626:627–643, June 2005. doi: 10.1086/429955.

K. Omukai, R. Schneider, and Z. Haiman. Can Supermassive Black Holes Form in Metal-enriched High-Redshift Protogalaxies? ApJ, 686:801–814, October 2008. doi: 10.1086/591636.

K. Omukai, T. Hosokawa, and N. Yoshida. Low-metallicity Star Formation: Prestellar Collapse and Protostellar Accretion in the Spherical Symmetry. ApJ, 722:1793–1815, October 2010. doi: 10.1088/0004-637X/722/2/1793.

B. W. O'Shea and M. L. Norman. Population III Star Formation in a ΛCDM Universe. II. Effects of a Photodissociating Background. ApJ, 673:14–33, January 2008. doi: 10.1086/524006.

F. Palla, E. E. Salpeter, and S. W. Stahler. Primordial star formation - The role of molecular hydrogen. ApJ, 271:632–641, August 1983. doi: 10.1086/161231.

J. C. B. Papaloizou. Non-linear pulsations of upper main sequence stars-I.A perturbation approach. MNRAS, 162:143, 1973a.

J. C. B. Papaloizou. Non-linear pulsations of upper main sequence stars-II.Direct numerical integrations. MNRAS, 162:169, 1973b.

P. J. E. Peebles. Origin of the Angular Momentum of Galaxies. ApJ, 155:393, February 1969. doi: 10.1086/149876.

K. Penev, J. Barranco, and D. Sasselov. Direct Calculation of the Turbulent Dissipation Efficiency in Anelastic Convection. ApJ, 705:285–297, November 2009. doi: 10.1088/0004-637X/705/1/285.

M. V. Penston. Dynamics of self-gravitating gaseous spheres-III. Analytical results in the free-fall of isothermal cases. MNRAS, 144:425, 1969.

S. Perlmutter, G. Aldering, G. Goldhaber, R. A. Knop, P. Nugent, P. G. Castro, S. Deustua, S. Fabbro, A. Goobar, D. E. Groom, I. M. Hook, A. G. Kim, M. Y.

Kim, J. C. Lee, N. J. Nunes, R. Pain, C. R. Pennypacker, R. Quimby, C. Lidman, R. S. Ellis, M. Irwin, R. G. McMahon, P. Ruiz-Lapuente, N. Walton, B. Schaefer, B. J. Boyle, A. V. Filippenko, T. Matheson, A. S. Fruchter, N. Panagia, H. J. M. Newberg, W. J. Couch, and Supernova Cosmology Project. Measurements of Omega and Lambda from 42 High-Redshift Supernovae. ApJ, 517:565–586, June 1999. doi: 10.1086/307221.

B. M. Peterson. Reverberation mapping of active galactic nuclei. PASP, 105:247–268, March 1993. doi: 10.1086/133140.

J. B. Pollack, D. Hollenbach, S. Beckwith, D. P. Simonelli, T. Roush, and W. Fong. Composition and radiative properties of grains in molecular clouds and accretion disks. ApJ, 421:615–639, February 1994. doi: 10.1086/173677.

J. A. Regan and M. G. Haehnelt. The formation of compact massive self-gravitating discs in metal-free haloes with virial temperatures of $\sim$13000 − 30000 K. MNRAS, 393:858–871, March 2009a. doi: 10.1111/j.1365-2966.2008.14088.x.

J. A. Regan and M. G. Haehnelt. Pathways to massive black holes and compact star clusters in pre-galactic dark matter haloes with virial temperatures $\gtrsim$10000 K. MNRAS, 396:343–353, June 2009b. doi: 10.1111/j.1365-2966.2009.14579.x.

A. G. Riess, A. V. Filippenko, P. Challis, A. Clocchiatti, A. Diercks, P. M. Garnavich, R. L. Gilliland, C. J. Hogan, S. Jha, R. P. Kirshner, B. Leibundgut, M. M. Phillips, D. Reiss, B. P. Schmidt, R. A. Schommer, R. C. Smith, J. Spyromilio, C. Stubbs, N. B. Suntzeff, and J. Tonry. Observational Evidence from Supernovae for an Accelerating Universe and a Cosmological Constant. AJ, 116:1009–1038, September 1998. doi: 10.1086/300499.

C. Safranek-Shrader, V. Bromm, and M. Milosavljević. Fragmentation in the First Galaxies. ApJ, 723:1568–1582, November 2010. doi: 10.1088/0004-637X/723/2/1568.

D. Schaerer. On the properties of massive Population III stars and metal-free stellar populations. A&A, 382:28–42, January 2002. doi: 10.1051/0004-6361:20011619.

D. Schaerer. The transition from Population III to normal galaxies: Lyalpha and He II emission and the ionising properties of high redshift starburst galaxies. A&A, 397:527–538, January 2003. doi: 10.1051/0004-6361:20021525.

R. Schlickeiser. *Cosmic Ray Astrophysics*. 2002.

R. Schneider, K. Omukai, A. K. Inoue, and A. Ferrara. Fragmentation of star-forming clouds enriched with the first dust. MNRAS, 369:1437–1444, July 2006a. doi: 10.1111/j.1365-2966.2006.10391.x.

R. Schneider, R. Salvaterra, A. Ferrara, and B. Ciardi. Constraints on the initial mass function of the first stars. MNRAS, 369:825–834, June 2006b. doi: 10.1111/j.1365-2966.2006.10331.x.

S. Sethi, Z. Haiman, and K. Pandey. Supermassive Black Hole Formation at High Redshifts Through a Primordial Magnetic Field. ApJ, 721:615–621, September 2010. doi: 10.1088/0004-637X/721/1/615.

C. Shang, G. L. Bryan, and Z. Haiman. Supermassive black hole formation by direct collapse: keeping protogalactic gas H_2 free in dark matter haloes with virial temperatures $T_{vir} \gtrsim 10^4$ K. MNRAS, 402:1249–1262, February 2010. doi: 10.1111/j.1365-2966.2009.15960.x.

P. R. Shapiro and H. Kang. Hydrogen molecules and the radiative cooling of pregalactic shocks. ApJ, 318:32–65, July 1987. doi: 10.1086/165350.

S. L. Shapiro and S. A. Teukolsky. *Black holes, white dwarfs, and neutron stars: The physics of compact objects*. 1983.

R. K. Sheth and G. Tormen. An excursion set model of hierarchical clustering: ellipsoidal collapse and the moving barrier. MNRAS, 329:61–75, January 2002. doi: 10.1046/j.1365-8711.2002.04950.x.

M. Shibata and S. L. Shapiro. Collapse of a Rotating Supermassive Star to a Supermassive Black Hole: Fully Relativistic Simulations. ApJ, 572:L39–L43, June 2002. doi: 10.1086/341516.

J. H. Shiode, E. Quataert, and P. Arras. The stability of massive main-sequence stars as a function of metallicity. MNRAS, 423:3397–3404, July 2012. doi: 10.1111/j.1365-2966.2012.21130.x.

I. Shlosman, J. Frank, and M. C. Begelman. Bars within bars - A mechanism for fuelling active galactic nuclei. Nature, 338:45–47, March 1989. doi: 10.1038/338045a0.

I. Shlosman, M. C. Begelman, and J. Frank. The fuelling of active galactic nuclei. Nature, 345:679–686, June 1990. doi: 10.1038/345679a0.

F. H. Shu. Self-similar collapse of isothermal spheres and star formation. ApJ, 214: 488–497, June 1977. doi: 10.1086/155274.

J. M. Shull and M. E. van Steenberg. X-ray secondary heating and ionization in quasar emission-line clouds. ApJ, 298:268–274, November 1985. doi: 10.1086/163605.

J. Silk and M. J. Rees. Quasars and galaxy formation. A&A, 331:L1–L4, March 1998.

A. Soltan. Masses of quasars. MNRAS, 200:115–122, July 1982.

T. Sonoi and H. Shibahashi. Vibrational Instability of Population III Low-Mass Stars due to the ϵ-Mechanism. PASJ, 63:95–, February 2011.

T. Sonoi and H. Umeda. Vibrational instability of Population III very massive main-sequence stars due to the ?-mechanism. MNRAS, 421:L34–L38, March 2012. doi: 10.1111/j.1745-3933.2011.01201.x.

D. N. Spergel, L. Verde, H. V. Peiris, E. Komatsu, M. R. Nolta, C. L. Bennett, M. Halpern, G. Hinshaw, N. Jarosik, A. Kogut, M. Limon, S. S. Meyer, L. Page, G. S. Tucker, J. L. Weiland, E. Wollack, and E. L. Wright. First-Year Wilkinson Microwave Anisotropy Probe (WMAP) Observations: Determination of Cosmological Parameters. ApJS, 148:175–194, September 2003. doi: 10.1086/377226.

L. Spitzer, Jr. and E. H. Scott. Heating of H i Regions by Energetic Particles. II. Interaction Between Secondaries and Thermal Electrons. ApJ, 158:161, October 1969. doi: 10.1086/150180.

L. Spitzer, Jr. and M. G. Tomasko. Heating of H i Regions by Energetic Particles. ApJ, 152:971, June 1968. doi: 10.1086/149610.

V. Springel, S. D. M. White, A. Jenkins, C. S. Frenk, N. Yoshida, L. Gao, J. Navarro, R. Thacker, D. Croton, J. Helly, J. A. Peacock, S. Cole, P. Thomas, H. Couchman, A. Evrard, J. Colberg, and F. Pearce. Simulations of the formation, evolution and clustering of galaxies and quasars. Nature, 435:629–636, June 2005. doi: 10.1038/nature03597.

A. Stacy and V. Bromm. Impact of cosmic rays on Population III star formation. MNRAS, 382:229–238, November 2007. doi: 10.1111/j.1365-2966.2007.12247.x.

A. Stacy, T. H. Greif, and V. Bromm. The first stars: mass growth under protostellar feedback. MNRAS, 422:290–309, May 2012. doi: 10.1111/j.1365-2966.2012.20605.x.

S. W. Stahler, F. Palla, and E. E. Salpeter. Primordial stellar evolution - The protostar phase. ApJ, 302:590–605, March 1986. doi: 10.1086/164018.

T. Tanaka and Z. Haiman. The Assembly of Supermassive Black Holes at High Redshifts. ApJ, 696:1798–1822, May 2009. doi: 10.1088/0004-637X/696/2/1798.

The Enzo Collaboration, G. L. Bryan, M. L. Norman, B. W. O'Shea, T. Abel, J. H. Wise, M. J. Turk, D. R. Reynolds, D. C. Collins, P. Wang, S. W. Skillman, B. Smith, R. P. Harkness, J. Bordner, J.-h. Kim, M. Kuhlen, H. Xu, N. Goldbaum, C. Hummels, A. G. Kritsuk, E. Tasker, S. Skory, C. M. Simpson, O. Hahn, J. S. Oishi, G. C So, F. Zhao, R. Cen, and Y. Li. Enzo: An Adaptive Mesh Refinement Code for Astrophysics. *ArXiv e-prints*, July 2013.

L. Tornatore, A. Ferrara, and R. Schneider. Population III stars: hidden or disappeared? MNRAS, 382:945–950, December 2007. doi: 10.1111/j.1365-2966.2007.12215.x.

J. K. Truelove, R. I. Klein, C. F. McKee, J. H. Holliman, II, L. H. Howell, and J. A. Greenough. The Jeans Condition: A New Constraint on Spatial Resolution in Simulations of Isothermal Self-gravitational Hydrodynamics. ApJ, 489:L179, November 1997. doi: 10.1086/310975.

T. Tsuribe and K. Omukai. Dust-cooling-induced Fragmentation of Low-Metallicity Clouds. ApJ, 642:L61–L64, May 2006. doi: 10.1086/504290.

Y. Ueda, M. Akiyama, K. Ohta, and T. Miyaji. Cosmological Evolution of the Hard X-Ray Active Galactic Nucleus Luminosity Function and the Origin of the Hard X-Ray Background. ApJ, 598:886–908, December 2003. doi: 10.1086/378940.

H. Uehara and S.-i. Inutsuka. Does Deuterium Enable the Formation of Primordial Brown Dwarfs? ApJ, 531:L91–L94, March 2000. doi: 10.1086/312529.

M. Umemura, A. Loeb, and E. L. Turner. Early Cosmic Formation of Massive Black Holes. ApJ, 419:459, December 1993. doi: 10.1086/173499.

W. Unno. Stellar Radial Pulsation Coupled with the Convection. PASJ, 19:140, 1967.

W. Unno, Y. Osaki, H. Ando, H. Saio, and H. Shibahashi. *Nonradial oscillations of stars.* 1989.

M. Volonteri, F. Haardt, and P. Madau. The Assembly and Merging History of Supermassive Black Holes in Hierarchical Models of Galaxy Formation. ApJ, 582: 559–573, January 2003. doi: 10.1086/344675.

W. R. Webber. A New Estimate of the Local Interstellar Energy Density and Ionization Rate of Galactic Cosmic Cosmic Rays. ApJ, 506:329–334, October 1998. doi: 10.1086/306222.

D. Whalen, B. van Veelen, B. W. O'Shea, and M. L. Norman. The Destruction of Cosmological Minihalos by Primordial Supernovae. ApJ, 682:49–67, July 2008. doi: 10.1086/589643.

S. D. M. White. Angular momentum growth in protogalaxies. ApJ, 286:38–41, November 1984. doi: 10.1086/162573.

C. J. Willott, P. Delorme, C. Reylé, L. Albert, J. Bergeron, D. Crampton, X. Delfosse, T. Forveille, J. B. Hutchings, R. J. McLure, A. Omont, and D. Schade. The Canada-France High-z Quasar Survey: Nine New Quasars and the Luminosity Function at Redshift 6. AJ, 139:906–918, March 2010. doi: 10.1088/0004-6256/139/3/906.

L. A. Willson. Mass Loss From Cool Stars: Impact on the Evolution of Stars and Stellar Populations. ARA&A, 38:573–611, 2000. doi: 10.1146/annurev.astro.38.1.573.

J. H. Wise and T. Abel. Resolving the Formation of Protogalaxies. I. Virialization. ApJ, 665:899–910, August 2007. doi: 10.1086/520036.

J. H. Wise, M. J. Turk, and T. Abel. Resolving the Formation of Protogalaxies. II. Central Gravitational Collapse. ApJ, 682:745–757, August 2008. doi: 10.1086/588209.

J. H. Wise, M. J. Turk, M. L. Norman, and T. Abel. The Birth of a Galaxy: Primordial Metal Enrichment and Stellar Populations. ApJ, 745:50, January 2012. doi: 10.1088/0004-637X/745/1/50.

J. Wolcott-Green and Z. Haiman. Suppression of HD cooling in protogalactic gas clouds by Lyman-Werner radiation. MNRAS, 412:2603–2616, April 2011. doi: 10.1111/j.1365-2966.2010.18080.x.

J. Wolcott-Green, Z. Haiman, and G. L. Bryan. Photodissociation of H_2 in protogalaxies: modelling self-shielding in three-dimensional simulations. MNRAS, 418:838–852, December 2011. doi: 10.1111/j.1365-2966.2011.19538.x.

M. G. Wolfire, D. Hollenbach, C. F. McKee, A. G. G. M. Tielens, and E. L. O. Bakes. The neutral atomic phases of the interstellar medium. ApJ, 443:152–168, April 1995. doi: 10.1086/175510.

M. Yamada and R. Nishi. Fragmentation of a Shock-Compressed Sheet of Primordial Gas. ApJ, 505:148–158, September 1998. doi: 10.1086/306131.

S.-C. Yoon and M. Cantiello. Evolution of Massive Stars with Pulsation-driven Superwinds During the Red Supergiant Phase. ApJ, 717:L62–L65, July 2010. doi: 10.1088/2041-8205/717/1/L62.

H. W. Yorke and P. Bodenheimer. Theoretical Developments in Understanding Massive Star Formation. In H. Beuther, H. Linz, and T. Henning, editors, *Massive Star Formation: Observations Confront Theory*, volume 387 of *Astronomical Society of the Pacific Conference Series*, page 189, May 2008.

Q. Yu. Evolution of massive binary black holes. MNRAS, 331:935–958, April 2002. doi: 10.1046/j.1365-8711.2002.05242.x.

Q. Yu and S. Tremaine. Observational constraints on growth of massive black holes. MNRAS, 335:965–976, October 2002. doi: 10.1046/j.1365-8711.2002.05532.x.

Y. B. Zeldovich and I. D. Novikov. *Relativistic astrophysics. Vol.1: Stars and relativity.* 1971.